

SVCR GOVERNMENT DEGREE
COLLEGE PALAMANER
NAAC EVIDENCES



3.3.1

UGC CARE LIST
JOURNAL
PUBLICATIONS



Data Article

Excess volume, speed of sound and isentropic compressibility data of ternary mixtures containing N-methylcyclohexylamine, *p*-xylene and (C₃-C₅) 1-alkanols



Ch. Bharath Kumar^a, P. Bhanuprakash^b, C. Narasimha Rao^c, R.L. Gardas^d,
K. Sivakumar^{a,*}

^a Department of Chemistry, S.V. Arts Degree & P.G. College (T.T.D'S), Tirupati-517502, A.P., India

^b Department of Chemistry, S.V.C.R. Govt. Degree College, Palamaner-517408, A.P., India

^c Department of Chemistry, Sri Venkateswara University, Tirupati-517502, A.P., India

^d Department of Chemistry, Indian Institute of Technology Madras, Chennai-600036, T.N., India

ARTICLE INFO

Article history:

Received 22 July 2020

Revised 16 October 2020

Accepted 19 November 2020

Available online 21 November 2020

Keywords:

N-methylcyclohexylamine

p-xylene

1-alkanols

Excess volume

Isentropic compressibility

Ternary mixtures

ABSTRACT

Excess volume (V_{123}^E) and speed of sound (u_{123}) data of three ternary mixtures of N-methylcyclohexylamine (NMC) (1) + *p*-xylene (2) + 1-alkanols (C₃-C₅) were determined as a function of composition at 303.15 K and atmospheric pressure. From the measured data, isentropic compressibility (k_{s123}), deviation in isentropic compressibility ($k_{s'123}$) and the quantity Δk_{s123} , the difference between measured value and that of computed from the constituent binary data were derived. The V_{123}^E data of all the mixtures were analyzed in terms of different theoretical models. The experimental and predicted results indicate that the theoretical expressions give good estimation of the derived functions for the studied ternary systems. The excess and deviation properties were discussed in terms of intermolecular interactions prevailing between component molecules in the liquid mixtures.

© 2020 Elsevier B.V. All rights reserved.

Specifications Table

Subject area	Physical Chemistry, Chemical Engineering, Chemical Thermodynamics
Compounds	N-methylcyclohexylamine, <i>p</i> -xylene and 1-alkanols
Data category	Physicochemical properties, Density, ultrasound velocity
Data acquisition format	Chemical data analysis
Data type	Calculated, analyzed
Procedure	Density measurements are made by using single-stem bicapillary pycnometer of bulb capacity 12 cm ³ , and speeds of sound are estimated with single crystal ultrasonic interferometer (model F-82) from Mittal Enterprises, New Delhi, India
Data accessibility	Data is with this article

1. Rationale

Thermodynamic investigation of liquid mixtures is of great interest because of their extensive utilization in process designing, petrochemical industry, textile industry, pharmaceutical industry and in many other chemical engineering appli-

* Corresponding author.

E-mail address: sivakumarkasi64@gmail.com (K. Sivakumar).

cations. When two or more solvent molecules are associated with one another it results in significant differences in their intermolecular interactions. In recent years, measurement of excess volumes and isentropic compressibilities has been adequately employed in understanding molecular interactions in pure liquids and in liquid mixtures [1–4]. Keeping both the industrial and scientific interest in mind, many studies pertaining to thermophysical properties of binary mixtures have been reported in the literature, whereas the same for the ternary systems in particular are scarce. Hence in the present work, we report here new excess volume and deviation in isentropic compressibility data of ternary mixtures containing NMC and *p*-xylene with 1-alkanols (C₃–C₅) at T = 303.15 K and atmospheric pressure.

NMC has wide application in the production of pharmaceuticals, insecticides and pesticides [5]. Xylenes are used in printing, rubber and leather industries. Alkanols are extensively utilized in the manufacture of fuel, perfumes, cosmetics, paints, varnishes, drugs, explosives, fats, waxes, resins, etc., [6]. Because of their extensive industrial applications, knowledge of their thermophysical properties is of great importance from a practical point of view. Therefore, these systems have been selected in order to study the molecular interactions between NMC, *p*-xylene and 1-alkanols (C₃–C₅). In addition, the ternary V^E_{123} data of all the mixtures were analyzed in terms of predictive expressions [7–9]. The experimental data were discussed in terms of molecular interactions between component molecules.

2. Procedure

2.1. Reagents

All chemicals used were of analytical grade. N-methylcyclohexylamine (NMC) (>99.5% of purity) and 1-propanol (>99.7% of purity) were obtained from Sigma Aldrich. *m*-Xylene (>99.5% of purity), 1-butanol (>99.5% of purity) and 1-pentanol (>99.5% of purity) were purchased from Merck. All the chemicals were purified by the standard methods described in the literature [10–11]. The chemical names, acronyms, CAS numbers, molar mass, supplier, and molecular purities of the liquids used were reported in Table 1. The purities of the samples were checked by comparing the measured densities (ρ) and speed of sound (u) of the components with those reported in the literature [12–14] and these values were presented in Table 2.

2.2. Apparatus and procedures (Measurements)

A single-stem bicapillary pycnometer (made of borosil glass) of bulb capacity 12 cm³ was utilized for density measurements. Excess volume (V^E_{123}) data for the ternary mixtures were measured using dilatometer [15]. The mixing cell contained three bulbs of different capacities that were connected by a W-tube. Mercury was used to separate three component liquids. One of the three bulbs was fitted with a capillary and the other two were fitted with ground-glass stoppers. Each bulb of the dilatometer was filled with a component whose mass was determined directly by weighing. The entire dilatometer was placed in a thermostat that could be maintained to 303.15 ± 0.01 K. All the measurements were made at constant temperature employing a thermostat. The measured ternary excess volume data (V^E_{123}) were accurate to ± 0.003 cm³ mol⁻¹.

The speeds of sound data (u_{123}) were measured [3] by a single crystal ultrasonic interferometer (model F-82) from Mittal Enterprises, New Delhi, India. A thermostatically controlled, well-stirred circulated water bath with a temperature controlled to ±0.01 K was used to maintain temperature stability. The uncertainty in sound speed measurement was is ± 0.3%.

Table 1
Characteristics of liquids used in the present work.

Material	Provenance	Molar mass (g.mol ⁻¹)	CAS number	Mass fraction purity
N-methylcyclohexylamine (NMC)	Sigma-Aldrich, India.	113.2	100-60-7	99.5%
1-propanol	Sigma-Aldrich, India.	60.1	71-23-8	99.7%
1-butanol	Merck, India.	74.1	71-36-3	99.5%
1-pentanol	Merck, India.	88.1	71-41-0	99.5%

Table 2
Density (ρ) and speed of sound (u) of pure components at 303.15 K and atmospheric pressure.

Compound	ρ (g.cm ⁻³)		u (m.s ⁻¹)	
	Experimental	Literature	Experimental	Literature
N-methyl cyclohexylamine	0.84683	0.84686 [12]	1356	1354 [12]
<i>p</i> -xylene	0.85229	0.85230 [13]	1289	1290 [13]
1-propanol	0.79566	0.79602 [14]	1189	1192 [14]
1-butanol	0.80205	0.80203 [14]	1229	1227 [14]
1-pentanol	0.80764	0.80764 [14]	1256	1258 [14]

Table 3

Mole fractions of N-methylcyclohexylamine (x_1), *p*-xylene (x_2), experimental and predicted excess volumes for the ternary mixtures of N-methylcyclohexylamine (NMC) (1) + *p*-xylene (2) + 1-alkanols (3) at 303.15 K and atmospheric pressure.

x_1	x_2	V^E ($\text{cm}^3 \cdot \text{mol}^{-1}$)					$\Delta V^E_{123}^*$
		Experimental	(Redlich-Kister)	Kohler	Tsao-Smith	Hwang	
N-methylcyclohexylamine (NMC) (1) + <i>p</i> -xylene (2) + 1-propanol (3)							
0.1010	0.0741	-0.522	-0.525	-0.507	-0.537	-0.550	0.003
0.1113	0.1021	-0.564	-0.567	-0.546	-0.597	-0.595	0.003
0.2224	0.1341	-0.968	-0.974	-0.962	-1.056	-1.014	0.006
0.2092	0.2847	-0.720	-0.732	-0.739	-0.925	-0.801	0.012
0.1729	0.3429	-0.577	-0.590	-0.598	-0.798	-0.649	0.013
0.0564	0.4634	-0.197	-0.210	-0.201	-0.308	-0.229	0.013
0.1373	0.5423	-0.292	-0.306	-0.322	-0.517	-0.359	0.014
0.1658	0.6216	-0.223	-0.238	-0.248	-0.379	-0.301	0.015
0.1275	0.6712	-0.161	-0.172	-0.182	-0.322	-0.219	0.011
0.1626	0.7631	-0.110	-0.117	-0.100	-0.061	-0.166	0.007
0.1056	0.8323	-0.070	-0.074	-0.068	-0.052	-0.107	0.004
0.0801	0.8616	-0.049	-0.052	-0.049	-0.052	-0.078	0.003
N-methylcyclohexylamine (NMC) (1) + <i>p</i> -xylene (2) + 1-butanol (3)							
0.0800	0.049	-0.330	-0.331	-0.324	-0.332	-0.343	0.001
0.1034	0.1026	-0.407	-0.409	0.397	-0.434	-0.426	0.002
0.1204	0.159	-0.198	-0.202	-0.203	-0.384	-0.468	0.004
0.0807	0.2251	-0.284	-0.293	-0.283	-0.351	-0.310	0.009
0.0937	0.3429	-0.265	-0.277	-0.273	-0.377	-0.297	0.012
0.0992	0.4126	-0.236	-0.249	-0.249	-0.369	-0.271	0.013
0.1115	0.5012	-0.196	-0.211	-0.217	-0.354	-0.239	0.015
0.1124	0.5624	-0.156	-0.170	-0.177	-0.312	-0.198	0.014
0.0918	0.6209	-0.095	-0.106	-0.112	-0.232	-0.130	0.011
0.0823	0.6714	-0.062	-0.069	-0.073	-0.183	-0.090	0.007
0.1108	0.7326	-0.072	-0.077	-0.080	-0.154	-0.104	0.005
0.0878	0.8409	-0.041	-0.044	-0.044	-0.049	-0.067	0.003
N-methylcyclohexylamine (NMC) (1) + <i>p</i> -xylene (2) + 1-pentanol (3)							
0.0510	0.081	-0.265	-0.267	-0.270	-0.293	-0.246	0.002
0.1057	0.1534	-0.455	-0.457	-0.466	-0.539	-0.451	0.002
0.0930	0.201	-0.382	-0.385	-0.398	-0.483	-0.377	0.003
0.0648	0.2709	-0.25	-0.255	-0.269	-0.349	-0.247	0.005
0.0966	0.3392	-0.303	-0.309	-0.330	-0.455	-0.300	0.006
0.1081	0.4298	-0.264	-0.273	-0.296	-0.446	-0.267	0.009
0.0654	0.5436	-0.114	-0.126	-0.143	-0.265	-0.123	0.012
0.1818	0.6121	-0.197	-0.211	-0.223	-0.310	-0.228	0.014
0.0678	0.6762	-0.068	-0.079	-0.093	-0.214	-0.081	0.011
0.0992	0.7126	-0.094	-0.104	-0.117	-0.222	-0.112	0.010
0.0477	0.7562	-0.024	-0.032	-0.040	-0.137	-0.035	0.008
0.0676	0.8532	-0.044	-0.049	-0.053	-0.087	-0.062	0.005

$$\Delta V^E_{123} = V^E_{123}(\text{Exp}) - V^E_{123}(\text{bc})$$

Where $V^E_{123}(\text{bc})$ is computed from constituent binary data using Redlich-Kister equation.

3. Data, value and validation

3.1. Excess volume

The measured excess volume data (V^E_{123}) of three ternary liquid mixtures containing NMC and *p*-xylene with 1-propanol, 1-butanol and 1-pentanol at 303.15 K and atmospheric pressure were reported in Table 3 along with those values calculated from predictive expressions namely Redlich-Kister, Kohler, Tsao-Smith and Hwang et al. equations. These data were also graphically depicted in Figs. 1–3.

Redlich-Kister equation [7,8] can be expressed as:

$$V^E_{123} = \sum_{i < j} V^E_{ij}(x_i, x_j) \quad (1)$$

where $V^E_{ij} = x_i x_j \sum_{s=0}^n (A_s)_{ij} (x_i - x_j)^s$ and x_i, x_j are the mole fractions of the components in a ternary mixture.

Kohler Expression [7]:

$$V^E_{123} = (x_1 + x_2)^2 V^E_{12} + (x_1 + x_3)^2 V^E_{13} + (x_2 + x_3)^2 V^E_{23} \quad (2)$$

where $V^E_{ij} = x'_i x'_j \sum_{s=0}^n (A_s)_{ij} (x'_i - x'_j)^s$ at composition (x'_i, x'_j) , such that $x'_i = 1 - x'_j = \frac{x_i}{x_i + x_j}$ where x_i and x_j are the ternary mole fractions.

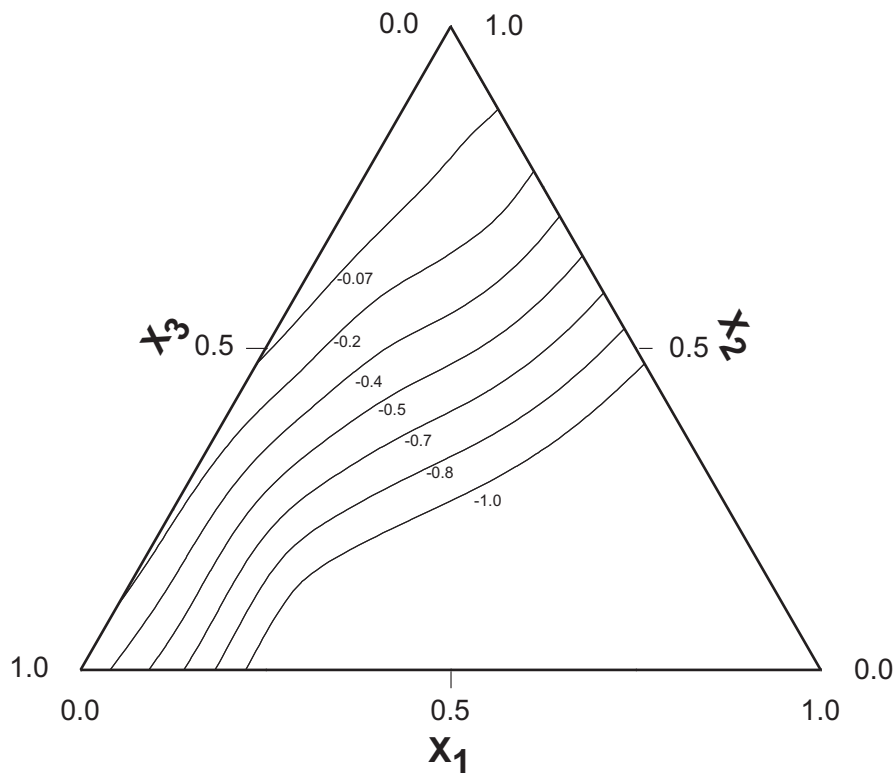


Fig. 1. Excess volumes (V^E_{123}) data for N-methylcyclohexylamine (NMC) (1) + *p*-xylene (2) + 1-propanol (3) at 303.15 K.

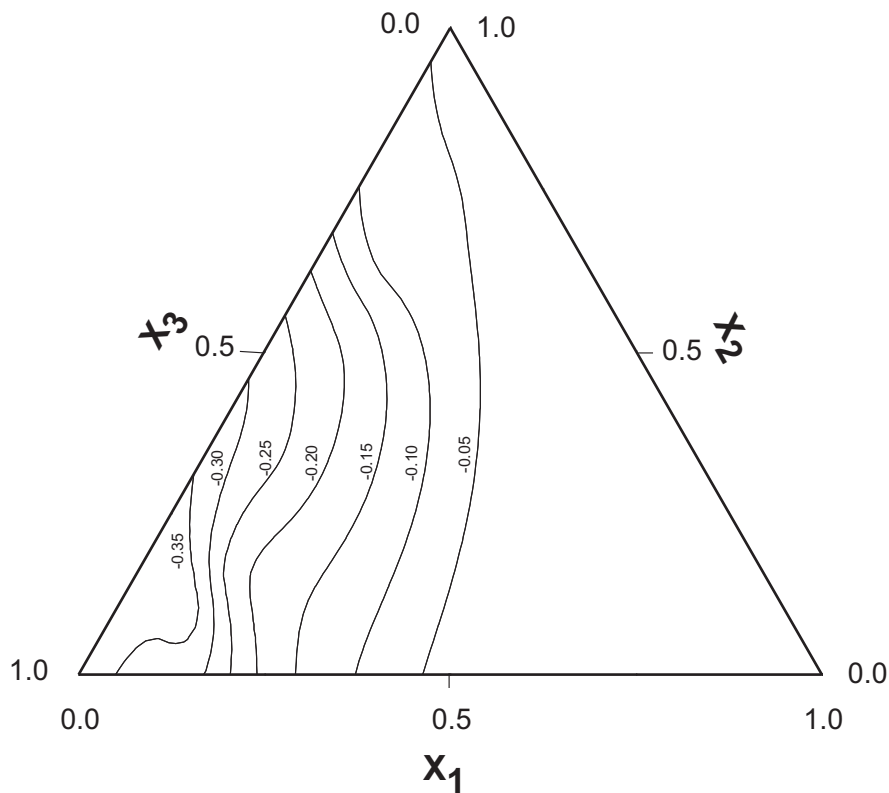


Fig. 2. Excess volumes (V^E_{123}) data for N-methylcyclohexylamine (NMC) (1) + *p*-xylene (2) + 1-butanol (3) at 303.15 K.

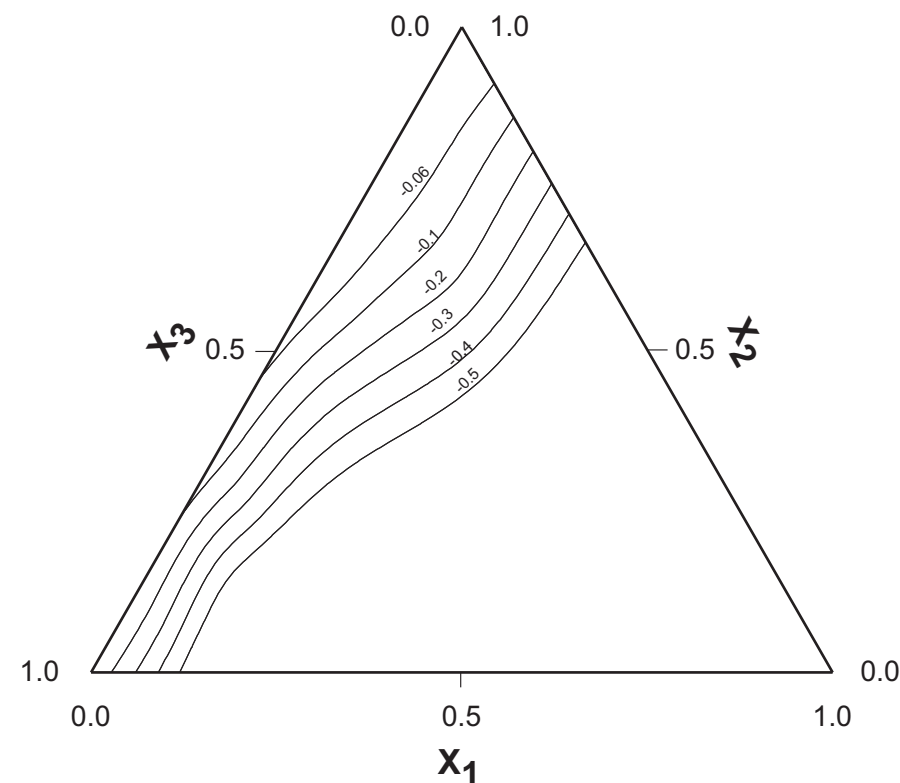


Fig. 3. Excess volumes (V_{123}^E) data for N-methylcyclohexylamine (NMC) (1) + *p*-xylene (2) + 1-pentanol (3) at 303.15 K.

Table 4

The standard deviation values (Redlich-Kister and Hwang eqns) of binary systems of $\sigma(V^E)$ at 303.15 K.

System	Redlich-Kister			$\sigma(V^E)$	Hwang			$\sigma(V^E)$
	a_0 $\text{cm}^3\text{mol}^{-1}$	a_1	a_2		b_0	b_1	b_2	
N-methyl cyclohexylamine (1)+ <i>p</i> -xylene (2)	-0.122	1.220	0.009	0.002	-0.125	1.464	-1.440	0.008
<i>p</i> -xylene (2)+ 1-propanol (3)	-0.076	0.560	0.463	0.000	-0.230	1.285	-0.050	0.006
<i>p</i> -xylene (2) + 1-butanol (3)	0.125	0.576	0.359	0.000	0.005	1.164	-0.207	0.000
<i>p</i> -xylene (2) + 1-pentanol (3)	0.090	0.371	0.027	0.002	0.081	0.477	-0.406	0.007
N-methyl cyclohexylamine (1) +1-propanol (3)	-6.237	2.703	3.925	0.002	-7.545	8.449	2.015	0.002
N-methyl cyclohexylamine (1) +1-butanol (3)	-5.219	0.847	1.908	0.001	-5.852	3.461	1.531	0.002
N-methyl cyclohexylamine (1) +1-pentanol (3)	-5.243	0.955	0.417	0.002	-5.382	1.695	-0.580	0.003

Tsao–Smith expression [7] is of the form:

$$V_{123}^E = x_2(1 + x_1)^{-1}V_{12}^E + x_3(1 - x_1)^{-1}V_{13}^E + (1 - x_1)V_{23}^E \quad (3)$$

where V_{12}^E , V_{13}^E and V_{23}^E are the binary excess volumes at composition (x'_i, x'_j), such that $x'_i = x_1$ for 1,2 and 1,3 binary systems and $x'_2 = \frac{x_2}{x_2+x_3}$ for 2,3 binary system.

Hwang et al. equation [9]:

$$V^{E(123)}/\text{cm}^3\text{mol}^{-1} = x_1x_2(b_0^{(12)} + b_1^{(12)}x_1^3 + b_2^{(12)}x_2^3) + x_1x_3(b_0^{(13)} + b_1^{(13)}x_1^3 + b_3^{(13)}x_3^3) + x_2x_3(b_0^{(23)} + b_2^{(23)}x_2^3 + b_3^{(23)}x_3^3) \quad (4)$$

The quantity ΔV_{123}^E , difference between measured ternary data and computed from the constituent binary data through the Redlich-Kister relation were given in last column of Table 3. The binary data which was used to compute ternary excess volume data for the mixtures NMC+*m*-xylene [12], NMC+1-alkanols [16] and *p*-xylene +1-alkanols [17] were collected from the literature and these data were included in Table 4 along with standard deviation values $\sigma(V^E)$.

The sign and magnitude of V_{123}^E data depends upon the resultant of the following factors [18]:

i dissociation of associated alkanols in solution systems

- ii donor-acceptor interaction between π -electrons of the aromatic ring and the alkanols
- iii a possible inclusion of *p*-xylene into the structural network of alkanols.

The first factor contributes to expansion in volume and the second and third factors lead to contraction in volume. The experimental V^E_{123} data in Table 2 suggest that the combined effects for volume contraction i.e., donor-acceptor interactions and inclusion of *p*-xylene into the structural network of alkanols exceed the factors responsible for volume expansion.

The molecular interaction between NMC and 1-alkanols in the studied ternary mixtures can be explained as follows [19]. Negative contributions in the mixtures containing NMC and 1-alkanol arise from two factors: a) changes in free volumes in the real mixtures and b) the presence of electron donor-acceptor interactions between NMC and 1-alkanol. The negative V^E_{123} values in the present ternary system emphasize that the breaking of the three-dimensional associated network of the alkanol is incomplete and that the aromatic hydrocarbon molecules are more or less fitted into the alkanol networks.

In addition, specific interactions due to the formation of N–H $\cdots\pi$ type hydrogen bond between NMC and electrons in aromatic ring of *p*-xylene also contribute significantly to negative V^E_{123} data of the studied ternary mixtures [12].

A perusal of Table 3 clearly indicates that V^E_{123} data is more negative for the ternary mixtures containing 1-propanol and the negative value decreases with increase in chain length from 1-propanol to 1-pentanol. The effect of increasing chain length of 1-alkanol on the V^E_{123} data can be considered using the effective dipole moment. The negative V^E_{123} values decrease with decreasing effective dipole moment of 1-alkanol in the systems of cyclic amine with alcohols [6] which can be explained as follows. The dipole moment of 1-alkanols decreases with increase in chain length. Polarity of hydroxyl group also decreases with increase in chain length of 1-alkanol. These two factors result in the rupture of alkanol-alkanol hydrogen bonds. Moreover, in higher alkanols, hydroxyl group proton will be shielded by the adjacent methyl groups, thus availability of such protons will be diminished for the formation heteroassociates which ultimately results in decrease in negative V^E_{123} data in higher 1-alkanols [4] in the following order: 1-propanol > 1-butanol > 1-pentanol.

An examination of ternary data in Table 3 reveal that the predictive expressions proposed by Redlich-Kister, Kohler, Tsao-Smith and Hwang et al. gives satisfactory estimation in terms of ternary excess volumes in all the mixtures.

3.2. Isentropic compressibility

The isentropic compressibility of ternary mixtures (κ_{s123}) was calculated from the expression

$$\kappa_{s123} = u^{-2}_{123} \rho^{-1}_{mix123} \quad (5)$$

where u_{123} and ρ_{mix123} indicate speed of sound and density of ternary mixtures respectively.

The density of a ternary liquid mixture (ρ_{mix123}) was computed using the expression

$$\rho_{mix123} = x_1 M_1 + x_2 M_2 + x_3 M_3 / V + V^E_{123} \quad (6)$$

where x_1 , x_2 and x_3 represent mole fractions and M_1 , M_2 and M_3 are the molecular weights of NMC, *p*-xylene and 1-alkanols respectively; V is the molar volume of the mixture and V^E_{123} is ternary excess volume.

The deviation in isentropic compressibility (κ'_{s123}) was estimated using the relation

$$\kappa'_{s123} = \kappa_{s123} - \theta_1 \kappa_{s1} - \theta_2 \kappa_{s2} - \theta_3 \kappa_{s3} \quad (7)$$

where θ_1 , θ_2 , θ_3 , κ_{s1} , κ_{s2} and κ_{s3} are the volume fractions and isentropic compressibilities of the pure components 1, 2 and 3 respectively. The quantity $\Delta\kappa_{s123}$, the difference between measured value of κ_{s123} and that of computed from binary data $\kappa'_{s123(b)}$ has been calculated using the relation

$$\Delta\kappa_{s123} = \kappa'_{s123} - \kappa'_{s123(b)} \quad (8)$$

The latter quantity, $\kappa'_{s123(b)}$ was computed using Redlich-Kister relation [8]

$$\kappa'_{s123(b)} = \kappa_{s12} + \kappa_{s13} + \kappa_{s23} \quad (9)$$

where κ_{s12} , κ_{s13} and κ_{s23} denote the deviation in isentropic compressibilities for the three binary mixtures and these are estimated using the smoothing equation

$$\kappa_{sij} = \theta_1 \theta_2 [a_0 + a_1 (\theta_1 - \theta_2) + a_2 (\theta_1 - \theta_2)^2] \quad (10)$$

where a_0 , a_1 and a_2 are the constants obtained by the method of least squares. Further, the binary parameters that were required to compute $\kappa'_{s123(b)}$ for the mixtures of NMC with *p*-xylene [20], NMC with 1-alkanols [21] and *p*-xylene with 1-alkanols [17] were collected from the literature and these were given in Table 5 along with standard deviation $\sigma(\Delta\kappa_s)$.

The speed of sound (u), density of the mixture (ρ_{mix123}), isentropic compressibility (κ_{s123}), deviation in isentropic compressibility (κ'_{s123}) and the quantity $\Delta\kappa_{s123}$, the difference between measured data of κ_{s123} and that of computed from the constituent binary data $\kappa'_{s123(b)}$ were presented in Table 6. Moreover, the deviation in isentropic compressibility ($\Delta\kappa_{s123}$) for the three ternary mixtures was also graphically represented in Figs. 4–6.

An examination of $\Delta\kappa_{s123}$ values in Table 6 suggest that the values were positive over the entire composition range in all the binary mixtures of NMC and *p*-xylene with 1-alkanols and these were 3 to 4 times to the experimental error.

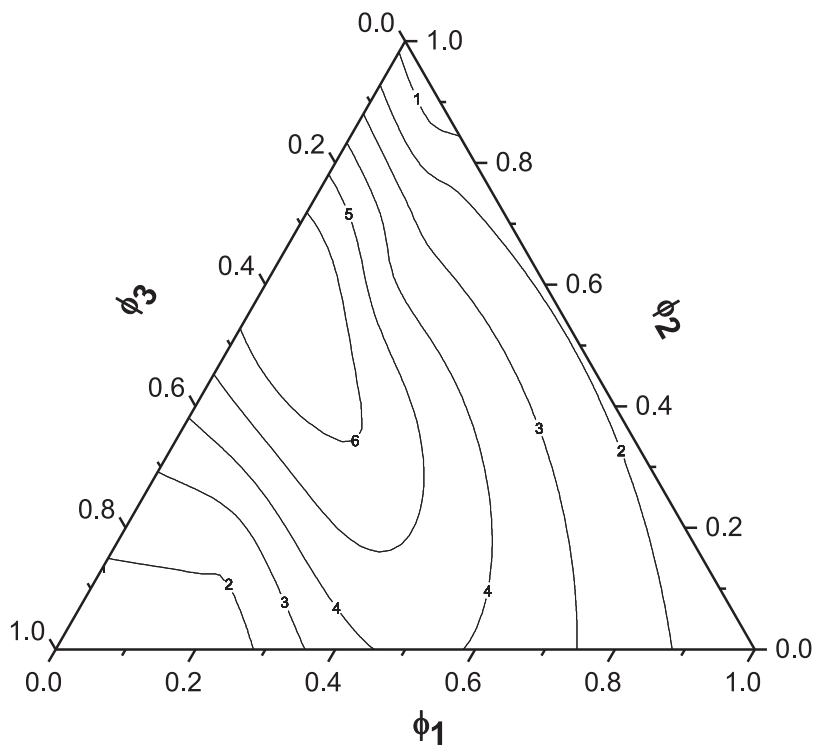


Fig. 4. Deviation in isentropic compressibility ($\Delta\kappa_{s123}$) data for N-methylcyclohexylamine (NMC) (1) + *p*-xylene (2) + 1-propanol (3) at 303.15 K.

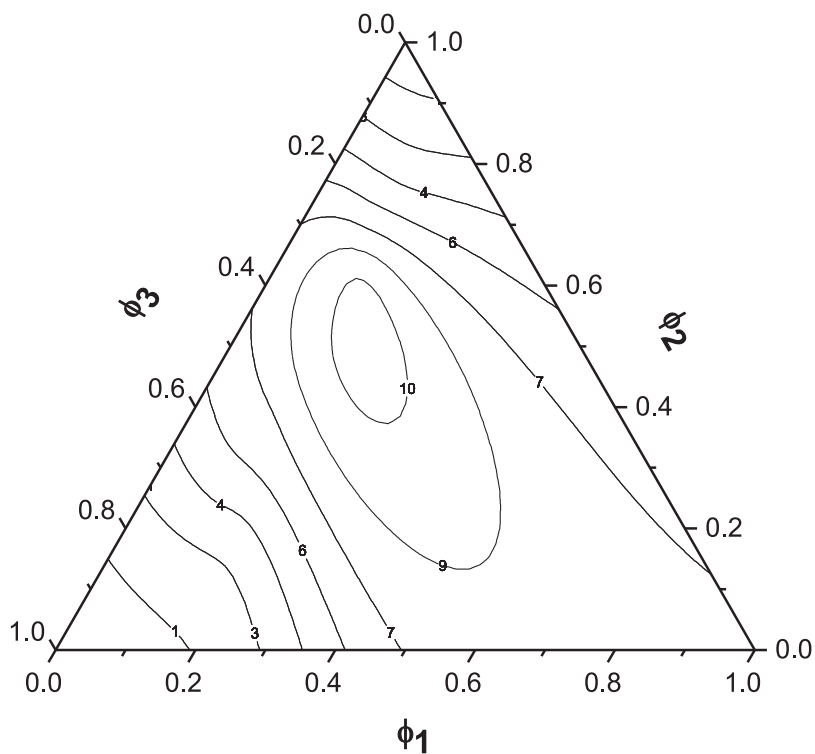


Fig. 5. Deviation in isentropic compressibility ($\Delta\kappa_{s123}$) data for N-methylcyclohexylamine (NMC) (1) + *p*-xylene (2) + 1-butanol (3) at 303.15 K.

Table 5

The standard deviation $\sigma(k_s)$ values of all the binary systems computed from Redlich-Kister equation at 303.15 K.

System	a_0 TPa-1	a_1	a_2	$\sigma(k_s)$
N-methyl cyclohexylamine (1)+ <i>p</i> -xylene (2)	-21.80	33.60	24.01	2
<i>p</i> -xylene (2)+1-propanol (3)	35.13	106.01	40.15	2
<i>p</i> -xylene (2)+ 1-butanol (3)	62.49	112.94	7.07	0
<i>p</i> -xylene (2)+ 1-pentanol (3)	80.95	138.16	32.51	0
N-methyl cyclohexylamine (1)+1-propanol (3)	-219.00	35.40	-68.30	2
N-methyl cyclohexylamine (1)+1-butanol (3)	-166.50	21.84	89.70	2
N-methyl cyclohexylamine (1)+1-pentanol (3)	-147.50	3.05	61.40	3

Table 6

Volume fractions of N-methylcyclohexylamine (ϕ_1), *p*-xylene (ϕ_2), density (ρ), speed of sound (u_{s123}), isentropic compressibility (k_{s123}), deviation in isentropic compressibility (κ_{s123}), deviation in isentropic compressibility computed from constituent binary data ($\kappa_{s123(b)}$) and $\Delta\kappa_{s123}$ values for ternary systems N-methylcyclohexylamine (NMC) (1) + *p*-xylene (2) + 1-alkanols (3).

Φ_1	Φ_2	P (g.cm ³)	U (m.s ⁻¹)	κ_{s123}	κ_{s123} TPa-1	$\kappa_{s123(b)}$	$\Delta\kappa_{s123}$
N-methylcyclohexylamine (NMC) (1) <i>p</i> -xylene (2) + 1-propanol (3)							
0.1587	0.1085	0.81490	1238	800	-29	-31	2
0.1709	0.1461	0.81796	1244	790	-29	-31	2
0.1127	0.7157	0.83005	1254	766	-33	-37	4
0.275	0.3488	0.83539	1271	741	-16	-22	6
0.2257	0.4171	0.83551	1267	745	-11	-17	6
0.0742	0.5685	0.83323	1248	771	6	-1	7
0.1667	0.6135	0.84110	1274	732	-2	-6	4
0.1916	0.6695	0.84498	1286	715	-3	-6	3
0.1471	0.7216	0.84520	1283	719	0	-3	3
0.1775	0.7766	0.84946	1298	699	-2	-4	2
0.1152	0.8466	0.84995	1295	702	-1	-2	1
0.0874	0.8766	0.85008	1292	705	0	-1	1
N-methylcyclohexylamine (NMC) (1) + <i>p</i> -xylene (2) + 1-butanol (3)							
0.1099	0.0629	0.81287	1250	787	-12	-13	1
0.1382	0.1278	0.81799	1258	772	-14	-16	2
0.157	0.1932	0.82036	1265	762	-12	-15	3
0.1047	0.2723	0.82267	1255	772	-2	-7	5
0.1167	0.3961	0.82930	1257	763	7	0	7
0.1208	0.4682	0.83275	1258	759	12	3	9
0.1317	0.5519	0.83710	1261	751	16	6	10
0.1305	0.6085	0.83958	1263	747	19	8	11
0.1056	0.6658	0.84089	1264	744	19	11	8
0.0937	0.7124	0.84245	1266	740	18	12	6
0.1229	0.7571	0.84606	1279	722	11	7	4
0.0953	0.8511	0.84933	1288	710	6	4	2
N-methylcyclohexylamine (NMC) (1) + <i>p</i> -xylene (2) + 1-pentanol (3)							
0.0611	0.0904	0.81599	1269	761	-5	-6	1
0.1238	0.1675	0.82324	1277	745	-7	-10	3
0.1086	0.2187	0.82439	1273	748	-2	-6	4
0.0754	0.2937	0.82548	1269	752	4	0	4
0.1106	0.362	0.83027	1271	746	8	2	6
0.122	0.4522	0.83374	1270	744	14	7	7
0.0734	0.5685	0.83667	1263	749	22	18	4
0.1975	0.6197	0.84438	1286	716	10	7	3
0.0747	0.6948	0.84204	1266	740	23	20	3
0.1082	0.7243	0.84484	1275	728	18	15	3
0.0523	0.7723	0.84430	1268	737	23	21	2
0.0729	0.8574	0.84905	1283	715	11	10	1

This suggests that Redlich-Kister equation is capable of giving good estimation of deviation in isentropic compressibility of ternary mixtures from that of constituent binaries [17,20,21].

The deviation in isentropic compressibility ($\Delta\kappa_{s123}$) data in the studied ternary mixtures is influenced by three factors: i) structure-breaking effects ii) structure making effects and iii) change in geometrical factors [2]. Structure breaking effects contribute to an increase in free spaces [22] between the molecules leading to positive deviation in compressibility. On the other hand, structure making effect and geometrical effect cause decrease in free spaces of the component molecules on mixing there by leading to negative deviation in isentropic compressibility. The actual deviation would depend up on

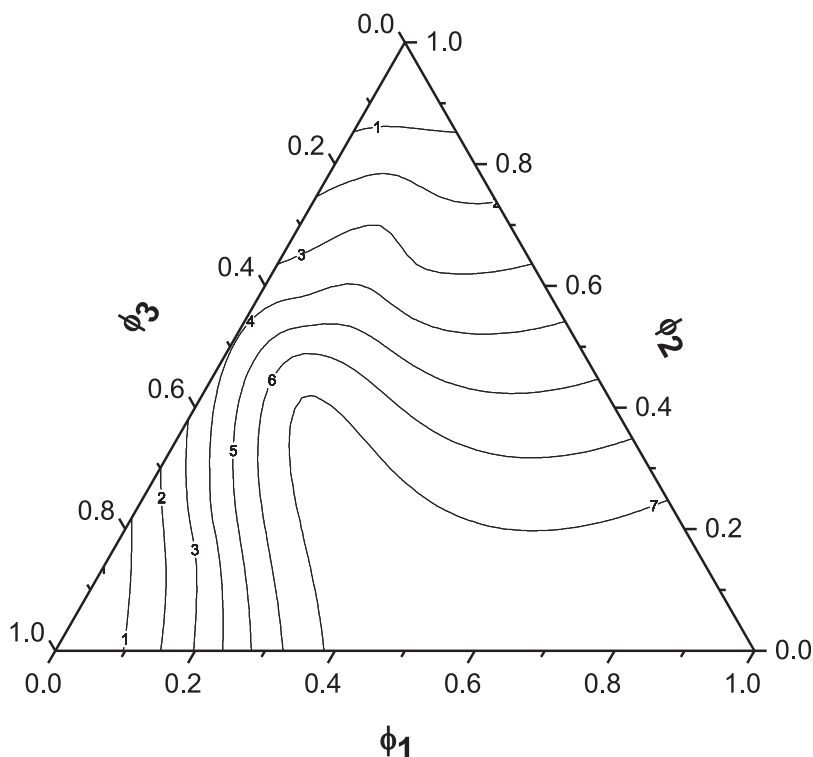


Fig. 6. Deviation in isentropic compressibility ($\Delta\kappa_{s123}$) data for N-methylcyclohexylamine (NMC) (1) + *p*-xylene (2) + 1-Pentanol (3) at 303.15 K.

Table 7

The standard deviation values $\sigma(\Delta V_{123}^E)$ and $\sigma(\Delta\kappa_{s123})$ for ternary systems of N- methylcyclohexylamine (NMC) (1) + *p*-xylene (2)+1-alkanols (3).

system	A $\text{cm}^3 \text{mol}^{-1}$	B	C	$\sigma(\Delta V_{123}^E)/\text{TPa}^{-1}$	A	B	C	$\sigma(\Delta\kappa_{s123})$
NMC (1) + <i>p</i> -xylene (2)+ 1-propanol(3)	0.639	2.026	-11.054	0.003	243.51	609.37	-4292.23	3
NMC (1) + <i>p</i> -xylene (2) + 1-butanol(3)	0.617	-11.177	-92.757	0.005	389.68	1843.89	-13821.03	1
NMC (1) + <i>p</i> -xylene (2) + 1-pentanol(3)	691.209	-1.737	-64.668	0.006	298.12	29.10	-20220.44	0

the balance between these two opposing effects. The experimental $\Delta\kappa_{s123}$ values indicate that structure breaking effect is dominant in all the three ternary mixtures.

The experimental ΔV_{123}^E and $\Delta\kappa_{s123}$ data were fitted to the following equation proposed by Redlich-Kister [8]:

$$\Delta V_{123}^E/\text{cm}^3 \text{mol}^{-1} = x_1 x_2 x_3 [A + B x_1 (x_2 - x_3) + C x_1^2 (x_2 - x_3)^2] \quad (11)$$

$$\Delta\kappa_{s123}/\text{TPa}^{-1} = \phi_1 \phi_2 \phi_3 [A + B \phi_1 (\phi_2 - \phi_3) + C \phi_1^2 (\phi_2 - \phi_3)^2] \quad (12)$$

where A , B and C are the ternary constants which were calculated by least square method. The values of coefficients were inturn used to compute standard deviation $\sigma(Y_{123}^E)$.

$$\sigma(Y_{123}^E) = \left[\frac{\sum (Y_{123}^E \text{exp} - Y_{123}^E \text{cal})^2}{(m - n)} \right]^{1/2} \quad (13)$$

where $\sigma(Y_{123}^E) = \Delta V_{123}^E$ (or) $\Delta\kappa_{s123}$

' m ' is the total number of experimental points and ' n ' is the number of coefficients in Equation (11) and (12) and the values of ternary constants A , B and C along with their standard deviation values were given in Table 7.

4. Conclusions

In the present investigation, excess volume, sound speed and deviation in isentropic compressibility data were reported for three ternary mixtures of N-methylcyclohexylamine (NMC) + *p*-xylene + 1-propanol or + 1-butanol + 1-pentanol at

303.15 K and atmospheric pressure. Experimental excess volume data were found to be negative as a function of composition. The negative V^E_{123} data for the studied systems follow the order: 1-propanol > 1-butanol > 1-pentanol. Whereas (Δk_{s123}) data were found to be positive for all the ternary mixtures. The experimental ternary (V^E_{123}) data were compared with theoretical models proposed by Redlich-Kister, Kohler, Tsao-Smith and Hwang et al. and found in good agreement between the predicted and experimental data. The V^E_{123} Δk_{s123} parameters were analyzed in terms of intermolecular interactions between component molecules.

Declaration of Competing Interest

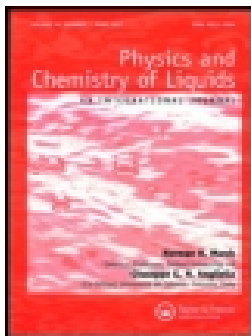
The authors declare that they have no known competing financial interests or personal relationships that could have appeared to influence the work reported in this paper.

Acknowledgements

The authors Ch. Bharath Kumar and K. Siva Kumar are gratefully acknowledge University Grants Commission (UGC), New Delhi for the financial support (MRP-MAJOR-CHEM-2013-24358). The authors express sincere thanks to Prof. P. Venkateswarlu, Dept. of Chemistry, SV University, Tirupati for giving valuable suggestions in the preparation of the present manuscript.

References

- [1] L. Venkatramana, K. Sreenivasulu, K. Sivakumar, K. Dayananda Reddy, Thermodynamic properties of binary mixtures containing 1-alkanols, *J. Therm. Anal. Calorim.* 115 (2014) 1829–1834.
- [2] L. Venkatramana, K. Sivakumar, V. Govinda, K. Dayananda Reddy, Study on solution properties of some industrially important solvents with an aromatic alcohol, *J. Mol. Liq.* 186 (2013) 163–170.
- [3] K. Sreenivasulu, V. Govinda, P. Venkateswarlu, K. Sivakumar, Thermodynamic properties of non-electrolyte solutions, *J. Therm. Anal. Calorim.* 115 (2014) 1805–1811.
- [4] P. Venkatesu, G. Chandra Sekhar, M.V. Prabhakara Rao, T. Hofman, Excess molar volumes of N, N-dimethylformamide+ 2-pentanone+ alkan-1-ols mixed solvent systems at 303.15 K, *Thermochim. Acta* 443 (2006) 62–71.
- [5] P.S. Slobodan, L.K. Mirjana, R.R. Ivona, D.D. Bojan, Effect of temperature on the excess molar volumes of some alcohol + aromatic mixtures and modelling by cubic EOS mixing rules, *Fluid Phase Equilib* 239 (2006) 69–82.
- [6] P.S. Slobodan, L.K. Mirjana, R.R. Ivona, D.D. Bojan, Densities and excess molar volumes of alcohol+ cyclohexylamine mixtures, *J. Serb. Chem. Soc.* 74 (2009) 1303–1318.
- [7] W.E. Acree, in: *Thermodynamics of non-electrolyte solutions*, Academic Press, Orlando, 1984, p. 64.
- [8] O. Redlich, A.T. Kister, Algebraic representation of thermodynamic properties and the classification of solutions, *Ind. Eng. Chem.* 40 (1948) 345–348.
- [9] C.A. Hwang, J. Holste, K.R. Hall, G.A. Mansoori, A simple relation to predict or to correlate the excess functions of multi component mixtures, *Fluid Phase Equilib* 62 (1991) 173–189.
- [10] J.A. Riddick, W.B. Bunger, T.K. Sakano, *Techniques of Chemistry*, 4th edition, Wiley Inter Science, New York, 1986.
- [11] A.I. Vogel, *A text book of practical organic chemistry*, 5th edition, John Wiley, New York, 1989.
- [12] C. Chennarayappa, K. Rambabu, P. Venkateswarlu, G.K. Raman, *Acoust. Lett.* 15 (1991) 83–86.
- [13] J.A. Al-Kandary, A.S. Al-Jimaz, A.H.M. Abdul-Latif, Viscosities, densities, and speeds of sound of binary mixtures of Benzene, Toluene, o-Xylene, m-Xylene, p-Xylene, and Mesitylene with Anisole at (288.15, 293.15, 298.15, and 303.15) K, *J. Chem. Eng. Data* 51 (2006) 2074–2082.
- [14] J. Rajasekhar, P.R. Naidu, Speed of sound of 1,3 dichlorobenzene + methyl ethyl ketone + 1-alkanols at 303.15 K, *J. Chem. Eng. Data* 41 (1996) 373–375.
- [15] V. Syamala, K. Sivakumar, P. Venkateswarlu, Volumetric behaviour of ternary organic liquid mixtures containing dimethylsulphoxide, 1, 2-dichlorobenzene and 1-alkanols at 303.15 K, *J. Mol. Liq.* 136 (2007) 29–34.
- [16] C. Chennarayappa, K. Rambabu, P. Venkateswarlu, G.K. Raman, Excess volumes of binary liquid mixtures of N-methylcyclohexylamine, *Indian J. Chem. Sci.* 5 (1991) 73–76.
- [17] L. Venkatramana, C. Narasimha Rao, R.L. Gardas, K.S. Kumar, FT-IR study of excess thermodynamic properties of binary liquid mixtures of p-xylene with 1-alkanols at 303.15 K, *J. Mol. Liq.* 207 (2015) 171–176.
- [18] M.A. Saleh, M. Habibullah, M. Shamsuddin Ahmed, M. Ashraf Uddin, S.M.H. Uddin, M. Afsar Uddin, F.M. Khan, Excess molar volumes of the systems m-xylene + 1-propanol, +2-propanol, +1-butanol, +2-methyl-2-propanol, *Phys. Chem. Liq.* 43 (2005) 139–148.
- [19] B.L. Yadav, S. Maken, K.C. Karla, K.C. Singh, Excess volumes of (an alkanol+ an aromatic hydrocarbon) at the temperature 308.15 K, *J. Chem. Thermodyn.* 25 (1993) 1345–1350.
- [20] C.L. Prabhavathi, K. Sivakumar, P. Venkateswarlu, G.K. Raman, Speed of Sound and Isentropic Compressibilities of N-Methylcyclohexylamine with Benzene and Substituted Benzenes at 303.15 K, *Phys. Chem. Liq.* 38 (2000) 705–712.
- [21] C. Chennarayappa, K. Rambabu, P. Venkateswarlu, G.K. Raman, Ultrasonic studies in binary mixtures of n-methyl cyclohexylamine with alcohols at 303.15 K, *Acoust. Lett.* 15 (1999) 83–86.
- [22] B. Jacobson, Ultrasonic velocity in liquids and liquid mixtures, *J. Chem. Phys.* 20 (1952) 9271–928.



Insights into non-ideal behaviour of benzyl alcohol with (C₂-C₄) carboxylic acids through volumetric, ultrasonic and ATR-FTIR spectroscopic studies

P. Bhanuprakash , Ramesh L. Gardas , R. Prathibha , K. Sivakumar & N.V.V. Jyothi

To cite this article: P. Bhanuprakash , Ramesh L. Gardas , R. Prathibha , K. Sivakumar & N.V.V. Jyothi (2020): Insights into non-ideal behaviour of benzyl alcohol with (C₂-C₄) carboxylic acids through volumetric, ultrasonic and ATR-FTIR spectroscopic studies, Physics and Chemistry of Liquids, DOI: [10.1080/00319104.2020.1808654](https://doi.org/10.1080/00319104.2020.1808654)

To link to this article: <https://doi.org/10.1080/00319104.2020.1808654>

 View supplementary material 

 Published online: 18 Aug 2020.

 Submit your article to this journal 

 Article views: 15

 View related articles 

 View Crossmark data 



ARTICLE



Insights into non-ideal behaviour of benzyl alcohol with (C₂-C₄) carboxylic acids through volumetric, ultrasonic and ATR-FTIR spectroscopic studies

P. Bhanuprakash ^{a,b}, Ramesh L. Gardas ^c, R. Prathibha^a, K. Sivakumar^d and N.V.V. Jyothi^a

^aDepartment of Chemistry, S.V. University, Tirupati, India; ^bDepartment of Chemistry, S.V.C.R. Govt. Degree College, Palamaner, India; ^cDepartment of Chemistry, Indian Institute of Technology Madras, Chennai, India; ^dDepartment of Chemistry, S.V. Arts Degree & P.G. College (T.T.D'S), Tirupati, India

ABSTRACT

In the present work, experimental density (ρ) and speed of sound (u) data for the binary mixtures of benzyl alcohol with acetic acid, propionic acid, and n-butyric acid have been reported over the complete range of mole fraction at $298.15 \text{ K} \leq T \leq 313.15 \text{ K}$. Excess volumes (V^E), excess isentropic compressibilities (κ_s^E), excess partial molar volumes (\bar{V}_i^E), and excess partial molar volumes at infinite dilution ($\bar{V}_i^{E,\infty}$) have been computed from the experimental data. The excess thermodynamic properties are found to be negative over the entire range of composition at the investigated temperatures. The temperature dependence of the excess thermodynamic properties has been investigated. All the excess functions are correlated with the Redlich-Kister equation. Further, attenuated total reflection Fourier transform infrared (ATR-FTIR) spectra for the studied binary solutions have been recorded at the equimolar composition to evaluate the extent of cross-association between component molecules through intermolecular hydrogen bonding.

ARTICLE HISTORY

Received 28 February 2020
Accepted 7 August 2020

KEYWORDS

Benzyl alcohol; acetic acid; propionic acid; n-Butyric acid; excess volume; hydrogen bonding

1. Introduction

The sound knowledge on structure-property relationships of binary liquid mixtures through accurate density (ρ) and speed of sound (u) measurements as a function of composition has relevance in industrial, chemical engineering and technological processes not only in development of efficient separation processes, transport equipment but also in the design of engineering calculations involving chemical purification, heat transfer, mass transfer, fluid flow, etc. [1–3]. The study on excess thermodynamic properties of mixed solvents is one of the excellent methods to understand the intermolecular forces qualitatively and quantitatively and also the geometrical effects existing between the components with different molecular sizes, shapes and chemical nature [4,5]. Further, the understanding of thermo-physical (ρ and u) and thermodynamic properties (V^E and κ_s^E) is indispensable in the development of thermodynamic models, namely, group contribution methods, reliable correlations and to test the existing solution theories [6,7]. The investigation on excess thermodynamic properties of binary solutions also contributes a huge data to thermodynamic data bank [8].

The carboxylic acids (CA) are considered to be highly polar protic solvents as indicated by their high dipole moments. The strongly polarised hydroxyl group (-O-H) and carbonyl group

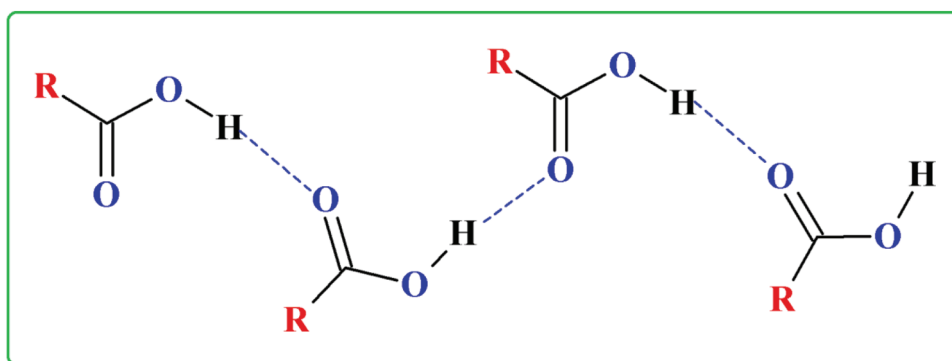


Figure 1. Self-association of carboxylic acids through hydrogen bonding.

($>C=O$) of carboxylic acid functions as hydrogen-bond donors and hydrogen-bond acceptors respectively. In their pure state, they show a high degree of self-association through hydrogen bonding and predominantly exist as a chain structure [9] as depicted in Figure 1. The hydrogen bonding interactions appear to play a more dominant role in strong self-association of carboxylic acids and hydrophobic interactions also have increasing roles in self-association with longer alkyl chain carboxylic acids [10]. Carboxylic acids are one of the versatile classes of raw materials used in a wide range of industrial applications such as manufacture of rubber, pharmaceuticals, biodegradable plastics, and in separation processes. They find applications as natural colourants, acidulants, food preservatives, flavouring agents, fungicides, insecticides, cleaning agents, buffers, etc. [11–13]. Likewise, they serve as catalysts in the synthesis of biodiesel. Acetic and propionic acids are used in the feed industry to control mould growth. Due to the unpleasant odour, butyric acid is found to use as a fishing bait additive.

Benzyl alcohol (Bn-OH) is a polar protic primary alcohol in which the hydroxyl group ($-O-H$) serves as both hydrogen-bond donor and acceptor. In the native state, it is strongly self-associated through intermolecular hydrogen bonding [14,15]. Bn-OH is widely used as a solvent due to its favourable properties like low toxicity, good polarity, and low vapour pressure. It is primarily used as a solvent for paints, inks, gelatin, epoxy resin coatings, lacquers, shellac, cellulose acetate [15,16]. It serves as an embedding material in microscopy, as a preservative in cosmetics and medications, as an antimicrobial agent in the pharmaceutical industry [17,18]. It is a well-known precursor to several esters, used in the manufacture of soaps, skin lotions, perfumes, topical creams, shampoos, and flavour industries. It is also utilised as a local anaesthetic, insect repellent, degreaser and as flavour enhancer in e-cigarettes.

The favourable properties and diversified applications of the carboxylic acids (CA) and benzyl alcohol (Bn-OH) in several industries have motivated to elucidate the nature and extent of intermolecular interactions through volumetric, acoustic studies in the binary mixtures of Bn-OH with (C_2-C_4) carboxylic acids at different temperatures. For the effective utilisation and also to explore new industrial applications of the investigated solvents, it is essential to have sound knowledge of their physicochemical and thermodynamic properties. The proper understanding of the information about chemical structures and molecular interaction changes occurring on mixing the molecular solvents is necessary as it provides an opportunity for the design and development of new processes and equipment [19]. Moreover, the excess property measurements in highly non-ideal binary systems containing carboxylic acids assist in understanding the hydrophobic and hydrogen bonding interactions between the components of the mixtures. Further, the present study aims at investigating the influence of alkyl chain length of carboxylic acids, temperature and composition on excess thermodynamic

properties (V^E , κ_s^E , \bar{V}_i^E and $\bar{V}_i^{E,\infty}$) of binary solutions to establish the relationship between thermodynamic properties and the molecular structures of components.

Many researchers have reported the thermodynamic properties for the binary mixtures of benzyl alcohol with (C₁–C₄) 1-alkanols [20], (C₅–C₁₀) 1-alkanols [21,22], 2-propanol [23], isomeric butanols [7], alkoxyalkanols [24], isomeric cresols [25], poly(propylene glycol) [26], chloroalkanes [27], isomeric chlorobenzenes [28], monocyclic aromatics [14], isomeric chloro and nitrotoluenes [29], N,N-dimethylacetamide [30], N,N-dimethylformamide [31], dimethylsulfoxide [32], (C₂–C₄) alkylacetates [15], ethylchloroacetate [33], vinyl acetate [34], t-butyl acetate [34], benzyl acetate [16], and 1,2-butanediol [35]. A comprehensive survey of the literature shows that no systematic data is currently available on the thermo-physical and excess thermodynamic properties for the binary solutions studied.

In the present study, experimental measurements on densities (ρ) and speeds of sound (u), excess volumes (V^E), excess isentropic compressibilities (κ_s^E), excess partial molar volumes (\bar{V}_i^E) and excess partial molar volumes at infinite dilution ($\bar{V}_i^{E,\infty}$) over the whole range of concentration for the binary solutions of Bn-OH and (C₂–C₄) homologous series of carboxylic acids at 298.15 K \leq T \leq 313.15 K, every 5 K, and atmospheric pressure have been reported. Further, attenuated total reflection-Fourier transform infrared (ATR-FTIR) spectra for the studied pure liquids and their equimolar binary mixtures have been recorded at room temperature to interpret the strength of the hydrogen bonding interactions between Bn-OH and CA molecules in the mixed systems. The experimental results emanating from this work have been discussed in terms of cross-association through hydrogen bonding and packing effects between Bn-OH and carboxylic acids.

2. Experimental

2.1. Materials

Benzyl alcohol (Bn-OH, Merck, purity \geq 99.5%), acetic acid (AA, Merck, purity \geq 99.8%), propionic acid (PA, Sigma-Aldrich, purity \geq 99.5%) and n-butyric acid (n-BA, SRL, purity \geq 99.5%) of analytical reagent grade were purchased and used in the sample preparation without further purification. The description of the chemicals used in this work including the percentage of water content was presented in Table 1. Before the experimental measurements, the chemicals were degassed ultrasonically and dried over freshly activated 4A° molecular sieves for about 48 h. To assess the purity of the liquid components, their experimental densities (ρ) and speeds of sound (u) were compared with the corresponding literature values [7,13,16,34–40] at 298.15 K \leq T \leq 313.15 K and are shown in Table 2. The experimental ρ and u values for pure chemicals are found to be in the best accordance with the published values.

Table 1. Description of chemicals used in the study.

Name of the chemical	CAS No	Molar mass (g·mol ⁻¹)	Source	Mass fraction purity by GC*	Water content by KF (%)
Benzyl alcohol	100-51-6	108.14	Merck, India	\geq 0.995	\leq 0.1
Acetic acid	64-19-7	60.05	Merck, India	\geq 0.998	\leq 0.2
Propionic acid	79-09-4	74.08	Sigma-Aldrich, India	\geq 0.995	\leq 0.2
n-Butyric acid	107-92-6	88.11	SRL, India	\geq 0.995	\leq 0.1

*The purity is reported by supplier.

Table 2. Experimental density (ρ) and speed of sound (u) values of the pure liquid compounds and their corresponding literature values from T/K = 298.15 to 313.15 at 0.1 MPa pressure.

Liquid	T (K)	$\rho(\text{g.cm}^{-3})$		$u (\text{m.s}^{-1})$	
		Exp.	Lit	Exp.	Lit
Benzyl alcohol (Bn-OH)	298.15	1.041271	1.041216 ^a 1.04138 ^b 1.04134 ^c	1525.21	1525.17 ^a
	303.15	1.037374	1.037352 ^a 1.03750 ^b 1.03745 ^c	1509.59	1509.34 ^a
	308.15	1.033481	1.033474 ^a 1.03363 ^b	1493.71	1493.62 ^a
	313.15	1.029586	1.029583 ^a 1.02961 ^b 1.02971 ^c	1478.09	1478.03 ^a
Acetic acid (AA)	298.15	1.043931	1.04413 ^d 1.0427 ^e	1134.19	1135.7 ^d
	303.15	1.038262	1.03848 ^d 1.0371 ^e 1.03844 ^f	1117.41	1118.4 ^d 1117.5 ^f
	308.15	1.032623	1.03283 ^d 1.0314 ^e 1.03261 ^f	1100.62	1101.2 ^d 1102.4 ^f
	313.15	1.026981	1.02718 ^d 1.0258 ^e 1.02704 ^f	1083.43	1084.0 ^d 1084.4 ^f
Propanoic acid (PA)	298.15	0.988111	0.98794 ^d 0.9882 ^e 0.98848 ^g	1146.51	1146.0 ^d 1146.7 ^g
	303.15	0.982809	0.98254 ^d 0.9829 ^e 0.98307 ^g	1127.39	1127.1 ^d 1127.7 ^g
	308.15	0.977468	0.97714 ^d 0.9774 ^e 0.97767 ^g	1108.61	1108.3 ^d 1108.9 ^g
	313.15	0.972122	0.97175 ^d 0.9721 ^e 0.97227 ^g	1089.78	1089.6 ^d 1090.2 ^g
n-Butyric acid (n-BA)	298.15	0.952791	0.95281 ^h 0.95282 ⁱ	1176.68	1176.9 ^h
	303.15	0.947892	0.94794 ^h 0.94784 ⁱ 0.94789 ^f	1158.09	1158.2 ^h 1159.0 ^f
	308.15	0.942904	0.94292 ^h 0.94288 ⁱ 0.94319 ^f	1139.41	1139.7 ^h 1140.1 ^f
	313.15	0.937966	0.93805 ^h 0.93791 ⁱ 0.93856 ^f	1121.08	1121.3 ^h 1122.0 ^f

^aRef [7,35]. ^bRef [34]. ^cRef [16]. ^dRef [36]. ^eRef 37. ^fRef [38]. ^gRef [39]. ^hRef [40]. ⁱRef [13].
Standard uncertainties are $u(\rho) = 5 \times 10^{-5} \text{ g.cm}^{-3}$, $u(u) = 0.5 \text{ m.s}^{-1}$, and $u(T) = 0.01 \text{ K}$.

2.2. Methods

2.2.1. Sample preparation

The homogeneous binary mixtures of Bn-OH with (C₂-C₄) carboxylic acids were prepared gravimetrically covering the complete range of mole fraction from 0.1 to 0.9 in a clean, airtight screw-capped glass vial. The mass of liquids is measured by using a digital electronic balance (Sartorius CPA225D) with an accuracy of $\pm 1 \times 10^{-5} \text{ g}$. Density and speed of sound measurements were carried immediately on the same day of sample preparation to avoid loss due to evaporation. Considering the mass of each component, the uncertainty in the mole fraction $u(x_1)$ of mixtures was estimated to be less than $\pm 5 \times 10^{-5}$.

2.2.2. Density and speed of sound measurements

The densities (ρ) and speeds of sound (u) of pure Bn-OH and its mixtures with (C_2 - C_4) carboxylic acids were automatically measured at $T = (298.15\text{--}313.15)$ K with a temperature step of 5 K and at 0.1 MPa pressure using vibrating U-tube digital density and sound velocity metre (Anton-Paar DSA 5000 M). The temperature of the sample in the density and sound velocity cells of the apparatus is controlled by a built-in Peltier thermostat with stability of ± 0.01 K. It measures the period of oscillation of a vibrating U-shaped tube filled with a sample, which is directly related to density (ρ) of the sample. The speed of sound (u) of a liquid sample is determined using a time propagation technique, in which the sample is sandwiched between two piezoelectric ultrasound transducers. One transducer emits sound waves through the sample at a frequency of 3 MHz and a second transducer receives those waves. The ratio of the known distance between the transmitter and receiver with the measured propagation time of the sound wave results in the speed of sound [41]. Prior to carrying out the measurements, the calibration of the instrument was done with dry air, Millipore quality water as standards at atmospheric pressure. The uncertainty in the measurement of density (ρ) and speed of sound (u) values is found to be $\pm 5 \times 10^{-5}$ g.cm⁻³ and ± 0.5 m.s⁻¹ respectively.

2.2.3. Infrared measurements

Fourier-transform infrared (FTIR) spectra of the pure components and the equimolar binary mixtures of benzyl alcohol with (C_2 - C_4) carboxylic acids were recorded using Alpha-ATR-FTIR spectrometer (Bruker, Germany). ATR-FTIR interferometer containing a single-point reflection sampling module was equipped with ZnSe crystal onto which a drop of the homogeneous sample has been placed to record the spectra at room temperature in the region 4000 – 600 cm⁻¹ with 4.0 cm⁻¹ spectral resolution.

3. Results and discussion

3.1. Densities and excess volumes (V^E)

Densities (ρ) are measured for the binary mixtures Bn-OH with (C_2 - C_4) carboxylic acids over the entire concentration range at $T = (298.15$ to $313.15)$ K, with a temperature step of 5 K to understand the extent of intermolecular interactions. The experimental ρ values are listed in Table 3. At a fixed temperature, the densities (ρ) of the investigated binary systems increase with an increase in the concentration of Bn-OH (x_1) except for the (Bn-OH + AA) system as Bn-OH is much denser than carboxylic acids. The increase in ρ values with an increase in x_1 is due to the strengthening of Bn-OH and carboxylic acid interactions. From Table 3, it is observed that the ρ values of (Bn-OH + AA) increases, reaches a maximum at $x_1 = 0.3750$ and then decreases continuously. This suggests that the specific interactions between Bn-OH and AA are relatively stronger between $0.25 \leq x_1 \leq 0.45$ than that in acetic acid-rich and benzyl alcohol-rich regions. A similar type of behaviour has been observed in the binary solutions of acetic acid with water [42–44] and 1-butyl-3-methylimidazolium thiocyanate ionic liquid [45]. Further, at constant x_1 , ρ values of the investigated systems decrease with an increase in the temperature. This might be due to an increase in the translational energy of the molecules with temperature, which increases the molecular agitations, leading to a decrease in intermolecular interactions in the mixed solutions.

The excess volumes (V^E) were evaluated for the three investigated mixtures containing Bn-OH and (C_2 - C_4) carboxylic acids according to the equation:

$$V^E = \frac{x_1 M_1 + x_2 M_2}{\rho} - \left[\frac{x_1 M_1}{\rho_1} + \frac{x_2 M_2}{\rho_2} \right] \quad (1)$$

where M_1 and M_2 , x_1 and x_2 , ρ_1 and ρ_2 represent the molar mass, mole fraction, and density of Bn-OH and (C_2 - C_4) carboxylic acids respectively, ρ_m represents the density of the binary mixture.

Table 3. Experimental values of densities ($\rho/\text{g}\cdot\text{cm}^{-3}$) and excess volumes ($V^E/\text{cm}^3\cdot\text{mol}^{-1}$) as a function of mole fraction of Bn-OH (x_1), for the binary solutions of Bn-OH with AA, PA and n-BA from T/K = 298.15 to 313.15 and 101.3kPa pressure.

x_1	$\rho/\text{g}\cdot\text{cm}^{-3}$				$V^E/\text{cm}^3\cdot\text{mol}^{-1}$			
	T/K = 298.15	303.15	308.15	313.15	T/K = 298.15	303.15	308.15	313.15
0.0000	1.04393	1.03826	1.03262	1.02698	0.000	0.000	0.000	0.000
0.1283	1.04558	1.04034	1.03512	1.02989	-0.134	-0.139	-0.143	-0.148
0.2455	1.04623	1.04130	1.03638	1.03146	-0.216	-0.224	-0.231	-0.239
0.3750	1.04625	1.04159	1.03694	1.03228	-0.265	-0.273	-0.282	-0.290
0.4435	1.04602	1.04149	1.03696	1.03243	-0.273	-0.282	-0.291	-0.300
0.5293	1.04552	1.04113	1.03675	1.03236	-0.265	-0.274	-0.283	-0.293
0.6243	1.04485	1.04058	1.03632	1.03206	-0.241	-0.249	-0.257	-0.266
0.7300	1.04393	1.03978	1.03565	1.03152	-0.193	-0.199	-0.206	-0.213
0.8329	1.04294	1.03890	1.03487	1.03084	-0.129	-0.133	-0.138	-0.143
0.9132	1.04213	1.03817	1.03422	1.03026	-0.069	-0.073	-0.076	-0.079
1.0000	1.04127	1.03737	1.03348	1.02959	0.000	0.000	0.000	0.000
0.0000	0.98811	0.98281	0.97747	0.97212	0.000	0.000	0.000	0.000
0.1052	0.99909	0.99401	0.98890	0.98377	-0.276	-0.282	-0.288	-0.293
0.2023	1.00776	1.00283	0.99791	0.99297	-0.467	-0.474	-0.484	-0.493
0.3067	1.01559	1.01087	1.00612	1.00137	-0.601	-0.612	-0.623	-0.636
0.3999	1.02136	1.01685	1.01227	1.00769	-0.655	-0.673	-0.687	-0.701
0.4587	1.02453	1.02010	1.01561	1.01112	-0.664	-0.682	-0.696	-0.711
0.5620	1.02921	1.02492	1.02062	1.01629	-0.627	-0.645	-0.662	-0.678
0.6612	1.03286	1.02868	1.02449	1.02030	-0.541	-0.556	-0.571	-0.587
0.7790	1.03633	1.03227	1.02821	1.02414	-0.385	-0.396	-0.408	-0.420
0.9056	1.03933	1.03537	1.03142	1.02747	-0.173	-0.179	-0.185	-0.191
1.0000	1.04127	1.03737	1.03348	1.02959	0.000	0.000	0.000	0.000
0.0000	0.95279	0.94789	0.94290	0.93797	0.000	0.000	0.000	0.000
0.1083	0.96552	0.96077	0.95594	0.95115	-0.204	-0.211	-0.217	-0.223
0.2101	0.97698	0.97236	0.96766	0.96301	-0.373	-0.383	-0.393	-0.404
0.3145	0.98795	0.98347	0.97895	0.97447	-0.494	-0.509	-0.526	-0.544
0.4116	0.99742	0.99311	0.98875	0.98441	-0.555	-0.578	-0.601	-0.623
0.5010	1.00551	1.00132	0.99708	0.99286	-0.568	-0.594	-0.620	-0.645
0.6128	1.01475	1.01070	1.00659	1.00249	-0.523	-0.550	-0.575	-0.601
0.7171	1.02258	1.01860	1.01459	1.01059	-0.424	-0.448	-0.471	-0.495
0.8238	1.02991	1.02600	1.02208	1.01816	-0.277	-0.295	-0.314	-0.333
0.9110	1.03561	1.03172	1.02783	1.02393	-0.141	-0.152	-0.163	-0.173
1.0000	1.04127	1.03737	1.03348	1.02959	0.000	0.000	0.000	0.000

The standard uncertainties are $u(x) = 5 \times 10^{-5}$, $u(\rho) = 5 \times 10^{-5} \text{ g}\cdot\text{cm}^{-3}$, $u(T) = 0.01 \text{ K}$, and $u(V^E) = 0.005 \text{ cm}^3\cdot\text{mol}^{-1}$

The excess thermodynamic properties could provide useful insights into the degree of non-ideality of a binary solution. Generally, the sign and magnitude of excess volumes of the mixed solutions depend on the relative strength of the following volume contraction and expansion factors [12,15,43]:

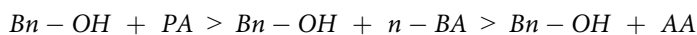
The factors that lead to volume contraction on mixing the components are:

- (i) The predominance of strong specific interactions like charge-dipole, hydrogen bonds, dipole-dipole, dipole-induced dipole interactions, etc. between unlike components (chemical contribution).
- (ii) Favourable geometrical fitting among the component molecules or accommodation of one component into others interstices (structural contribution).

The factors that lead to volume expansion on mixing the components are:

- (i) Disruption of the molecular associates (chemical contribution).
- (ii) Weak London dispersion forces between the components (physical contribution).
- (iii) Steric hindrance caused by the structure of the component molecules.
- (iv) Unfavourable geometrical fitting between the mixed components (structural contribution).

The excess volumes (V^E) against the mole fraction of Bn-OH (x_1) for the binary systems at T = (298.15 to 313.15) K, are plotted in Figure 2–4 and these values are listed in Table 3. A perusal of V^E data reveals that the property was negative for all the systems studied over the complete range of composition at the investigated temperatures. The magnitude of excess volumes (V^E) at a fixed temperature and composition varies in the following order:



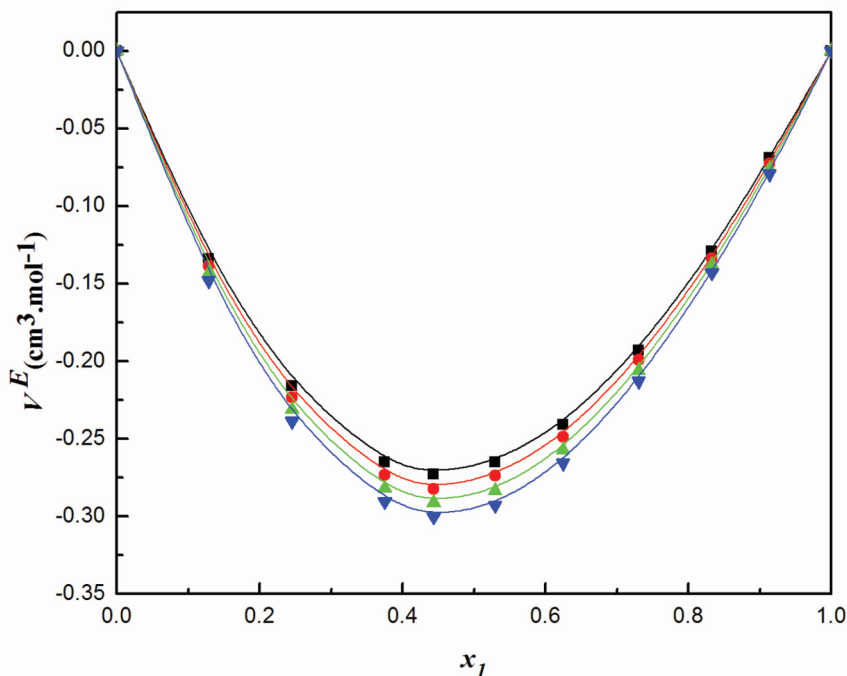


Figure 2. Plot of Excess volumes (V^E) vs. mole fraction (x_1) for Bn-OH (1) + AA (2) binary system at $T = 298.15$ K (■), 303.15 K (●), 308.15 K (▲) and 313.15 K (▼).

The negative V^E reveals that the specific interactions between Bn-OH and CA are stronger than between similar component molecules in their pure state. During mixing of Bn-OH with CA, the following volume contraction and expansion factors occur simultaneously: (a) disruption of associated structure of the pure benzyl alcohol through the breaking of hydrogen bonds, (b) rupture of hydrogen bonding interactions in self-associates of carboxylic acids, (c) formation of a cross hydrogen bond and new $-H \cdots \pi$ interaction between Bn-OH and carboxylic acids [20] and (d) interstitial accommodation (packing effect) of carboxylic acids in $\pi \cdots \pi$ and hydrogen-bonded and benzyl alcohol aggregates. The volume expansion factors (a) and (b) provide a positive contribution to V^E and the volume contraction factors (c) and (d) make a negative contribution to V^E . The actual V^E values for the studied systems are a consequence of the balance between the two volume expansion and contraction factors that occur due to mixing. The obtained negative excess volume (V^E) data points to the fact that the volume contraction factors (c) and (d) dominate over the volume expansion factors (a) and (b) in these systems at the investigated temperatures. Hence, the cross-association through H-bonding between -O-H group of Bn-OH and -O-H or $>C=O$ group of carboxylic acids and the favourable packing effects due to significant differences in the free volume size, and molar volume between the components are the two factors that govern the molecular structures of studied systems.

The V^E data is found to be more negative for Bn-OH + PA system than Bn-OH + AA and Bn-OH + BA systems. The magnitude of V^E for the mixtures follows the same order as pK_a values of carboxylic acids which are 4.76, 4.87, and 4.82 for AA, PA, and n-BA respectively [46]. A similar trend in V^E values has been reported for the mixed solutions of carboxylic acids with methanol [47], acetonitrile [48] and acetophenone [49]. The dimerisation constant (K_d) of carboxylic acids tends to increase with an increase in the alkyl chain length of carboxylic acids. According to Lark et al. [50], the increased dimerisation constant of PA ($K_d = 2.301$ at $T = 298.15$ K) than that of AA ($K_d = 1.982$ at $T = 298.15$ K) could reduce the positive contribution to V^E , resulting in more negative V^E for Bn-

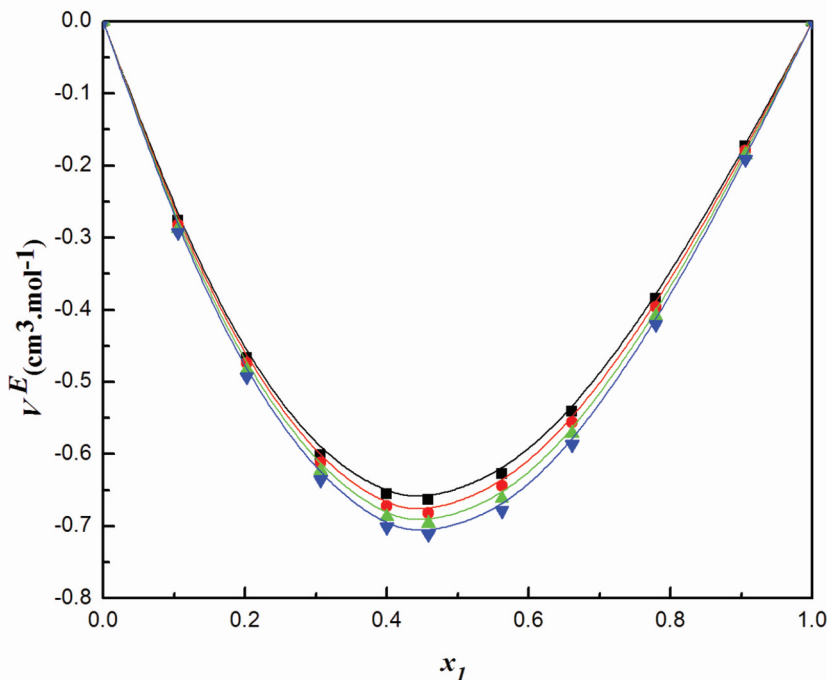


Figure 3. Plot of Excess volumes (V^E) vs. mole fraction (x_1) for Bn-OH (1) + PA (2) binary system at $T = 298.15$ K (■), 303.15 K (●), 308.15 K (▲) and 313.15 K (▼).

OH + PA. The more negative V^E for Bn-OH + PA than Bn-OH + AA is attributed to more positive inductive effect (+I) of the larger $-C_2H_5$ alkyl group in PA, which increases electron density on the oxygen atoms and consequently resulting in the formation of an energetically more favoured cross H-bonding between Bn-OH and PA. The stronger cross H-bonding in Bn-OH + PA is also evidenced by its FT-IR data. Similarly, one would expect the large negative V^E for Bn-OH + BA due to the larger +I-effect of its $-C_3H_7$ group. But, the V^E values for Bn-OH + BA system are found to be less negative than for the mixtures of BnOH + PA. In addition to the +I-effect of CA, their molecular geometry should be considered as well to correlate less negative V^E values for Bn-OH + n-BA. The larger $-C_3H_7$ group in BA makes it less planar and restricts the closer approach of Bn-OH [51], which sterically hinders the interaction of its $-COOH$ group with O-H of Bn-OH and results in less negative V^E values than BnOH + PA. Hence, the observed trend in V^E for the studied systems suggests that the contribution to volume change from cross-association through H-bonding, geometrical effect and steric factor between components of the mixture are equally important.

As can be observed in Figure 2–4, the values of the V^E are more negative with the increase in temperature for all binary mixtures studied. With an increase in the temperature, kinetic energy increases and the interactions between the like molecules of the pure components might be decreased more than that of between unlike component molecules. Consequently, volume contraction increases leading to more negative V^E values. The more negative V^E data with an increase in temperature could also be understood as the enlargement of interstices and thereby more favourable interstitial accommodation between carboxylic acid and benzyl alcohol molecules. This leads to an increased contraction in volume resulting in more negative V^E values.

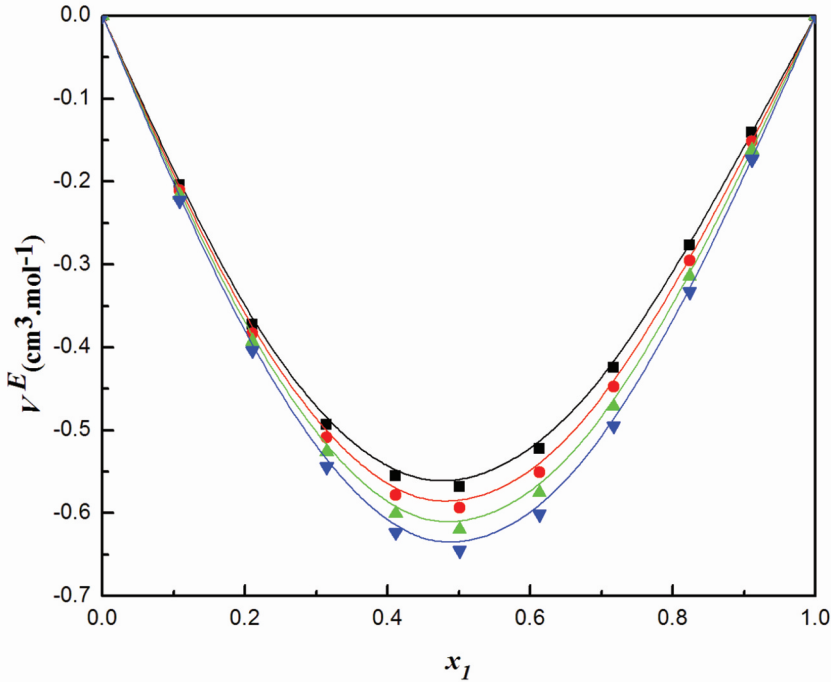


Figure 4. Plot of Excess volumes (V^E) vs. mole fraction (x_1) for Bn-OH (1) + n-BA (2) binary system at $T = 298.15$ K (■), 303.15 K (●), 308.15 K (▲) and 313.15 K (▼).

3.2. Excess isentropic compressibilities (κ_s^E)

The speeds of sound (u) measurements and evaluation of excess isentropic compressibilities (κ_s^E) provide useful insights into the molecular compactness and intermolecular interactions between the components of the mixed solutions. The sign and magnitude of excess isentropic compressibilities (κ_s^E) are reliant on the nature and extent of the intermolecular forces which in turn depend on the size and molecular geometry of the component molecules of the binary solutions. The speeds of sound (u) for the binary systems of Bn-OH with (C_2 - C_4) carboxylic acids over the entire range of concentration at $T = (298.15$ to $313.15)$ K are incorporated in Table 4. It is clear that values of u increase with an increase in mole fraction of Bn-OH and decrease with an increase in temperature from 298.15 to 313.15 K.

The isentropic compressibilities (κ_s) are calculated from density (ρ) and speed of sound (u) data by using the Laplace-Newton's equation:

$$\kappa_s = \frac{1}{u^2 \rho} \quad (2)$$

The excess isentropic compressibilities (κ_s^E) are computed for the mixtures containing Bn-OH and (C_2 - C_4) carboxylic acids by using the relation:

$$\kappa_s^E = \kappa_s - \kappa_s^{id} \quad (3)$$

where, κ_s^{id} represents the ideal isentropic compressibility.

The ideal isentropic compressibilities (κ_s^{id}) were evaluated from the expression suggested by Benson and Kiyohara [52]:



Table 4. Mole fraction of Bn-OH (x_1), speeds of sound (u ($\text{m}\cdot\text{s}^{-1}$), isentropic compressibilities (κ_s ($\text{T}\cdot\text{Pa}^{-1}$)) for Bn-OH + AA/PA/n-BA mixtures at $298.15 \leq T/K \leq 313.15$ and 0.1 MPa pressure.

x_1	u ($\text{m}\cdot\text{s}^{-1}$)	κ_s ($\text{T}\cdot\text{Pa}^{-1}$)	κ_s^E ($\text{T}\cdot\text{Pa}^{-1}$)	x_1	u ($\text{m}\cdot\text{s}^{-1}$)	κ_s ($\text{T}\cdot\text{Pa}^{-1}$)	κ_s^E ($\text{T}\cdot\text{Pa}^{-1}$)
Bn-OH (1) + AA (2)							
T/K = 298.15							
0.0000	1134.2	744.7	0.0	0.0000	1117.4	771.4	0.0
0.1283	1204.5	659.2	-18.4	0.1283	1188.5	680.5	-20.5
0.2455	1265.6	596.7	-28.8	0.2455	1249.4	615.2	-31.2
0.3750	1327.9	542.0	-34.0	0.3750	1311.3	558.4	-36.0
0.4435	1357.2	519.0	-33.6	0.4435	1340.6	534.2	-35.7
0.5293	1391.8	493.8	-32.0	0.5293	1375.1	507.9	-33.7
0.6243	1425.5	471.0	-27.7	0.6243	1408.9	484.2	-29.1
0.7300	1458.1	450.6	-20.9	0.7300	1441.7	462.7	-21.9
0.8329	1485.6	434.5	-13.0	0.8329	1469.5	445.7	-13.6
0.9132	1505.1	423.6	-6.5	0.9132	1489.3	434.3	-6.9
1.0000	1525.2	412.8	0.0	1.0000	1509.6	423.0	0.0
T/K = 308.15							
0.0000	1100.6	799.4	0.0	0.0000	1083.4	829.5	0.0
0.1283	1172.4	702.8	-22.6	0.1283	1156.2	726.4	-25.2
0.2455	1233.3	634.4	-33.7	0.2455	1217.3	654.2	-37.0
0.3750	1294.6	575.4	-38.1	0.3750	1277.9	593.2	-40.6
0.4435	1324.1	550.1	-37.7	0.4435	1307.6	566.5	-40.2
0.5293	1358.4	522.8	-35.4	0.5293	1341.1	538.6	-37.0
0.6243	1391.9	498.1	-30.3	0.6243	1374.8	512.6	-31.5
0.7300	1425.2	475.4	-22.9	0.7300	1408.5	488.6	-23.9
0.8329	1453.4	457.4	-14.4	0.8329	1437.4	469.5	-15.2
0.9132	1473.6	445.3	-7.5	0.9132	1457.9	456.7	-8.0
1.0000	1493.7	433.7	0.0	1.0000	1478.1	444.6	0.0
Bn-OH (1) + PA (2)							
T/K = 298.15							
0.0000	1146.5	769.9	0.0	0.0000	1127.4	800.5	0.0
0.1052	1199.6	695.5	-26.8	0.1052	1181.5	720.7	-29.5
0.2023	1244.6	640.6	-40.3	0.2023	1227.2	662.1	-44.3
0.3067	1289.6	592.1	-46.8	0.3067	1272.4	611.0	-50.9
0.3999	1326.9	556.1	-47.3	0.3999	1310.1	573.0	-51.5
0.4587	1349.4	536.1	-45.9	0.4587	1332.6	552.0	-49.8
0.5620	1387.8	504.5	-41.4	0.5620	1371.1	519.0	-44.6
0.6612	1422.8	478.3	-34.8	0.6612	1406.5	491.4	-37.6
0.7790	1462.8	451.0	-25.3	0.7790	1446.8	462.8	-27.3
0.9056	1501.6	426.7	-12.4	0.9056	1485.9	437.4	-13.3
1.0000	1525.2	412.8	0.0	1.0000	1509.6	423.0	0.0
T/K = 308.15							

(Continued)



Table 4. (Continued).

0.0000	1108.6	832.4	0.0	0.0000 1089.8	866.2	0.0
0.1052	1163.4	747.1	-32.1	0.1052 1145.3	775.0	-34.9
0.2023	1209.8	684.7	-48.3	0.2023 1192.3	708.4	-52.6
0.3067	1255.2	630.8	-55.2	0.3067 1238.1	651.5	-59.9
0.3999	1293.2	590.7	-55.7	0.3999 1276.4	609.1	-60.5
0.4587	1315.8	568.7	-53.8	0.4587 1299.0	586.1	-58.2
0.5620	1354.4	534.2	-48.1	0.5620 1337.7	549.9	-51.7
0.6612	1390.2	505.1	-40.5	0.6612 1373.7	519.4	-43.5
0.7790	1430.7	475.1	-29.4	0.7790 1414.7	487.9	-31.6
0.9056	1470.2	448.5	-14.5	0.9056 1454.5	460.0	-15.5
1.0000	1493.7	433.7	0.0	1.0000 1478.1	444.6	0.0
Bn-OH (1) + n-BA (2)						
T/K = 298.15						
0.0000	1176.7	758.0	0.0	0.0000 1158.1	786.6	0.0
0.1083	1215.6	700.9	-18.2	0.1083 1197.8	725.5	-20.0
0.2101	1252.3	652.7	-30.0	0.2101 1234.9	674.4	-32.7
0.3145	1289.8	608.4	-37.2	0.3145 1272.4	628.0	-40.1
0.4116	1324.4	571.6	-40.0	0.4116 1307.0	589.4	-42.9
0.5010	1355.5	541.3	-39.2	0.5010 1338.5	557.4	-42.1
0.6128	1394.4	506.8	-35.2	0.6128 1377.2	521.7	-37.4
0.7171	1430.2	478.1	-28.6	0.7171 1413.1	491.7	-30.2
0.8238	1466.4	451.6	-19.4	0.8238 1449.8	463.7	-20.4
0.9110	1495.3	431.9	-10.1	0.9110 1479.2	443.0	-10.7
1.0000	1525.2	412.8	0.0	1.0000 1509.6	423.0	0.0
T/K = 308.15						
0.0000	1139.4	816.9	0.0	0.0000 1121.1	848.3	0.0
0.1083	1179.9	751.4	-22.1	0.1083 1162.0	778.6	-24.0
0.2101	1217.4	697.3	-35.8	0.2101 1199.7	721.5	-38.4
0.3145	1254.8	648.8	-43.3	0.3145 1237.4	670.2	-46.5
0.4116	1289.5	608.2	-46.0	0.4116 1272.1	627.8	-49.1
0.5010	1321.2	574.5	-45.2	0.5010 1304.0	592.3	-48.2
0.6128	1360.0	537.1	-39.9	0.6128 1342.9	553.2	-42.4
0.7171	1396.1	505.7	-32.1	0.7171 1379.3	520.2	-34.1
0.8238	1433.2	476.4	-21.7	0.8238 1416.6	489.4	-23.0
0.9110	1463.3	454.4	-11.6	0.9110 1447.2	466.3	-12.3
1.0000	1493.7	433.7	0.0	1.0000 1478.1	444.6	0.0

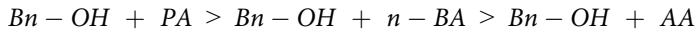
The standard uncertainties are $u(x) = 5 \times 10^{-5}$, $u(u) = 0.5 \text{ m.s}^{-1}$, and $u(T) = 0.01 \text{ K}$

$$\kappa_s^{id} = \sum_{i=1}^2 \phi_i \left[\kappa_{s,i} + \frac{TV_i(\alpha_i^2)}{C_{p,i}} \right] - \left\{ T \left(\sum_{i=1}^2 x_i V_i \right) \left(\sum_{i=1}^2 \phi_i \alpha_i \right)^2 / \sum_{i=1}^2 x_i C_{p,i} \right\} \quad (4)$$

The ϕ_i , V_i , x_i , $\kappa_{s,i}$, α_i and $C_{p,i}$ represents the volume fraction, molar volume, mole fraction, isentropic compressibility, thermal expansion coefficient, and molar heat capacity of i^{th} component respectively. The $C_{p,i}$ values for the pure liquids are collected from the literature [12,15,40] and α_i values for the pure components are calculated from the experimental density (ρ) data according to the relation:

$$\alpha_i = \left(\frac{1}{V} \right) \left(\frac{\partial V}{\partial T} \right)_p = - \left(\frac{1}{\rho} \right) \left(\frac{\partial \rho}{\partial T} \right)_p = - \left(\frac{\partial \ln \rho}{\partial T} \right)_p \quad (5)$$

The experimental κ_s and κ_s^E values for the binary systems over the complete range of concentration at $T = (298.15 \text{ to } 313.15) \text{ K}$ are included in Table 4. The variation of κ_s^E as a function of x_1 for the investigated binary series is plotted in Figure 5–7. An examination of curves in Figure 5–7 reveals that κ_s^E data are negative from $x_1 = 0.1$ to 0.9 at $298.15 \text{ K} \leq T \leq 313.15 \text{ K}$ for the solutions of Bn-OH with (C_2 - C_4) carboxylic acids. The trend in κ_s^E correlates with that of V^E for the investigated systems at four different temperatures. The negative κ_s^E data suggests that the studied binary mixtures might be less compressible than the corresponding ideal mixtures. This could be attributed to a favourable closer approach and stronger intermolecular interaction between the unlike components present in the mixed-species leading to a more compact structure. The negative κ_s^E values at a fixed temperature for the binary solutions fall in the following order:



The negative κ_s^E values could be attributed to two factors namely (i) formation of cross H-bonding interactions between Bn-OH and (C_2 - C_4) carboxylic acids and (ii) interstitial accommodation of carboxylic acids in hydrogen-bonded benzyl alcohol aggregates due to the considerable difference in their molecular sizes and molar volumes. The above order of κ_s^E data for the studied binary mixtures is a consequence of the balance between the factors (i) and (ii) that occurs due to the mixing of pure liquids. Hence, the trend in κ_s^E could be interpreted as the suitable combination of cross H-bond interactions and geometrical effect between unlike component molecules of the mixture. One would expect more negative κ_s^E for Bn-OH + AA mixture due to the largest differences in molar volumes between Bn-OH and AA but the strength of the specific interactions between the unlike components of the mixture are considered to be equally important. The cross H-bonding interactions are relatively weaker between Bn-OH and AA due to the lesser +I-effect of the smaller $-CH_3$ group in AA, resulting in less negative κ_s^E values for Bn-OH + AA.

The negative κ_s^E values increase with an increase in temperature because the decrease in intermolecular interactions between like molecules is more compared to those between dissimilar molecules [53]. In addition, an increase in temperature results in the enlargement of interstices, which in turn leads to more efficient packing between Bn-OH and (C_2 - C_4) carboxylic acids. Hence, the binary solutions become more rigid and difficult to compress leading to more negative κ_s^E values.

3.3. Correlation of derived properties

The experimental V^E and κ_s^E of Bn-OH + (C_2 - C_4) carboxylic acids at $298.15 \text{ K} \leq T \leq 313.15 \text{ K}$, are correlated with mole fraction, using the Redlich-Kister (R-K) polynomial equation [54]:

$$Y^E = x_1 x_2 \sum_{i=0}^n A_i (2x_1 - 1)^i \quad (6)$$

where $Y^E = V^E$ or κ_s^E ; x_1 is the mole fraction of pure benzyl alcohol.

The adjustable parameters A_0 , A_1 , and A_2 of each excess function are computed by the procedure of least-squares. The correlation parameters are included in Table 5 along with the standard deviations $\sigma(Y^E)$. These deviations for the investigated excess properties are determined by using the expression:

$$\sigma(Y^E) = \left[\frac{\sum (Y_{exp}^E - Y_{cal}^E)^2}{(m - n)} \right]^{\frac{1}{2}} \quad (7)$$

where m is the number of experimental measurements and n is the number of correlation parameters; Y_{cal}^E and Y_{exp}^E are the calculated and experimental values of excess functions respectively.

The low $\sigma(Y^E)$ values between the calculated and experimental values of excess parameters obtained at $298.15 \text{ K} \leq T \leq 313.15 \text{ K}$ for Bn-OH + CA indicate that the experimental V^E and κ_s^E data is consistent.

3.4. Excess partial molar volumes

The partial molar properties have often been used to get insights into the solute-solvent interactions that govern the binary mixture behaviour over the entire range of composition. The partial molar volumes of Bn-OH (\bar{V}_1) and (C₂-C₄) carboxylic acids (\bar{V}_2), in these mixtures over the complete range of composition were computed by using the following Equation [15, 55]:

$$\bar{V}_1 = V^E + V_1^0 - x_2 \left(\frac{\partial V^E}{\partial x_2} \right)_{T,P} \quad (8)$$

$$\bar{V}_2 = V^E + V_2^0 + x_1 \left(\frac{\partial V^E}{\partial x_2} \right)_{T,P} \quad (9)$$

where x_1 , V_1^0 and x_2 , V_2^0 represent the mole fractions and molar volumes of Bn-OH and (C₂-C₄) carboxylic acids respectively.

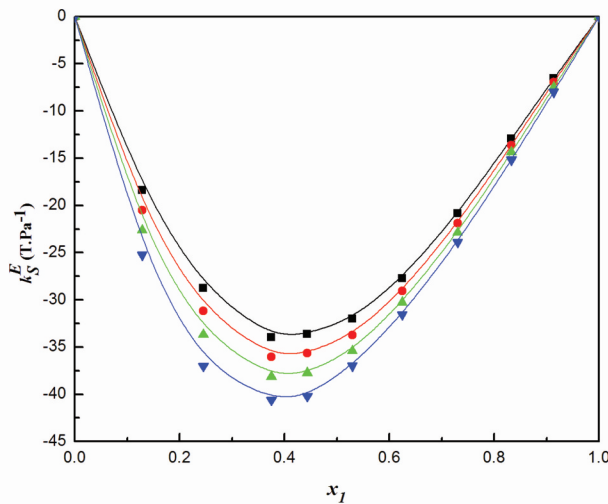


Figure 5. Excess isentropic compressibilities (κ_s^E) for Bn-OH (1) + AA (2) mixture against composition (x_1) at investigated temperatures: 298.15 K (■), 303.15 K (●), 308.15 K (▲) and 313.15 K (▼).

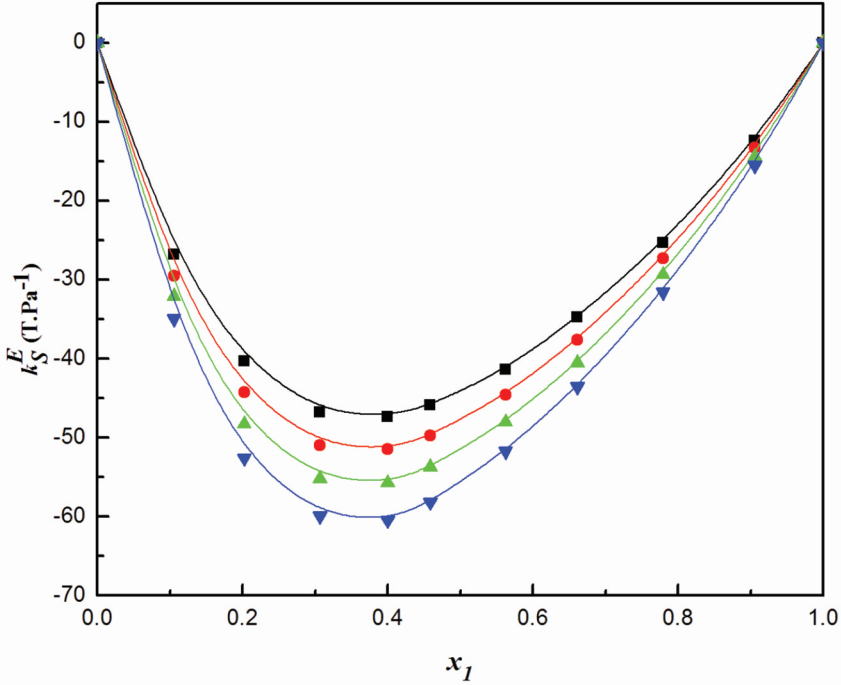


Figure 6. Excess isentropic compressibilities (k_S^E) for Bn-OH (1) + PA (2) mixture against composition (x_1) at investigated temperatures: 298.15 K (■), 303.15 K (●), 308.15 K (▲) and 313.15 K (▼).

The $\left(\frac{\partial V^E}{\partial x_2}\right)$ term in Equation 8 and 9 is calculated by differentiating Equation 6, which leads to the following expressions for \overline{V}_1 and \overline{V}_2 respectively:

$$\overline{V}_1 = V_1^0 + x_2^2 \sum_{i=0}^n A_i (1 - 2x_2)^i + 2(1 - x_2)x_2^2 \sum_{i=0}^n A_i(i)(1 - 2x_2)^{i-1} \quad (10)$$

$$\overline{V}_2 = V_2^0 + (1 - x_2)^2 \sum_{i=0}^n A_i (1 - 2x_2)^i - 2(1 - x_2)x_2^2 \sum_{i=0}^n A_i(i)(1 - 2x_2)^{i-1} \quad (11)$$

To study the changes in the association patterns between components of the binary mixture, the excess partial molar volumes of Bn-OH (\overline{V}_1^E) and (C₂-C₄) carboxylic acids (\overline{V}_2^E), have been computed using the following Equation [56]:

$$\overline{V}_1^E = \overline{V}_1 - V_1^0 \quad (12)$$

$$\overline{V}_2^E = \overline{V}_2 - V_2^0 \quad (13)$$

The partial molar volumes at infinite dilution give some information about the solvent effect on the structure of the solute in the mixed solutions. The partial molar volumes of Bn-OH at infinite dilution in (C₂-C₄) carboxylic acids (\overline{V}_1^∞) and C₂-C₄ carboxylic acids in Bn-OH (\overline{V}_2^∞) have been evaluated with the help of the R-K coefficients by using the following expressions [56,57]:

$$\overline{V}_1^\infty = V_1^0 + \sum_{i=0}^n A_i (-1)^i \quad (14)$$

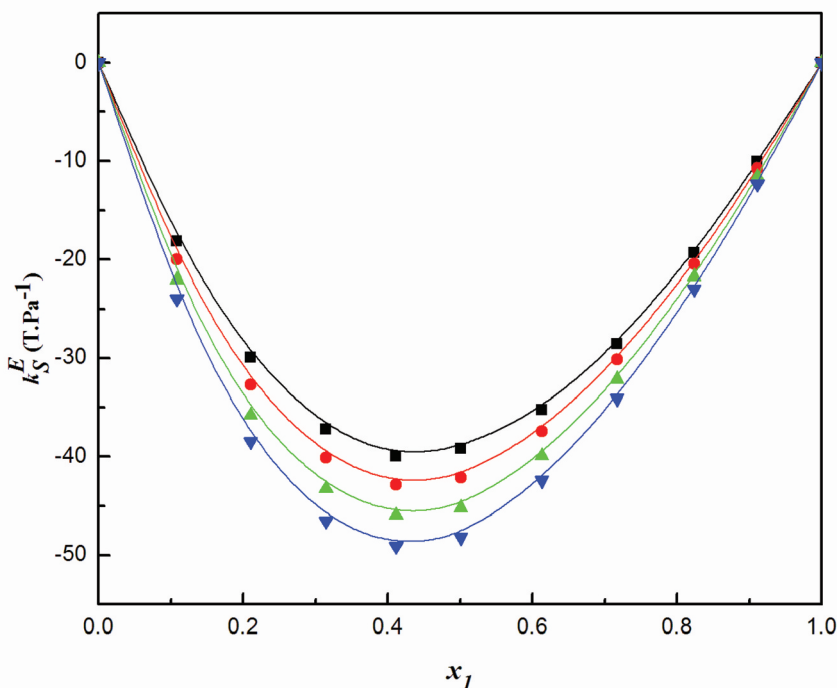


Figure 7. Excess isentropic compressibilities (k_S^E) for Bn-OH (1) + n-BA (2) mixture against composition (x_1) at investigated temperatures: 298.15 K (■), 303.15 K (●), 308.15 K (▲) and 313.15 K (▼).

$$\bar{V}_2^\infty = V_2^0 + \sum_{i=0}^n A_i \quad (15)$$

In addition, the excess partial molar volumes of Bn-OH ($\bar{V}_1^{E,\infty}$) and (C₂-C₄) carboxylic acids ($\bar{V}_2^{E,\infty}$) at infinite dilution are evaluated with the following Eq

$$\bar{V}_1^{E,\infty} = \bar{V}_1^\infty - V_1^0 = \sum_{i=0}^n A_i (-1)^i \quad (16)$$

$$\bar{V}_2^{E,\infty} = \bar{V}_2^\infty - V_2^0 = \sum_{i=0}^n A_i \quad (17)$$

The values of \bar{V}_1 , \bar{V}_2 , \bar{V}_1^E and \bar{V}_2^E of Bn-OH+AA/PA/n-BA are collected in Table S1 in the supplementary material. The variation of \bar{V}_1^E and \bar{V}_2^E values with mole fraction (x_1) for the investigated systems at T = (298.15, 303.15, 308.15 and 313.15) K are presented in Figure 8–10. A kind perusal of Figure 8–10 indicates that \bar{V}_1^E and \bar{V}_2^E values are negative over complete concentration range for Bn-OH+AA/PA/n-BA systems at four investigated temperatures. This suggests that the partial molar volumes (\bar{V}_i) of each component in the binary solution were less than their corresponding pure molar volume (V_i^0).

The overall negative magnitude of \bar{V}_i^E follows the order:

$$\bar{V}_i^E(\text{Bn-OH} + \text{PA}) > \bar{V}_i^E(\text{Bn-OH} + \text{n-BA}) > \bar{V}_i^E(\text{Bn-OH} + \text{AA})$$

The negative \bar{V}_i^E values of each component in the mixture suggest that there is a contraction in volume on mixing Bn-OH + AA/PA/n-BA due to the presence of solute-solvent interactions

Table 5. The Redlich–Kister fitting parameters (A_0 – A_2) and standard deviations $\sigma(Q^F)$ for excess functions obtained for Bn-OH (1) + carboxylic acids (2) at $T/K = 298.15$ to 313.15 and 0.1 MPa.

T(K)	Excess function			Redlich–Kister			Excess function			Redlich–Kister		
	A_0	A_1	A_2	$\sigma(Q^F)$	A_0	A_1	A_2	$\sigma(Q^F)$	A_0	A_1	A_2	$\sigma(Q^F)$
Bn-OH (1) + acetic acid (2)												
298.15	-1.081	0.200	0.057	0.0008	-131.5	51.41	9.540	0.1521	-131.5	51.41	9.540	0.1521
303.15	-1.116	0.204	0.048	0.0008	-138.5	60.41	1.101	0.1341	-138.5	60.41	1.101	0.1341
308.15	-1.152	0.207	0.039	0.0007	-145.4	68.79	-9.059	0.1315	-145.4	68.79	-9.059	0.1315
313.15	-1.187	0.210	0.032	0.0009	-153.0	80.72	-21.85	0.1507	-153.0	80.72	-21.85	0.1507
Bn-OH (1) + propionic acid (2)												
298.15	-2.626	0.573	0.219	0.0012	-177.3	88.07	-59.49	0.1178	-177.3	88.07	-59.49	0.1178
303.15	-2.693	0.562	0.227	0.0015	-192.0	99.15	-68.27	0.1447	-192.0	99.15	-68.27	0.1447
308.15	-2.755	0.552	0.221	0.0014	-207.3	108.6	-76.43	0.1287	-207.3	108.6	-76.43	0.1287
313.15	-2.818	0.540	0.222	0.0013	-223.9	120.0	-84.32	0.1237	-223.9	120.0	-84.32	0.1237
Bn-OH (1) + n-butyric acid (2)												
298.15	-2.279	0.222	0.530	0.0018	-157.7	39.18	0.134	0.1286	-157.7	39.18	0.134	0.1286
303.15	-2.378	0.173	0.537	0.0015	-168.5	46.54	-3.521	0.0939	-168.5	46.54	-3.521	0.0939
308.15	-2.476	0.126	0.541	0.0010	-180.0	53.78	-10.97	0.1289	-180.0	53.78	-10.97	0.1289
313.15	-2.576	0.080	0.547	0.0010	-191.7	60.57	-14.25	0.1291	-191.7	60.57	-14.25	0.1291

between dissimilar molecules. The increase in \overline{V}_1^E data at lower x_1 and decrease in \overline{V}_2^E values at higher x_1 is clear evidence of disruption of the hydrogen-bonded Bn-OH and CA self associates respectively. The observed negative \overline{V}_i^E data indicates of the dominance of cross H-bonding formation between Bn-OH and CA over the structure breaking effect between like molecules. The negative \overline{V}_1^E and \overline{V}_2^E are also equally attributed to the significant geometrical fitting between the component molecules in Bn-OH + AA/PA/n-BA. The reasons for the above observed trend in \overline{V}_i^E and its variation with temperature were similar to those of V^E .

From Table S2 in supplementary material, it is evident that the partial properties at infinite dilution (\overline{V}_1^∞ and \overline{V}_2^∞) are lower than the respective pure molar volumes (V_1^0 and V_2^0) for all the investigated binary systems at each temperature. This emphasises that there is a contraction in volume due to better packing effect on mixing Bn-OH with AA/PA/n-BA. An examination of values in Table S2 also reveals that $\overline{V}_1^{E,\infty}$ and $\overline{V}_2^{E,\infty}$ for Bn-OH and CA respectively are negative at all investigated temperatures. This indicates that at infinite dilution, the intermolecular interactions between dissimilar molecules exceed the structure breaking effect between similar molecules i.e., the cross hydrogen bonding between Bn-OH and CA is not broken in dilute regions. In addition, the negative \overline{V}_1^E and \overline{V}_2^E are also equally attributed to the packing effect in Bn-OH + CA. The more negative $\overline{V}_1^{E,\infty}$ and $\overline{V}_2^{E,\infty}$ values for Bn-OH + PA is attributed to energetically more favoured solute-solvent interactions at infinite dilution. The values of \overline{V}_1^E and \overline{V}_2^E become more negative with the increase in temperature for each system investigated, which indicates a more favourable interstitial accommodation between component molecules due to the enlargement of interstices. These results further support the trends observed in V^E and κ_s^E data for the investigated binary systems.

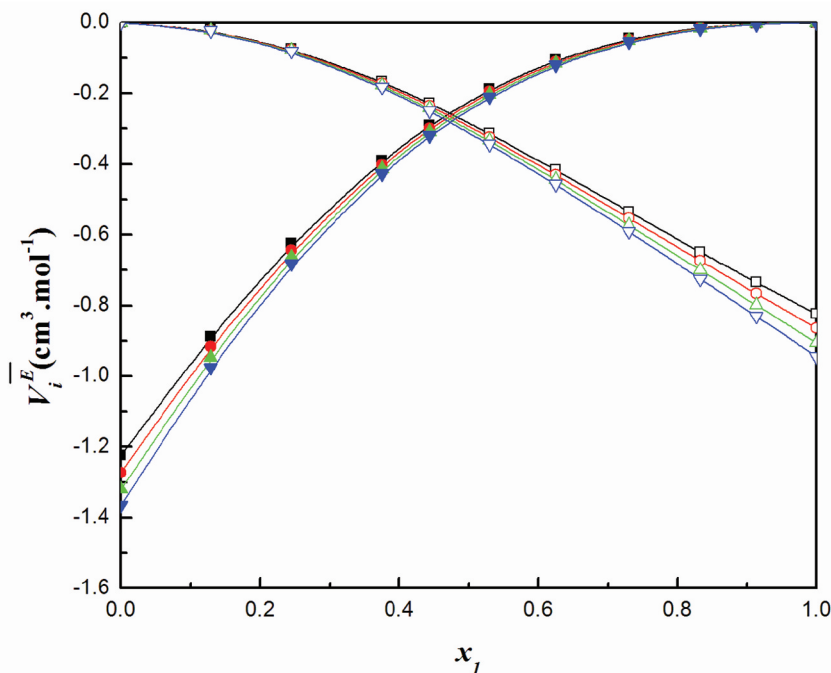


Figure 8. Plot of excess partial molar volumes of Bn-OH in AA (\overline{V}_1^E) and AA in Bn-OH (\overline{V}_2^E) at T = 298.15 K (■ and □), 303.15 K (● and ○), 308.15 K (▲ and △), and 313.15 K (▼ and ▽) respectively.

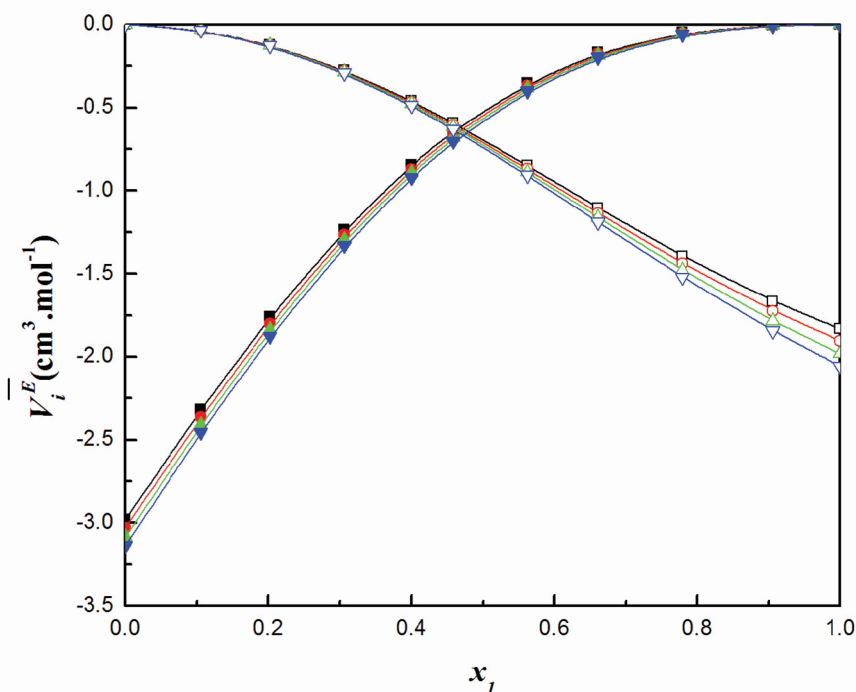


Figure 9. Plot of excess partial molar volumes of Bn-OH in PA (\bar{V}_1^E) and PA in Bn-OH (\bar{V}_2^E) at T = 298.15 K (■ and □), 303.15 K (● and ○), 308.15 K (▲ and △), and 313.15 K (▼ and ▽) respectively.

3.5. ATR-FTIR investigations

Attenuated total reflection Fourier transform infrared (ATR-FTIR) spectroscopic technique is one of the powerful tools used to investigate the nature and extent of intermolecular interactions like hydrogen bonding between components in the mixtures by analysing the position, shape and, shifts of the FT-IR band [58]. In general, the H-bonding results in broadening and shifting of the X-H stretching band (X is highly electronegative than H) to lower frequencies (red shift). The existence of cross H-bonding and its strength in Bn-OH + AA/PA/n-BA could be identified by comparison of shift in the absorption band of hydroxyl group $\nu(\text{-O-H})$ of Bn-OH with the respective bands in their pure states.

In alcohols, the characteristic stretching frequency of free O-H group is observed around $3700\text{--}3650\text{ cm}^{-1}$ and H-bonded $\nu(\text{-O-H})$ shows a broad band around $3550\text{--}32,000\text{ cm}^{-1}$ [59]. The partial ATR-FTIR spectra of pure benzyl alcohol recorded at T = 298.15 K is shown in Figure 11, which shows that $\nu(\text{-O-H})$ absorption band appears at 3317.8 cm^{-1} . This broad -O-H band clearly indicates Bn-OH was self associated through intermolecular H-bonding. The -O-H stretching frequencies of pure AA, PA, and n-BA are in the order of 3018.6 cm^{-1} , 2983.9 cm^{-1} , and 2968.5 cm^{-1} respectively. ATR-FTIR spectra of equimolar binary solutions of Bn-OH with AA/PA/n-BA are recorded and the corresponding $\nu(\text{O-H})$ absorption bands of Bn-OH at $x_1 = 0.5$ are presented in Table 6 and Figure 11. The $\nu(\text{O-H})$ bands for the equimolar mixtures of Bn-OH + AA, Bn-OH + PA and Bn-OH + n-BA are found to be 3292.5 cm^{-1} , 3232.7 cm^{-1} and 3273.2 cm^{-1} respectively. The red shift ($\Delta\nu$) of -O-H stretching frequency of Bn-OH in AA/PA/n-BA is calculated and incorporated in Table 6. The red shift ($\Delta\nu$) of $\nu(\text{O-H})$ peak position of Bn-OH in equimolar mixtures of carboxylic acids fall in the order:

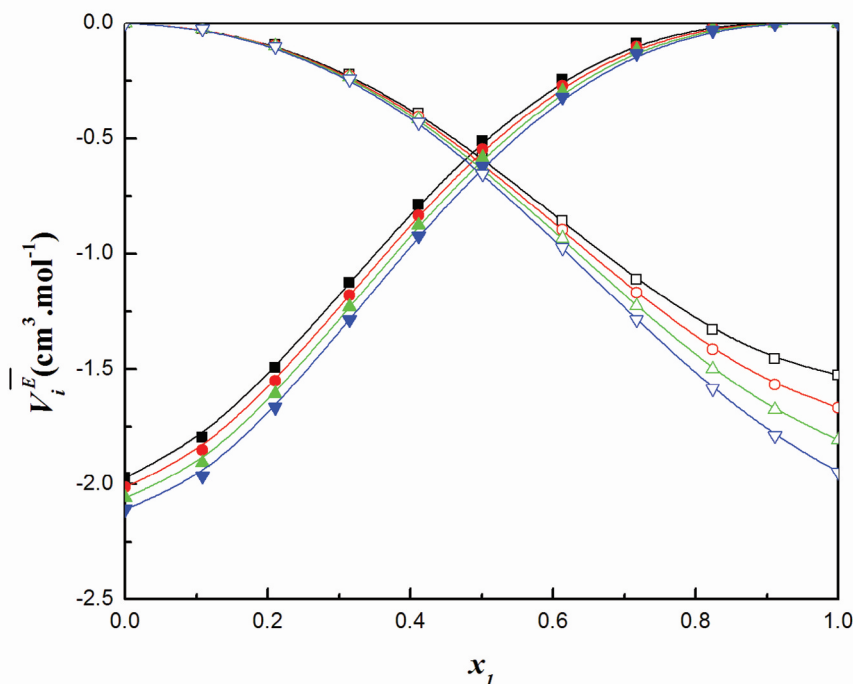


Figure 10. Plot of excess partial molar volumes of Bn-OH in n-BA (\bar{V}_1^E) and n-BA in Bn-OH (\bar{V}_2^E) at T = 298.15 K (■ and □), 303.15 K (● and ○), 308.15 K (▲ and △), and 313.15 K (▼ and ▽) respectively.

Bn-OH + PA (-79.1 cm^{-3}) > Bn-OH + n-BA (-38.6 cm^{-3}) > Bn-OH + AA (-19.3 cm^{-3})

The red shift of $\nu(\text{O-H})$ absorption band appeared in the range of $3292.5 - 3273.2 \text{ cm}^{-1}$ for the three binary mixtures studied shows the existence of cross H-bonding between the hydroxyl group of Bn-OH and ($\text{C}_2\text{-C}_4$) carboxylic acids. It is well-known that the degree of red shift of $\nu(\text{O-H})$ band is a direct measure of the strength of intermolecular H-bond [58,59]. The larger red shift of $\nu(\text{O-H})$ absorption peak in Bn-OH + PA suggests that a stronger cross H-bonding exists between Bn-OH and PA system compared to those of Bn-OH + n-BA and Bn-OH + AA systems. Thus, the excess thermodynamic properties studied in the present investigation are supported by ATR-FTIR spectral analysis through the elucidation of cross H-bonding between Bn-OH and AA/PA/n-BA systems.

4. Conclusion

In this study, densities (ρ) and speeds of sound (u) have been measured for binary solutions of Bn-OH with ($\text{C}_2\text{-C}_4$) carboxylic acids for the whole concentration range at $298.15 \text{ K} \leq T \leq 313.15 \text{ K}$ under atmospheric pressure. The various excess properties (V^E , κ_s^E , \bar{V}_i^E , and $\bar{V}_i^{E,\infty}$) are evaluated from the experimental ρ and u results. The sign of the studied excess functions was found to be negative for the binary mixtures over the complete range of mole fraction. It is observed that (i) formation of cross hydrogen bonding between Bn-OH and ($\text{C}_2\text{-C}_4$) carboxylic acids (ii) packing effects between components of the mixture, and (iii) steric hindrance effect equally contributes to the magnitude of the evaluated excess parameters. At a fixed composition, the non-ideality of Bn-OH + AA/PA/n-BA systems increases with an increase in the temperature. In addition, the experimental excess volumes

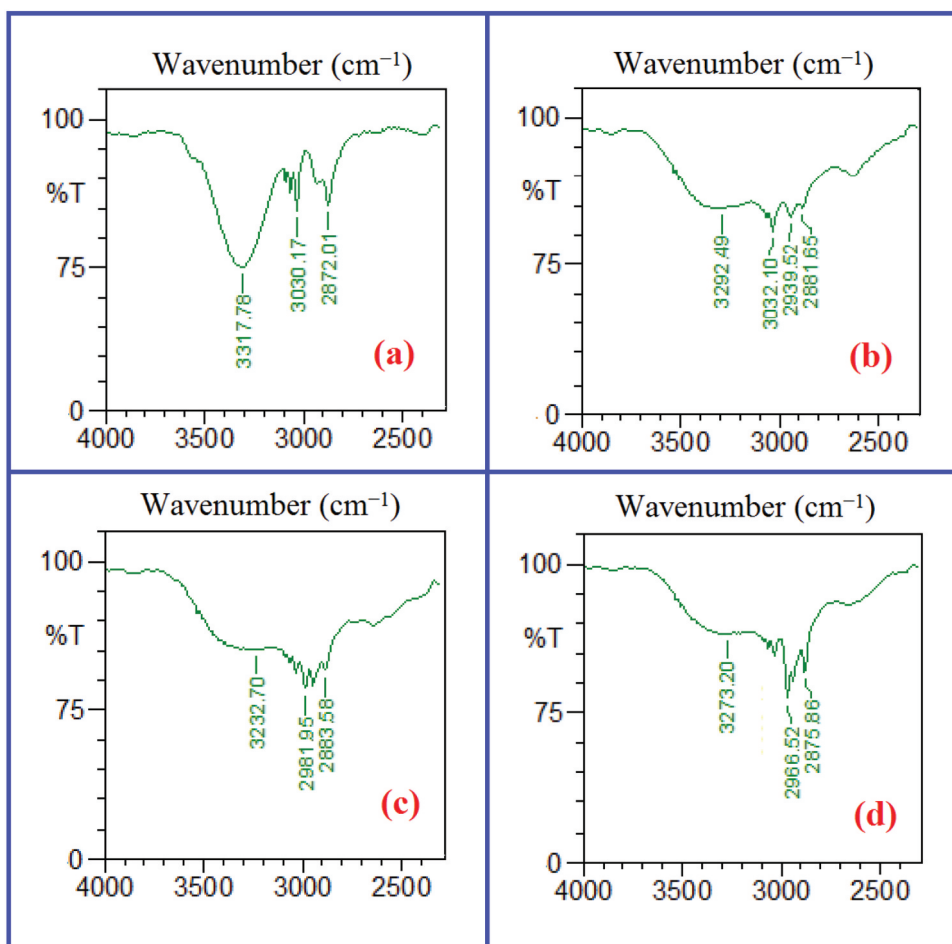


Figure 11. The partial ATR-FTIR spectra of (a) pure Bn-OH in the $\nu(\text{O-H})$ region; -O-H stretching frequencies of Bn-OH at $x_1 = 0.5$ in the binary systems of (b) Bn-OH + AA; (c) Bn-OH + PA; and (d) Bn-OH + n-BA.

(V^E), excess isentropic compressibilities (κ_s^E) have been correlated with Redlich-Kister equation. The thermodynamic conclusions are found to be in good agreement with the ATR-FTIR spectral studies of the binary systems.

Table 6. Experimental ATR-FTIR vibrational frequencies, ν_{max} (cm^{-1}) of the pure and equimolar binary mixtures of Bn-OH with (C_2 - C_4) carboxylic acids at ambient temperature.

System	Vibrational band	Experimental vibrational frequencies ν_{max} (cm^{-1})	Shift of vibrational frequencies $\Delta\nu_{max}$ (cm^{-1})
Pure Bn-OH	-O-H (a)	3317.8	-
Pure EA	-O-H (b)	3018.6	-
Pure PA	-O-H (c)	2983.9	-
Pure n-BA	-O-H (d)	2968.5	-
Bn-OH + AA	-O-H...O-H (e)	3292.5	-25.3 (e-a)
Bn-OH + PA	-O-H...O-H (f)	3232.7	-85.1 (f-a)
Bn-OH + n-BA	-O-H...O-H (g)	3273.2	-44.6 (g-a)

Acknowledgements

The authors express sincere thanks to Prof. C. Suresh Reddy, Department of Chemistry, S.V. University, Tirupati for the assistance in ATR-FTIR studies.

Disclosure statement

No potential conflict of interest was reported by the authors.

ORCID

P. Bhanuprakash  <http://orcid.org/0000-0002-8885-4689>

Ramesh L. Gardas  <http://orcid.org/0000-0002-6185-5825>

References

- [1] Malek NI, Ijardar SP, Master ZR, et al. Temperature dependence of densities, speeds of sound, and derived properties of cyclohexylamine + cyclohexane or benzene in the temperature range 293.15–323.15 K. *Thermochim Acta*. 2012;547:106–119.
- [2] Peralta RD, Infente R, Cortze G, et al. Densities and excess volumes of benzene with ethyl acrylate, butyl acrylate, methyl methacrylate, and styrene at 298.15 K. *Thermochim Acta*. 2003;398:39–46.
- [3] Reddy PM, Sivakumar K, Venkatesu P. Densities and ultrasonic studies for binary mixtures of tetrahydrofuran with chlorobenzenes, chlorotoluenes and nitrotoluenes at 298.15. *Fluid Phase Equilib*. 2011;310:74–81.
- [4] Marianoa A, Mussari L, Orozc M, et al. Volumetric and transport properties of the ternary mixtures of toluene (1) + benzene (2) + butyl acetate (3) at different temperatures. *Phys Chem Liq*. 2015;53:587–598.
- [5] Parveen S, Singh S, Shukla D, et al. Study of molecular interactions in binary mixtures of aniline with carboxylic acids at 293.15 K, 303.15 K and 313.15 K. *J Solution Chem*. 2012;41:156–172.
- [6] Letcher TM, Redhi GG. Thermodynamic excess properties for binary mixtures of (benzonitrile + a carboxylic acid) at T = 298.15 K. *Fluid Phase Equilib*. 2002;198:257–266.
- [7] Alavianmehr MM, Hemmati N, Ghodrati H. Excess molar volumes, excess thermal expansion coefficients and isentropic compressibility deviations for binary mixtures of benzyl alcohol + (1-butanol, 2-butanol, 2-methyl-1-butanol and *tert*-butanol) at T = (298.15–328.15) K and ambient pressure. *Phys Chem Liq*. 2017;55:85–99.
- [8] Gardas RL, Freire MG, Carvalho PJ, et al. High-pressure densities and derived thermodynamic properties of imidazolium-based ionic liquids. *J Chem Eng Data*. 2007;52:80–88.
- [9] Takamuku T, Kyoshoin Y, Noguchi H, et al. Liquid structure of acetic acid–water and trifluoroacetic acid –water mixtures studied by large-angle x-ray scattering and NMR. *J Phys Chem B*. 2007;111:9270–9280.
- [10] Chen J, Brooks CL, Scheraga HA. Revisiting the carboxylic acid dimers in aqueous solution: interplay of hydrogen bonding, hydrophobic interactions, and entropy. *J Phys Chem B*. 2008;112:242–249.
- [11] Clifford SL, Ramjugernath D, Raal JD. Subatmospheric vapor pressure curves for propionic acid, butyric acid, isobutyric acid, valeric acid, isovaleric acid, hexanoic acid, and heptanoic acid. *J Chem Eng Data*. 2004;49:1189–1192.
- [12] Bhanuprakash P, Narasimha Rao C, Sivakumar K. Evaluation of molecular interactions by volumetric and acoustic studies in binary mixtures of the ionic liquid [EMIM][MeSO₄] with ethanoic and propanoic acid at different temperatures. *J Mol Liq*. 2016;219:79–87.
- [13] Bahadur I, Deenadayalu N, Naidoo P, et al. Density, speed of sound, and refractive index measurements for the binary systems (butanoic acid + propanoic acid, or 2-methyl-propanoic acid) at T = (293.15 to 313.15) K. *J Chem Thermodyn*. 2013;57:203–211.
- [14] Ali A, Tariq M. Thermodynamic and transport behaviour of binary liquid mixtures of benzyl alcohol with monocyclic aromatics at 303.15 K. *J Mol Liq*. 2006;128:50–55.
- [15] Bhanuprakash P, Jyothi NVV, Narasimharao C, et al. Elucidation of molecular interactions in the mixtures of benzylalcohol with (C₂–C₄) alkylacetates through volumetric, ultrasonic, theoretical and ATR-FTIR spectroscopic studies at T = (298.15, 303.15, 308.15 and 313.15) K. *J Mol Liq*. 2017;234:49–63.
- [16] Chen KD, Lin YF, Tu CH. Densities, viscosities, refractive indexes, and surface tensions for mixtures of ethanol, benzyl acetate, and benzyl alcohol. *J Chem Eng Data*. 2012;57:1118–1127.
- [17] Martindale W. *The Extra Pharmacopoeia*. 33rd ed. London: Pharmaceutical Press; 2002.
- [18] O'Neil MJ, ed. *The merck index—an encyclopedia of chemicals, drugs and biologicals*. 13th ed. Whitehouse Station. NJ: Merck and Co., Inc; 2001.

- [19] Hong YK, Hong WH, Han DH. Application of reactive extraction to recovery of carboxylic acids. *Biotechnol Bioprocess Eng.* 2001;6:386–394.
- [20] Neyband RS, Yousefi A, Zarei H. Experimental and computational thermodynamic properties of (benzyl alcohol+ alkanols) mixtures. *J Chem Eng Data.* 2015;60:2291–2300.
- [21] Venkatramana L, Sreenivasulu K, Sivakumar K, et al. Thermodynamic properties of binary mixtures containing 1-alkanols. *J Therm Anal Calorim.* 2014;115:1829–1834.
- [22] Venkatramana L, Sivakumar K, Gardas RL, et al. Effect of chain length of alcohol on thermodynamic properties of their binary mixtures with benzylalcohol. *Thermochim Acta.* 2014;581:123–132.
- [23] Yeh CT, Tu CH. Densities, viscosities, refractive indexes, and surface tensions for binary mixtures of 2-propanol+ benzyl alcohol,+ 2-phenylethanol and benzyl alcohol + 2-Phenylethanol at T = (298.15, 308.15, and 318.15) K. *J Chem Eng Data.* 2007;52:1760–1767.
- [24] Raveendra M, Narasimharao C, Venkatramana L, et al. Effect of chain length of alcohol on thermodynamic properties of their binary mixtures with benzylalcohol. *J Chem Thermodyn.* 2016;92:97–107.
- [25] Raveendra M, Chandrasekhar M, Narasimharao C, et al. Elucidation of hydrogen bonding formation by a computational, FT-IR spectroscopic and theoretical study between benzyl alcohol and isomeric cresols. *RSC Adv.* 2016;6:27335–27348.
- [26] Comelli F, Ottani S. Excess enthalpies of binary mixtures containing poly (propylene glycols) + benzyl alcohol, or + m-cresol, or + anisole at 308.15 K and at atmospheric pressure. *Thermochim Acta.* 2005;430:123–128.
- [27] Kumar RV, Rao AA, Rao MV, et al. Excess molar enthalpies of chloroalkanes or chloroalkenes+ benzyl alcohol at 298.15 K. *J Chem Eng Data.* 1995;40:99–101.
- [28] Venkatramana L, Sivakumar K, Govinda V, et al. Study on solution properties of some industrially important solvents with an aromatic alcohol. *J Mol Liq.* 2013;186:163–170.
- [29] Venkatramana L, Gardas RL, Sivakumar K, et al. Thermodynamics of binary mixtures: the effect of substituents in aromatics on their excess properties with benzylalcohol. *Fluid Phase Equilib.* 2014;367:7–21.
- [30] Ali A, Nain AK, Chand D, et al. Volumetric and viscometric studies of molecular interactions in binary N, N-dimethylacetamide + benzyl alcohol mixtures at different temperatures. *S Afr J Chem.* 2005;58:98–104.
- [31] Nikam PS, Kharat SJ. Densities and viscosities of binary mixtures of N, N-dimethylformamide with benzyl alcohol and acetophenone at (298.15, 303.15, 308.15, and 313.15) K. *J Chem Eng Data.* 2003;48:1291–1295.
- [32] Francesconi R, Bigi A, Rubini K, et al. Excess enthalpies, heat capacities, densities, viscosities and refractive indices of dimethyl sulfoxide + three aryl alcohols at 308.15 K and atmospheric pressure. *J Chem Eng Data.* 2005;50:1932–1937.
- [33] Nayak JN, Aralaguppi MI, Aminabhavi TM. Density, viscosity, refractive index, and speed of sound in the binary mixtures of ethyl chloroacetate + cyclohexanone, + chlorobenzene, + bromobenzene, or + benzyl Alcohol at (298.15, 303.15, and 308.15) K. *J Chem Eng Data.* 2003;48:628–631.
- [34] Rafiee HR, Sadeghi S. The study of excess molar volumes and related properties for binary mixtures containing benzyl alcohol and 1,3-dichloro-2-propanol with vinyl acetate, ethyl acetate and t-butyl acetate at T = 293.15 to 313.15 K and P = 0.087 MPa. *Thermochim Acta.* 2016;633:149–160.
- [35] Alavianmehr MM, Shahsavari S, Ghodrati H, et al. Measurement and modeling of volumetric properties and speeds of sound of several mixtures of alcohol liquids containing butanediol. *J Chem Eng Data.* 2015;60:1956–1967.
- [36] Singh S, Bahadur I, Redhi GG, et al. Density and speed of sound of 1-ethyl-3-methylimidazolium ethyl sulphate with acetic or propionic acid at different temperatures. *J Mol Liq.* 2014;199:518–523.
- [37] Vong WT, Tsai FN. Densities, molar volumes, thermal expansion coefficients, and isothermal compressibilities of organic acids from 293.15 K to 323.15 K and at pressures up to 25 MPa. *J Chem Eng Data.* 1997;42:1116–1120.
- [38] Mukesh B, Gowrisankar M, Krishna TS, et al. Studies on the importance of thermodynamic and transport properties of liquid mixtures at various temperatures. *J Therm Anal Calorim.* 2018;132:1167–1181.
- [39] Bahadur I, Naidoo P, Singh S, et al. Effect of temperature on density, sound velocity, refractive index and their derived properties for the binary systems (heptanoic acid + propanoic or butanoic acids). *J Chem Thermodyn.* 2014;78:7–15.
- [40] Bahadur I, Singh S, Deenadayalu N, et al. Influence of alkyl group and temperature on thermophysical properties of carboxylic acid and their binary mixtures. *Thermochim Acta.* 2014;590:151–159.
- [41] Fortin TJ, Laesecke A, Freund M, et al. Advanced calibration, adjustment, and operation of a density and sound speed analyzer. *J Chem Thermodyn.* 2013;57:276–285.
- [42] Motin MA, Kabir MH, Huque EM. Densities and excess molar volumes of formic acid, acetic acid and propionic acid in pure water and in water + Surf Excel solutions at different temperatures. *Phys Chem Liq.* 2005;43:277–288.
- [43] Kumari A, Sandeepa K, Kumar TP, et al. Solubility, thermodynamic properties, and derived excess properties of benzoic acid in (acetic acid + water) and (acetic acid + toluene) binary mixtures. *J Chem Eng Data.* 2016;61:67–77.

- [44] Gonzalez B, Dominguez A, Tojo J. Dynamic viscosities, densities, and speed of sound and derived properties of the binary systems acetic acid with water, methanol, ethanol, ethyl acetate and methyl Acetate at $T = (293.15, 298.15, \text{ and } 303.15) \text{ K}$ at atmospheric pressure. *J Chem Eng Data*. 2004;49:1590–1596.
- [45] Singh S, Bahadur I, Redhi GG, et al. Influence of the alkyl group on thermophysical properties of carboxylic acids in 1-butyl-3-methylimidazolium thiocyanate ionic liquid at various temperatures. *J Chem Thermodyn*. 2015;89:104–111.
- [46] Tummanapelli AK, Vasudevan S. Dissociation constants of weak acids from ab initio molecular dynamics using metadynamics: influence of the inductive effect and hydrogen bonding on pK_a Values. *J Phys Chem B*. 2014;118(47):13651–13657.
- [47] Lark BS, Singh S, Aggarwal SK, et al. volumes of n-butyric acid + various polar and nonpolar solvents. *J Chem Eng Data*. 1985;30:467–469.
- [48] Letcher TM, Redhi GG. Excess enthalpies and volumes for mixtures of (acetonitrile + a carboxylic acid) at 298.15 K. *J Chem Eng Data*. 2000;45:57–60.
- [49] Ahluwalia R, Gupta R, Vashisht JL, et al. Thermophysical properties of binary liquid systems of ethanoic acid, propanoic acid, and butanoic acid with benzene or acetophenone. *ISRN Phys Chem*. 2013;2013:1–13. ArticleID 612837.
- [50] Lark BS, Banipal TS. Excess volumes and excess enthalpies of acetic and its methyl-substituted acids + acetonitrile. *Can J Chem*. 1985;63:3269–3275.
- [51] Dalai B, Dash SK, Singh SK. Viscometric, volumetric and acoustic properties of binary mixtures of a nuclear extractant with monocarboxylic acids (C_1 - C_3) at 303.15 K. *Indian J Pure Appl Phys*. 2014;52:24–29.
- [52] Benson GC, Kiyohara O. Evaluation of excess isentropic compressibilities and isochoric heat capacities. *J Chem Thermodyn*. 1979;11:1061–1064.
- [53] Zhong Y, Wang H, Diao K. Densities and excess volumes of binary mixtures of the ionic liquid 1-butyl-3-methylimidazolium hexafluorophosphate with aromatic compound at $T=(298.15 \text{ to } 313.15) \text{ K}$. *J Chem Thermodyn*. 2007;39:291–296.
- [54] Redlich O, Kister AT. Algebraic representation of thermodynamic properties and the classification of solutions. *Ind Eng Chem*. 1948;40:345–348.
- [55] Wood SE, Battino R. *Thermodynamics of chemical systems*. Cambridge: Cambridge University Press; 1990.
- [56] Iloukhani H, Zarei HA. Volumetric properties of dimethyl sulfoxide with some alcohols at 298.15 K. *Phys Chem Liq*. 2008;46:154–161.
- [57] Pal A, Kumar A, Kumar H. Volumetric properties of binary mixtures of some n-alkoxyethanols with 2-pyrrolidinone and N-methyl-2-pyrrolidinone at 298.15 K. *Indian J Chem*. 2002;41:2017–2024.
- [58] Wei Q, Guo X, Wang Y, et al. Temperature-dependent FTIR study on three kinds of hydrogen-bonded benzoic acid dimers in their melt states. *J Mol Liq*. 2013;177:225–228.
- [59] Silverstein RM, Webster FX. *Spectrometric Identification of Organic Compounds*. 6th ed. New Delhi: Wiley-India; 2007.



Data Article

Investigation on thermodynamic properties and spectroscopic studies of binary mixtures of 1, 2, 4-trichlorobenzene with alkyl acetates (C1-C5) at $T = (303.15 \text{ to } 318.15) \text{ K}$

R. Raju ^a, S. Ravikumar ^a, K. Sivakumar ^b, P. Bhanuprakash ^c, V. Pandiyan ^a  [Show more](#) 

Outline



Share



Cite

<https://doi.org/10.1016/j.cdc.2021.100781>[Get rights and content](#)

Abstract

The measurements of experimental densities (ρ) and speeds of sound (u) of binary mixtures of 1, 2, 4-trichlorobenzene (1,2,4-TCB) with alkyl acetates namely methyl acetate, ethyl acetate, propyl acetate, butyl acetate and pentyl acetate have been done over the entire composition range at four different temperatures ($T = 303.15, 308.15, 313.15$ and 318.15 K) and pressure ($P = 0.1 \text{ MPa}$). The intermolecular interactions present in these mixtures were briefly explained through the calculated excess molar volume (V_m^E), excess isentropic compressibility (κ_s^E) and excess speeds of sound (u^E). The ideal and excess parameters were correlated with Redlich-Kister polynomial equation. Different theoretical models such as PFP theory, CFT and FLT have been used to analyze the experimental results of V_m^E and u values respectively. The strength of intermolecular interactions between the component molecules have been confirmed using the excess properties and the results were further analyzed with FT-IR spectroscopic technique.

[Previous](#)[Next](#)

Keywords

Binary mixtures; 1, 2, 4-trichlorobenzene; Densities; Excess thermodynamic properties; Speeds of sound; FTIR studies

[Recommended articles](#)

Cited by (0)

[View full text](#)

© 2021 Published by Elsevier B.V.



Copyright © 2022 Elsevier B.V. or its licensors or contributors.
ScienceDirect® is a registered trademark of Elsevier B.V.

RELX™

Journal Pre-proof

Quantum cutting and near-infrared emissions in Ho³⁺/Yb³⁺ codoped transparent glass-ceramics

P. Babu, I.R. Martín, V. Lavín, U.R. Rodríguez-Mendoza, Hyo Jin Seo, K. Venkata Krishanaiah, V. Venkatramu

PII: S0022-2313(20)30606-2

DOI: <https://doi.org/10.1016/j.jlumin.2020.117424>

Reference: LUMIN 117424

To appear in: *Journal of Luminescence*

Received Date: 20 March 2020

Revised Date: 16 May 2020

Accepted Date: 2 June 2020

Please cite this article as: P. Babu, I.R. Martín, V. Lavín, U.R. Rodríguez-Mendoza, H.J. Seo, K.V. Krishanaiah, V. Venkatramu, Quantum cutting and near-infrared emissions in Ho³⁺/Yb³⁺ codoped transparent glass-ceramics, *Journal of Luminescence* (2020), doi: <https://doi.org/10.1016/j.jlumin.2020.117424>.

This is a PDF file of an article that has undergone enhancements after acceptance, such as the addition of a cover page and metadata, and formatting for readability, but it is not yet the definitive version of record. This version will undergo additional copyediting, typesetting and review before it is published in its final form, but we are providing this version to give early visibility of the article. Please note that, during the production process, errors may be discovered which could affect the content, and all legal disclaimers that apply to the journal pertain.

© 2020 Published by Elsevier B.V.



CRediT author statement

P. Babu: Conceptualization, Investigation, Writing – original/Revised draft preparation.

I.R. Martin: Methodology, Investigation.

V. Lavin: Investigation, Writing - Reviewing and Editing.

U.R. Rodriguez-Mendoza: Formal analysis.

Hyo Jin Seo: Methodology, Resources.

K. Venkata Krishnaiah: Software, Data curation.

V. Venkatramu: Validation

Quantum cutting and near-infrared emissions in $\text{Ho}^{3+}/\text{Yb}^{3+}$ codoped transparent glass-ceramics

P. Babu^{1,*}, I.R. Martín², V. Lavín², U.R. Rodríguez-Mendoza²,
Hyo Jin Seo³, K. Venkata Krishanaiah⁴, V. Venkatramu^{5,6}

¹Department of Physics, Government Degree College, Palamaner-517408, India

²Departamento de Física, MALTA Consolider Team, IMN, and IUdEA, Universidad de la Laguna, Apartado de Correos 456, E-38200 San Cristóbal de La Laguna, Santa Cruz de Tenerife, Spain

³Department of Physics, Pukyong National University, Busan, Republic of Korea

⁴Department of Physics, RGM College of Engineering and Technology, Nandyal – 518501, India

⁵Department of Physics, Yogi Vemana University, Kadapa-516 005, India

⁶Department of Physics, Krishna University Dr. MRAR PG Centre, Nuzvid -521 201, India

Abstract

Visible to near-infrared quantum cutting and 2.0 μm near-infrared emissions have been obtained in $\text{Ho}^{3+}/\text{Yb}^{3+}$ co-doped oxyfluoride transparent glass-ceramic, containing cubic CaF_2 nanocrystals, under 473 nm excitation. The formation of CaF_2 nanocrystals and the incorporation of $\text{Ho}^{3+}/\text{Yb}^{3+}$ ions into these nanocrystals have been confirmed from x-ray diffraction and photoluminescence studies, respectively. Lifetime of 1.2 μm emission has been enhanced by three orders of magnitude in the glass-ceramic compared to that of the precursor glass. Time-resolved near-infrared quantum cutting emission of Yb^{3+} ions at different delay times under 532 nm laser excitation has also been obtained. Studies reveal that the infrared quantum cutting emission of Yb^{3+} and Ho^{3+} ions in the CaF_2 nanocrystalline glass-ceramic could improve the efficiency of crystalline-Si solar cells, and that the 1.2 μm emission could be useful for further enhancing transmission windows using optical amplifiers.

Keywords: Oxyfluoride glass-ceramics; $\text{Ho}^{3+}/\text{Yb}^{3+}$ ions; CaF_2 nanocrystals;
Downconversion; Near-infrared quantum cutting

*Corresponding authors: drbabu64@gmail.com (P. Babu)

1. INTRODUCTION

A transparent oxyfluoride glass-ceramic (TGC) is a two-phase material containing fluoride nanocrystals that precipitate in an amorphous environment during the controlled thermal treatment of the precursor glass. In recent years, TGCs have attracted great deal of interest due to their potential applications in diverse fields of science and technology [1-3]. Alumina-silicate based glasses are most suitable for precipitation of fluoride nanocrystals due to their excellent thermal, chemical and mechanical properties compared to phosphate or fluoride glasses. Further, in these TGCs, the host for the trivalent lanthanide (Ln^{3+}) ions corresponds to fluoride crystals with low phonon energy and, hence, low multiphonon probabilities, which results in increasing the luminescence efficiency of these materials compared to their precursor glasses [3]. Ln^{3+} ions doped TGCs are widely investigated as they exhibit both upconversion (UC) and downconversion (DC) processes besides excellent Ln^{3+} ion solubility [4]. Recently, TGCs containing fluoride nanocrystals have been explored for laser cooling applications as they show extraordinary properties, including high photoluminescence quantum yield and low background absorption [5-7].

Trivalent holmium, Ho^{3+} , ion is suitable for infrared-to-visible upconversion since it has two pumping energy levels, $^5\text{F}_5$ and $^5\text{I}_4$, along with a relatively long lived intermediate energy level, $^5\text{I}_7$, that acts as a good population reservoir for upconversion processes. As a result, in recent times there is significant amount of interest in Ho^{3+} -doped glasses and crystals as possible upconversion materials. Further, Ho^{3+} -doped glass fibers are found to emit continuous wave upconversion laser under red light pumping [8]. In addition, Yb^{3+} ion has a relatively simple energy level structure with the $^2\text{F}_{7/2}$ level as ground state and the $^2\text{F}_{5/2}$ level as excited state. Its broad emission, ranging between 900 and 1100 nm, overlaps with the crystalline silicon's band

gap of ~ 1.12 eV, making Yb^{3+} ion an important candidate for near-infrared (NIR) quantum cutting (QC) materials to improve the efficiency of crystalline-silicon (C-Si) solar cells [9]. Materials co-doped with Yb^{3+} ions and other Ln^{3+} ions are attractive for the development of upconversion devices. In the specific case of Ln^{3+} (Er^{3+} , Tm^{3+} or Ho^{3+}) ions, resonance energy transfer is facilitated by the energy matching of their excited states with that of Yb^{3+} ion [10]. The Yb^{3+} ion is found to be efficient sensitizer for Ho^{3+} lasers [2], due to considerable energy match between Yb^{3+} and Ho^{3+} ions and hence, $\text{Ho}^{3+}/\text{Yb}^{3+}$ couple is a good choice for NIR QC investigations [11]. The NIR QC, which converts one UV-blue photon into two NIR photons of ~ 1.0 μm , has attracted more attention for their application in plasma display, mercury free fluorescent tubes, and solar cells [11,12]. In recent times, more emphasis has been focused on NIR QC in different systems with the combination of different Ln^{3+} ions with Yb^{3+} ions, for example, $\text{Nd}^{3+}/\text{Yb}^{3+}$ [13], $\text{Tb}^{3+}/\text{Yb}^{3+}$ [14-17], $\text{Er}^{3+}/\text{Yb}^{3+}$ [18,19], $\text{Tm}^{3+}/\text{Yb}^{3+}$ [20], $\text{Pr}^{3+}/\text{Yb}^{3+}$ [13,21] $\text{Ho}^{3+}/\text{Yb}^{3+}$ [9,22,23], and $\text{Yb}^{2+}/\text{Yb}^{3+}$ [24] to enhance the efficiency of solar cells. On the other side, solid state laser working in the infrared region at 2 μm is attracting increasing interest for its wide range of applications such as remote sensing, optical parametric oscillators, eye safe LIDAR, biomedical applications, environmental sensing, etc. [2,25]. Among the Ln^{3+} ions, Ho^{3+} is one of the important active ions that can emit at 2 μm through the ${}^5\text{I}_7 \rightarrow {}^5\text{I}_8$ transition.

In the present work, $\text{Ho}^{3+}/\text{Yb}^{3+}$ codoped TGCs containing CaF_2 nanocrystals have been synthesized through post-thermal treatment method and their visible, QC and NIR emissions have been measured exciting at 473 nm. NIR QC emissions are observed at 1.0 and 1.2 μm wavelengths under 473 nm excitation and their possible mechanisms are discussed. The NIR emission spectra at 2.0 μm have been measured in glass and GCs and explained their variation

with respect to size of the nanocrystals. Absorption and emission cross-sections and figure of merit for the 1.2 μm and 2.0 μm emissions have also been calculated.

2. EXPERIMENTAL DETAILS

Precursor $\text{Ho}^{3+}/\text{Yb}^{3+}$ co-doped oxyfluoride glass, with composition (in mol%) $45\text{SiO}_2 - 20\text{Al}_2\text{O}_3 - 8\text{CaO} - 24\text{CaF}_2 - 2\text{Yb}_2\text{O}_3 - 1\text{Ho}_2\text{O}_3$, was prepared by the melt-quenching technique at 1400 $^\circ\text{C}$ for 2 h using a covered platinum crucible. The melt was poured onto a pre-heated brass mold kept just below the glass transition temperature (T_g), at which glass samples were annealed, and slowly cooled to room temperature to avoid thermal stress and strains. Finally, glass samples were annealed for 4h at 650, 675, 700 and 725 $^\circ\text{C}$ (hereafter referred to as GC1, GC2, GC3 and GC4, respectively), close to the onset of crystallization temperature T_c (675 $^\circ\text{C}$) of CaF_2 nanocrystals to transform them into glass-ceramics. Structural differences between the precursor glass and glass-ceramics were identified by using X-ray diffraction technique, performed with a Thermo ARL X'TRA powder diffractometer with Cu-K_α radiation (1.54 \AA).

Visible and NIR quantum cutting emissions were obtained by pumping with a cw laser at 473 nm and the emission was collimated and focalized in an optical fiber coupled to a ANDOR spectrograph, a SR-303i-B equipped with a Newton 970EMCCD camera for the visible range, and an SR-500i-B2 with a iDusInGaAs photodiode array for the NIR range. The time-resolved fluorescence was obtained by exciting the samples with an EKSPLA 10 ns pulsed Optical Parametric Oscillator (OPO) laser and recording the luminescence with a Jobin-Yvon 320 spectrometer equipped with a Hamamatsu NIR-extended photomultiplier connected to a Lecroy digital storage oscilloscope.

3. RESULTS AND DISCUSSION

3.1. X-ray diffraction spectra

X-ray diffraction (XRD) patterns of Ho³⁺/Yb³⁺-doped precursor glass and glass-ceramics are shown in Fig. 1. The profile of the precursor glass contains two broad curves typical of an amorphous structure, whereas the GCs contain several additional sharp peaks related to the diffraction pattern of a crystalline structure, which can be identified as the CaF₂ cubic phase with *Pm3m* ($\alpha = \beta = \gamma = 90^\circ$) space group, by comparing with standard data (JCPDS Card No. 35-0816). These crystals form nanostructures that are found to precipitate from the precursor aluminosilicate glass through a suitable thermal treatment that, from the XRD peak widths and using the Scherer's formula [26], sizes of the nanocrystals are found to be around 8, 10, 13 and 18 nm for GC1, GC2, GC3 and GC4, respectively. Samples exhibit only the cubic phase and no second phase is detected in the XRD pattern, indicating the successful formation of CaF₂ nanocrystals.

3.2. Emission spectra and decay curves

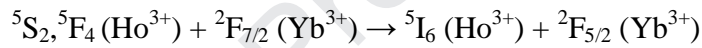
3.2.1. Visible emission spectra

Visible emission spectra of glass (G) and glass-ceramics (GCs) are measured exciting the ⁵I₈→⁵F₃ transition of the Ho³⁺ ion under 473 nm laser excitation, and are shown in Fig. 2. Spectra consist of three bands centered at ~542, ~648 and ~752 nm corresponding to the ⁵S₂,⁵F₄→⁵I₈, ⁵F₅→⁵I₈ and ⁵S₂,⁵F₄→⁵I₇ transitions, respectively. When samples are excited, Ho³⁺ ions reach the ⁵F₃ level, from which a fast non-radiative decay takes place and ions reach the ⁵S₂,⁵F₄ metastable multiplets, resulting in green emission at ~542 nm and red emission at ~752 nm. From the ⁵S₂,⁵F₄ levels further non-radiative deexcitation processes populates the ⁵F₅ level, resulting in ⁵F₅→⁵I₈ emission at ~648 nm. Mechanisms of excitation and emissions are

shown in Fig. 3. Lin *et al.* [27] obtained similar emission spectra in Ho³⁺/Yb³⁺ co-doped GC with YF₃ nanocrystals under 488 nm excitation. Out of these three transitions, the green emission is more intense than the other two. As can be seen from Fig. 2, the emission intensity and splitting of the bands increases from glass to GC4, indicating the progressive incorporation of Ho³⁺ ions into the CaF₂ nanocrystals and the increase in size of the nanocrystals.

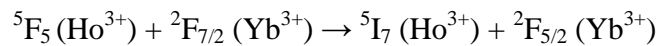
3.2.2. Quantum cutting and 1.2 μm emission spectra

As already mentioned, when the samples are excited with a 473 nm cw laser, the Ho³⁺ ions are excited to the ⁵F₃ level, followed by a non-radiative relaxation to the ⁵S₂,⁵F₄ level. From this level, the following resonant cross-relaxation energy transfer, denoted as CR1 in Fig. 3, occurs:



and one Ho³⁺ 1180 nm photon (from the ⁵I₆ level) and one Yb³⁺ 980 nm photon (from the ²F_{5/2} level) are emitted.

Further, non-radiative multiphonon relaxations from the ⁵S₂,⁵F₄ levels populate the ⁵F₅ one and, from this level, another resonant cross-relaxation energy transfer, shown as CR2 in Fig. 3, takes place as follows:



resulting in the emission of one Ho³⁺ 2.0 μm photon (from the ⁵I₇ level) and one Yb³⁺ 980 nm photon (from the ²F_{5/2} level). All these excitations, CR and emissions channels are shown in the partial energy level diagram of Yb³⁺ and Ho³⁺ ions in Fig. 3. It is worth noting that Zhou *et al.* [26] and Lin *et al.* [27] proposed similar mechanisms to explain QC processes in Ho³⁺/Yb³⁺ codoped glass-ceramics.

Emissions from Yb^{3+} (${}^2\text{F}_{5/2} \rightarrow {}^2\text{F}_{7/2}$) and Ho^{3+} (${}^5\text{S}_2, {}^5\text{F}_4 \rightarrow {}^5\text{I}_6$) ions overlap giving a wide band in the range of 950-1100 nm, as shown in Fig. 4. Additionally, Yb^{3+} emissions consist of two peaks, a sharp one at ~980 nm and broader one at ~1020 nm, attributed to emission from the lowest Stark level of ${}^2\text{F}_{5/2}$ multiplet to the lowest and next higher Stark levels of the ${}^2\text{F}_{7/2}$ ground multiplet, respectively [28]. The intensity of Yb^{3+} emissions increases, due to the change of the Ln^{3+} local structure, from glass to glass-ceramic GC3, and then decreases marginally for GC4, which could be due to back transfer processes from Yb^{3+} to Ho^{3+} ions. The ${}^5\text{I}_6 \rightarrow {}^5\text{I}_8$ transition gives emission at ~1.2 μm and is also shown in Fig. 4 for the glass and GCs. Their intensities are higher compared to those of 1.0 μm , and increase monotonically from the glass to the glass-ceramic GC4 with the increase in size of the nanocrystals and the progressive incorporation of Ho^{3+} ions into low phonon energy CaF_2 nanocrystals.

As can be seen from Figs. 2 and 4, in moving from glass to GC4, the enhancement factor of the intensity is higher for the ${}^5\text{I}_6 \rightarrow {}^5\text{I}_8$ emission band compared to the ${}^5\text{S}_2, {}^5\text{F}_4 \rightarrow {}^5\text{I}_7$ band of Ho^{3+} ions. This can be explained taking into account that the energy difference between the ${}^5\text{S}_2, {}^5\text{F}_4$ and ${}^5\text{F}_5$ levels is ~3020 cm^{-1} whereas the difference between the ${}^5\text{I}_6$ and ${}^5\text{I}_7$ levels is ~3540 cm^{-1} (from absorption spectrum). Larger energy gap results in lower multiphonon relaxation from the upper level. In moving from glass to GC4, phonon energy of the host progressively decreases. As a result of this, there is progressive increase in radiative emission from the ${}^5\text{I}_6$ level compared to the ${}^5\text{S}_2, {}^5\text{F}_4$ level in moving from glass to GC4. Another reason for higher enhancement factor of the ${}^5\text{I}_6 \rightarrow {}^5\text{I}_8$ emission could be increase in CR1 process, in moving from glass to GC4, which depopulates the ${}^5\text{S}_2, {}^5\text{F}_4$ level and populates the ${}^5\text{I}_6$ one.

Quantum cutting (QC) is a process in which one photon of high energy converts into two photons of lower energy. This process in the Ho^{3+} ions, where each photon at 473 nm that is absorbed can produce two NIR photons, given by ${}^2\text{F}_{5/2} \rightarrow {}^2\text{F}_{7/2}$ & ${}^5\text{I}_6 \rightarrow {}^5\text{I}_8$ (1.0 & 1.2 μm) and ${}^2\text{F}_{5/2} \rightarrow {}^2\text{F}_{7/2}$ & ${}^5\text{I}_7 \rightarrow {}^5\text{I}_8$ (1.0 & 2.0 μm). The low energy photons (~ 1.2 and ~ 2.0 μm) are more intense and efficient as they occur only between Ho^{3+} ions, whereas the former ones (~ 1.0 μm) involves energy transfer from Ho^{3+} to Yb^{3+} ions and, hence, they are weaker.

The effect of Yb^{3+} ions can be analyzed using the decay curves of the ${}^2\text{F}_{5/2}$ level of Yb^{3+} ions in glass and GC3. These decays are measured by exciting them with a 944 nm laser radiation and monitoring the emission at ~ 1020 nm, where there is shoulder in the Yb^{3+} ions emission, and are shown in Fig. 5. Both decay curves are clearly non-exponential and the average lifetimes [11] are found to be ~ 15 and ~ 28 μs for glass and GC3, respectively. It is interesting to note that the lifetime in GC3 increases significantly, almost by a factor of 2, due to the presence of Yb^{3+} ions in a low phonon energy CaF_2 nanocrystalline environment.

Decay curves for the ${}^5\text{I}_6 \rightarrow {}^5\text{I}_8$ transition of Ho^{3+} ions at 1.2 μm measured in the glass and the glass-ceramics, under 473 nm laser excitation, are shown in Fig. 6. As can be seen, all decay curves are non-exponential in nature and consists of short and long components. The short component corresponds to ions that reside in the glass matrix and are not incorporated in the nanocrystals. But, as can be seen from Fig. 6, this component is reduced from GC1 to GC4. Lifetime of the long component of 1.2 μm decay, which is due to ions present in CaF_2 nanocrystals, increases with the increase in the size of nanocrystals from 15 μs (Glass/GC1) to 1.586 ms (GC4). It is worth noting that the lifetime in GC4 is three orders of magnitude (~ 1006 times) longer compared to that of the glass, due to the presence of Ho^{3+} ions in low phonon energy CaF_2 nanocrystals. The present lifetime of the 1.2 μm emission of Ho^{3+} ion in GC4 is

longer compared to other reported Ho^{3+} doped matrices, such as CaSc_2O_4 ceramic [29] or water-free fluorotellurite glasses [30].

Fig. 7 shows the time-resolved NIR QC emission of Yb^{3+} ions at different delay times after exciting with a 532 nm laser light, resonant with the $^5\text{I}_8 \rightarrow ^5\text{F}_4, ^5\text{S}_2$ transition of Ho^{3+} ions. The emission spectra consist of overlapped bands at ~894, ~911, ~980 and ~1020 nm due to Stark's splitting of the excited $\text{Yb}^{3+}: ^2\text{F}_{5/2}$ multiplet and the $^5\text{F}_4, ^5\text{S}_2 \rightarrow ^5\text{I}_6$ transition of Ho^{3+} ions at ~1010 nm. The energy transfer from Ho^{3+} ions is responsible for the emission of Yb^{3+} ions. The emission intensity and full width at half maximum of the 980 nm emission band increases with the increase in delay time, due to population differences among the thermally coupled levels of Yb^{3+} ions in the matrix.

In order to study the energy transfer process more accurately, luminescence decay curves are obtained by exciting $^5\text{I}_8 \rightarrow ^5\text{F}_4, ^5\text{S}_2$ transition at 532 nm of the Ho^{3+} ions and monitoring the emissions at ~975 and ~1010 nm, respectively, as shown in Fig. 8. The decay curves indicate that the energy transfer process is predominant at higher delay times because the Yb^{3+} ions are excited through CR1 or CR2 processes from Ho^{3+} ions. The rising edge in the decay curve (975 nm) of Fig. 8 indicates the slow population process of the $^2\text{F}_{5/2}$ level of Yb^{3+} ions through energy transfer from Ho^{3+} ions. This provides a strong evidence for the energy transfer from the Ho^{3+} to Yb^{3+} ions [31]. On the contrary, in the emission at ~1010 nm, associated with the $^5\text{F}_4, ^5\text{S}_2 \rightarrow ^5\text{I}_6$ transition, predominates the emission coming from Ho^{3+} ions initially excited.

The emission cross-section between a high energy level and a lower energy level can be derived using the McCumber [32] theory,

$$\sigma_{em}(\lambda) = \sigma_{ab}(\lambda) \frac{Z_l}{Z_u} \exp\left(\frac{h\nu - E_{ZL}}{k_B T}\right) \quad (1)$$

where σ_{ab} is absorption cross-section, $\sigma_{ab} = \alpha(\lambda)/N$, where $\alpha(\lambda)$ is the experimental absorption coefficient and N is the concentration of Ho^{3+} ions; Z_l and Z_u are the partial functions of lower and upper levels, respectively; k_B is Boltzmann's constant; $E_j - E_i = h\nu - E_{ZL}$ is the energy separation between the two levels; and E_{ZL} is the 'zero line' energy, i.e. the energy of the transition from the lowest Stark sublevels of upper and lower manifold.

Absorption and emission cross-sections ($\times 10^{-20} \text{ cm}^2$) are calculated for the 1.2 μm emission of the Ho^{3+} ion and are found to be 0.93 and 5.2 for the precursor glass and 1.16 and 6.7 for the glass-ceramic GC4. Values of emission-cross-sections of glass and GC4 are much larger than those of TZNF60 glass ($0.63 \times 10^{-20} \text{ cm}^2$) [30] and oxyfluoride nano glass-ceramic ($0.27 \times 10^{-20} \text{ cm}^2$) [33]. Figure of merit (FOM), defined as the product of experimental lifetime and emission cross-section [34], for the 1.2 μm emission is found to be $0.08 \times 10^{-23} \text{ cm}^2 \cdot \text{s}$ for glass and $10720 \times 10^{-23} \text{ cm}^2 \cdot \text{s}$ for the glass-ceramic GC4. The FOM for GC4 is found to be about 1000 times higher than that of glass. The higher value of FOM indicates higher gain for the 1.2 μm emission in GC4.

3.2.3. 2.0 μm emission spectra

NIR emission spectra of the oxyfluoride glass and the glass-ceramics at around 2.0 μm are measured by exciting $^5\text{I}_8 \rightarrow ^5\text{F}_3$ transition using a 473 nm laser light and are shown in Fig. 9. As can be seen, the intensity of the bands increases from the glass to the glass-ceramic GC3 and then decreases slightly for GC4. This could be due to decrease in the magnitude of the cross-relaxation processes, CR2 in GC4, which feeds $^5\text{I}_7$ level, due to decrease in multiphonon relaxation from $^5\text{S}_2, ^5\text{F}_4$ to $^5\text{F}_5$ level. The full width at half maximum (FWHM) of the all the

emissions of the present study, from glass to GC4, is found to be around 153 nm (386 cm^{-1}), which is slightly larger than 149 nm found in TZNF60 glass [26] but less than 171 nm found in germinate glass [35].

Absorption and emission cross-sections ($\times 10^{-20} \text{ cm}^2$) of the $2.0 \mu\text{m}$ band calculated using Eq. (1) are found to be 2.1 and 5.39 for the precursor glass and 2.09 and 5.79 for the glass-ceramic GC4, respectively. The absorption and emission cross-sections ($\times 10^{-20} \text{ cm}^2$) of the present study are larger than those found in oxyfluoride glass ($\sigma_{ab}= 0.498$, $\sigma_{em}= 0.47$) and glass-ceramic GC C ($\sigma_{ab}= 0.56$, $\sigma_{em}= 0.66$) [2] and TZNF60 glass ($\sigma_{ab}= 0.68$, $\sigma_{em}= 0.72$) [26].

The wavelength dependent gain cross-section can be expressed as:

$$\sigma_g(\lambda) = \gamma\sigma_{em}(\lambda) - (1 - \gamma)\sigma_{ab}(\lambda) \quad (2)$$

where σ_{em} and σ_{ab} represents emission and absorption cross-sections, respectively, and γ (0 to 1 with an increments of 0.1) represents the population of Ho^{3+} ions. Gain cross-section spectra of the $^5\text{I}_8 \leftrightarrow ^5\text{I}_7$ transitions of Ho^{3+} ion at $2.0 \mu\text{m}$ as a function of population inversion for a glass and the glass-ceramic GC4 are shown in Figs.10 (a) and (b), respectively. Gain is positive when the population inversion is equal or greater than 0.3. However, broadening is more predominant for GC4 compared to glass. The gain is found to be 5.79 cm^{-2} for GC4 which is higher than that of glass, 5.35 cm^{-2} . The value of gain is very high compared to those of reported tellurite [35] and fluorophosphate [37] glasses. It is observed from the gain spectra that a tunable wavelength range of 1900-2100 nm is expected when the population inversion is greater than or equal to 0.5. These results reveal that the Ho^{3+} -doped glass-ceramics have potential for optical amplifiers.

4. CONCLUSIONS

The Ho^{3+} - Yb^{3+} co-doped transparent oxyfluoride glass and glass-ceramics containing CaF_2 nanocrystals have been investigated. X-ray diffraction patterns confirm the formation of CaF_2 nanocrystals in the glass matrix. The size of the nanocrystals increases from 8 to 18 nm with increasing the thermal treatment temperature of the precursor glass. Near-infrared quantum cutting as well as 2.0 μm eye safe emissions are obtained in Yb^{3+} ions and Ho^{3+} ions, respectively by exciting with 473 nm laser at the $^5\text{F}_2$ level of Ho^{3+} ions. The similar emission is also achieved at different delay times by exciting the $^5\text{F}_4$ level of Ho^{3+} ions at 532 nm. The decay curves of Yb^{3+} emission evidences the energy transfer process from Ho^{3+} to Yb^{3+} ions. It is worth noting that lifetime of 1.2 μm emission has been enhanced by three order of magnitude in GC4 sample compared to that of the precursor glass. Intense Yb^{3+} and Ho^{3+} near-infrared emissions indicate that the present oxyfluoride glass-ceramics containing CaF_2 nanocrystals have potential application in realizing the solar spectrum to enhance the efficiency of c-Si solar cells.

ACKNOWLEDGEMENTS

This research has been partially supported by Spanish Ministerio de Economía y Competitividad (MINECO) under the Spanish National Program of Materials (MAT2016-75586-C4-4-P), the Agencia Canaria de Investigación, Innovación y Sociedad de la Información (ProID2017010078), and by EU-FEDER funds. Two of the authors Babu and Venkatramu are also grateful to DST, New Delhi for the sanction of research project (No. INT/PORTUGAL/P-04/2017) under India-Portugal bilateral scientific and technological cooperation.

REFERENCES

- [1]. F. Lahoz, S.E. Hernández, N.E. Capuz, D. Navarro-Urrios, *Appl. Phys. Lett* 90 (2007) 201117-1-201117-3.
- [2]. J. Pan, R. Xu, Y. Tian, K. Li, L. Hu, J. Zhang, *Opt. Mater.* 32 (2010) 1451-1455.
- [3]. G. Gorni, J.J. Velazquez, J. Mosa, G. C. Mather, A. Serrano, M. Vila, G.R. Castro, D. Bravo, R. Balda, J. Fernandez, A. Duran, Y. Castro, *Nano Mater.* 9 (2019) 530-545.
- [4]. L.M. Almeida, *Fluoride glasses*, Handbook on the Physics and Chemistry of Rare-Earths, In: K.A. Gschneidner Jr, L. Eyring (Eds.), Vol. 5, Elsevier Science Publishers, 1991, p. 287-346.
- [5]. K. Venkata Krishnaiah, E.S. de L. Filho, Y. Ledemi, G. Nemova, Y. Messaddeq, R. Kashyap, *Sci. Reports* 6 (2016) 21905-1-21905-12.
- [6]. E. S. de L. Filho, K. Venkata Krishnaiah, Y. Ledemi, Y.J. Yu, Y. Messaddeq, G. Nemova, R. Kashyap, *Opt. Exp.* 23 (2015) 4630-4640.
- [7]. K. Venkata Krishnaiah, Y. Ledemi, E.S. de L. Filho, G. Nemova, Y. Messaddeq, R. Kashyap, *Opt. Eng.* 56 (2017) 011103-1-011103-5.
- [8]. J.C. Boyer, F. Vetrone, J.A. Capobianco, A. Speghini, and M. Bettinelli, *J. Appl. Phys.* 93 (2003) 9460-9465.
- [9]. D.C. Yu, X.Y. Huang, S. Ye, Q.Y. Zhang, *J. Alloys Compds.* 509 (2011) 9919-9923.
- [10]. A. Volokitina, P. Loiko, O. Dymshits, M. Tsenter, S. Zapalova, K. Bogdanov, A. Baranov, A. Zhilin, *J. Phys. Conf. Series* 917 (2017) 062024-062027.
- [11]. L. Guo, Y. Wang, J. Zhang, Y. Wang, P. Dong, *Nano Scale Res. Lett.* 7 (2012) 636-642.
- [12]. D. Chen, Y. Wang, Y. Yu, P. Huang, F. Weng, *Opt. Lett.* 33 (2008) 1884-1886.
- [13]. L.J. Borrero-González, L.A.O. Nunes, *J. Phys.: Condens. Matter* 24 (2012) 385501-1-385501-7.
- [14]. S. Ye, B. Zhu, J. X. Chen, J. Luo, J.R. Qiu, *Appl. Phys. Lett.* 92 (2008) 141112-1-141112-3.
- [15]. Y. Wang, L. Xie, H. Zhang, *J. Appl. Phys.* 105 (2009) 023528-1-023528-4.
- [16]. Q.Y. Zhang, C.H. Yang, Y.X. Pan, *Appl. Phys. Lett.* 90 (2007) 021107-1-021107-3.

- [17]. Y. Arai, T. Yamashidta, T. Suzuki, Y. Ohishi, *J. Appl. Phys.* 105 (2009) 083105-1-083105-6.
- [18]. A.L. Arrts, O.M. vander Ende, A. Meijerink, *J. Appl. Phys.* 106 (2009) 023522-1-023522-6.
- [19]. J.J. Eilers, D. Biner, J.T.V. Wijngaarden, K. Kramer, H.U. Gudel, A. Meijerink, *Appl. Phys. Lett.* 96 (2010) 151106-1-151106-3.
- [20]. L. Xie, Y. Wang, H. Zhang, *Appl. Phys. Lett.* 94 (2009) 061905-1-061905-3.
- [21]. B. Bryan, M. van der Ende, L. Aarts, A. Meijerink, *Adv. Mater.* 21 (2009) 3073-3077.
- [22]. K. Deng, T. Gong, L. Hu, X. Wei, Y. Chen, M. Yin, *Opt. Express* 19 (2011) 1749-1754.
- [23]. Z. Hou, H. Li, Z. Xue, M. Wang, X. Hu, S. Wang, *J. Alloys Compds.* 640 (2015) 311-316.
- [24]. Y. Teng, J. Zhou, X. Liu, S. Ye, J. Qiu, *Opt. Exp.* 18 (2010) 9671-9676.
- [25]. J. He, H. Zhan, Z. Zhou, A. Zhang, A. Lin, *Opt. Mater.* 35 (2013) 2573-2576.
- [26]. X. Zhou, Y. Wang, X. Zhao, L. Li, Z. Wang, Q. Li, *J. Am. Ceram. Soc.*, 97 (2014) 179-184.
- [27]. H. Lin, D. Chen, Y. Yu, A. Yang, Y. Wang, *Opt. Lett.* 36 (2011) 876-878.
- [28]. K. Venkata Krishnaiah, C.K. Jayasankar, S. Chaurasia, C.G. murali, L.J. Dhareshwar, *Sci. Advan. Mater.* 5 (2013) 276-284.
- [29]. Ş. Georgescu, A. Ştefan, O. Toma, A.-M. Voiculescu, *J. Lumin.* 162 (2015) 174-179.
- [30]. J. He, H. Zhan, Z. Zhou, A. Zhang, A. Lin, *Opt. Commun.* 320 (2014) 68-72.
- [31]. Q. Zou, P. Huang, W. Zheng, W. You, R. Li, D. Tu, J. Xu, X. Chen, *Nanoscale* 9 (2017) 6521-6528.
- [32]. D.E. McCumber, *Phys. Rev. A*, 136 (1964) A954-A957.
- [33]. K. Driesen, V.K. Tikhomirov, C.G. Walrand, V.D. Rodriguez, *Appl. Phys. Lett.* 88 (2006) 073111-1-073111-3.
- [34]. A.S. Pinheiro, A.M. Freitas, G.H. Silva, M.J.V. Bell, V. Anjos, A.P. Carmo, N.O. Dautas, *Chem. Phys. Lett.* 592 (2014) 164-169.
- [35]. M. Cai, B. Zhou, F. Wang, Y. Tian, J. Zhou, S. Xu, J. Zhang, *Opt. Mater. Exp.* 5 (2015) 1431-1439.

- [36]. K. Damak, El Sayed Yousef, A.S. Al-Shihri, H.J. Seo, C. Rüssel, R. Maâle, Solid State Sci. 28 (2014) 74-80.
- [37]. L.X. Yi, M. Wang, S.Y. Feng, Y.K. Chen, G.N. Wang, L.L. Hu, J.J. Zhang, Opt. Mater. 31 (2009) 1586-1590.

Journal Pre-proof

Figures

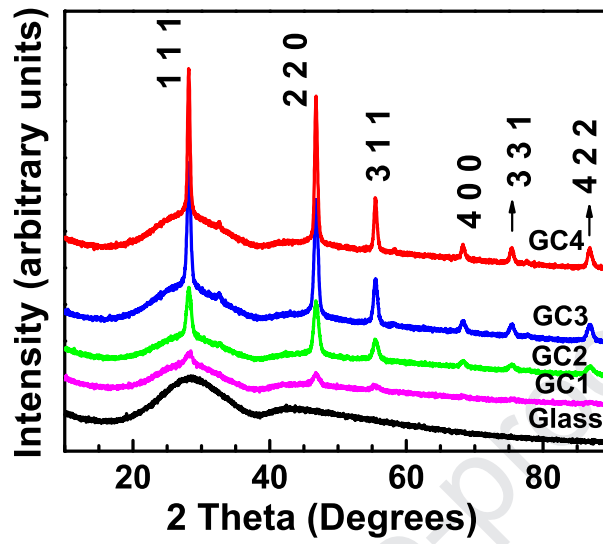


Fig.1. X-ray diffraction patterns of the oxyfluoride glass and glass-ceramics.

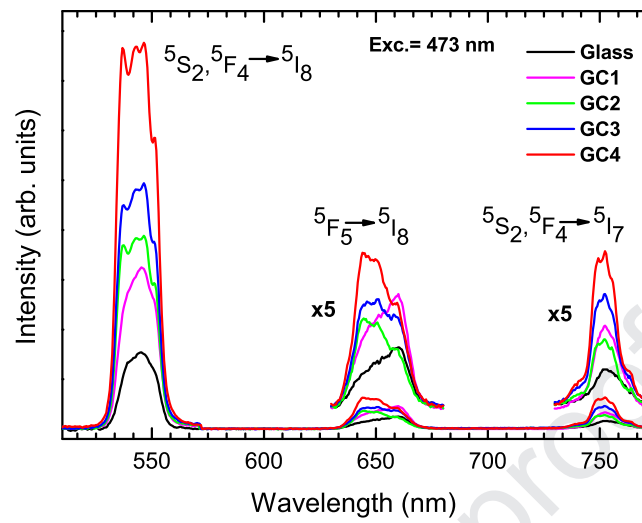


Fig. 2. Visible emissions of Ho^{3+} ions in the oxyfluoride glass (G) and glass-ceramics (GC) under 473 nm laser excitation.

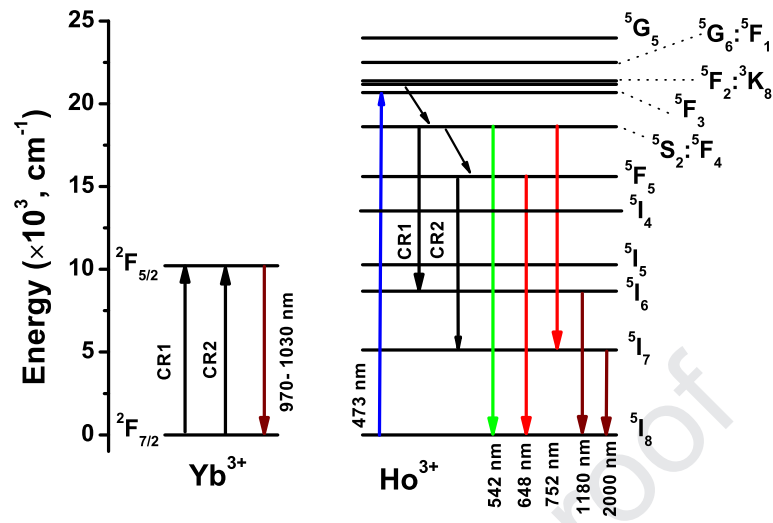


Fig.3. Partial energy level diagram of the oxyfluoride glass and glass-ceramics.
CR indicates a cross-relaxation channel.

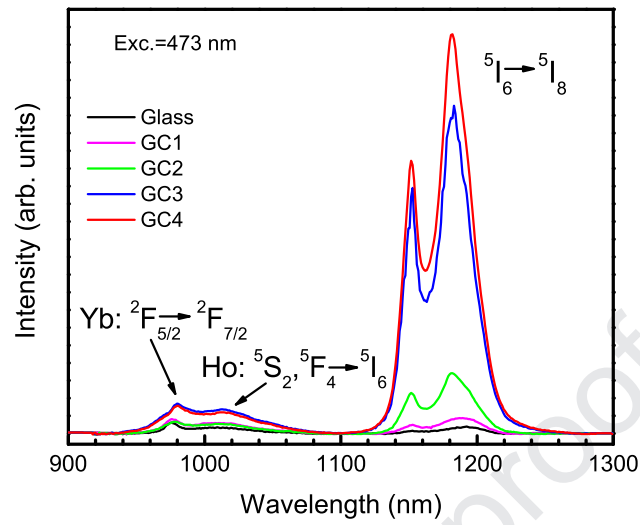


Fig. 4. Quantum cutting emissions of Yb³⁺ and Ho³⁺ ions in the oxyfluoride Glass (G) and glass-ceramics (GC) under 473 nm laser excitation.

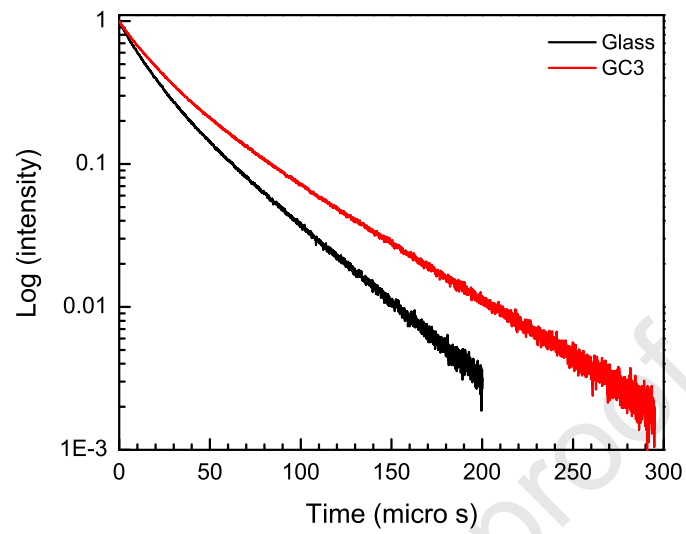


Fig. 5. Decay curves of the Yb³⁺ ions in the oxyfluoride glass (G) and glass-ceramic (GC3) exciting at 944 nm and monitoring the emission at 1020 nm, where there is shoulder in the Yb³⁺ emission.

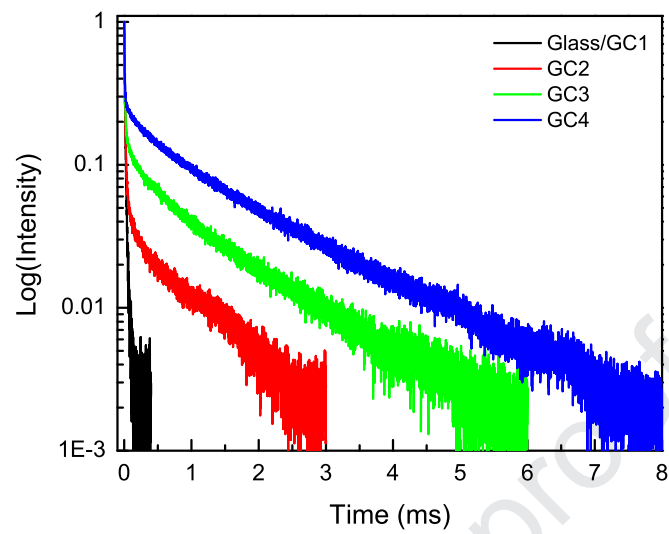


Fig. 6. Decay curves of the Ho^{3+} ion in the oxyfluoride glass (G) and glass-ceramics (GC) exciting at 473 nm and monitoring the emission at 1.2 μm .

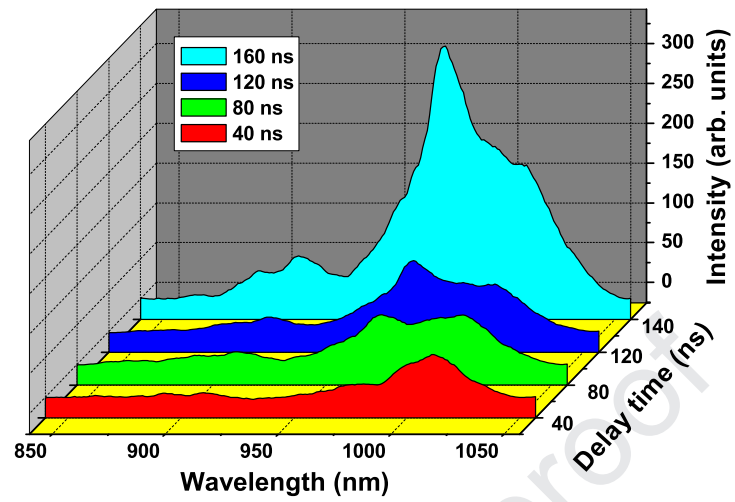


Fig. 7. Time-resolved near-infrared quantum cutting emissions of Yb³⁺ ions at different delay times after a 532 nm pulsed-laser excitation in a glass-ceramic (GC3).

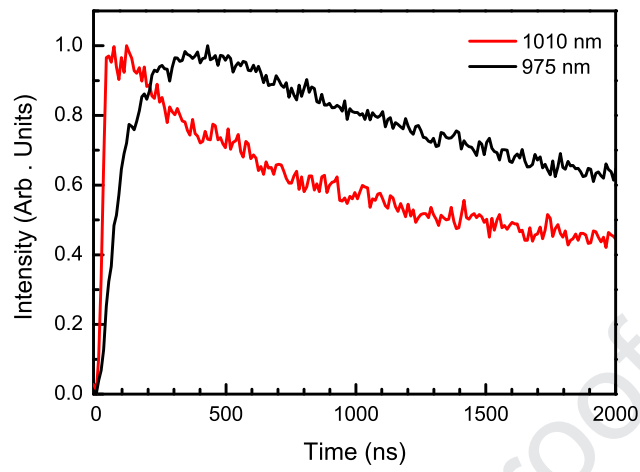


Fig. 8. Decay curves of Yb³⁺ (975 nm) and Ho³⁺ (1010 nm) ions in glass-ceramic (GC3) under 532 nm pulsed laser excitation.

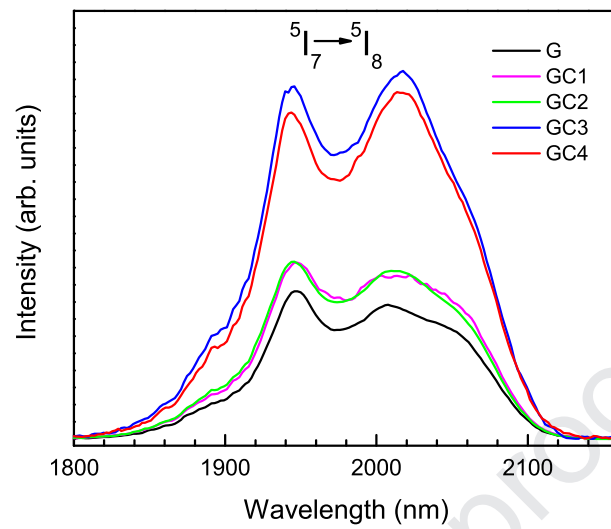


Fig. 9. Near infrared emissions of Ho³⁺ ions in the oxyfluoride glass (G) and glass-ceramics (GC) under 473 nm laser excitation.

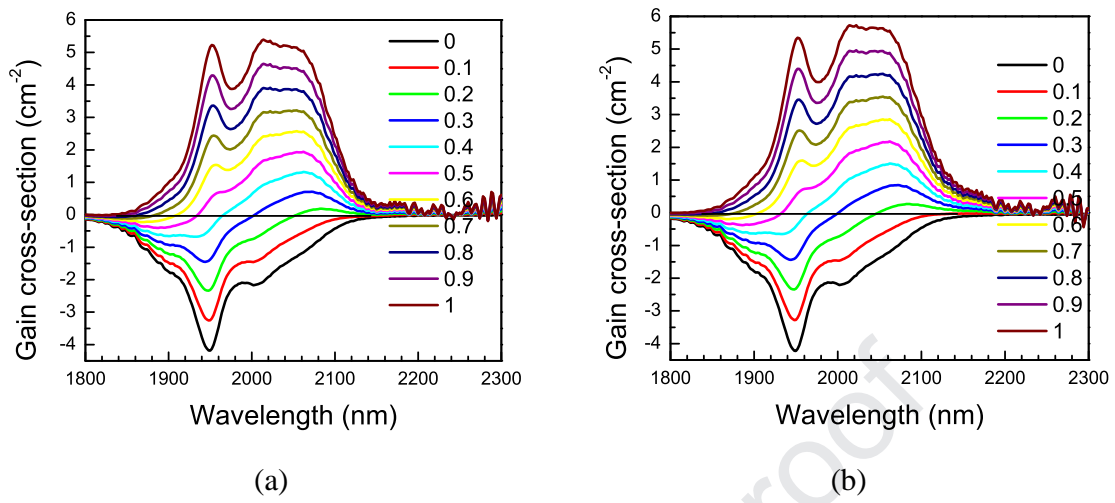


Fig. 10. Gain cross-section spectra of Ho³⁺ ion at 1950 nm in Ho³⁺/Yb³⁺-doped oxyfluoride (a) glass and (b) glass-ceramic (GC4).

Research Highlights:

- Ho^{3+} - Yb^{3+} co-doped oxyfluoride glass and glass-ceramics (GC) have been synthesized.
- Samples show quantum cutting (QC) and near infrared emissions under 473 nm excitation.
- Lifetime of 1.2 μm emission has been enhanced by three orders of magnitude in GC compared to precursor glass.
- 1.0 μm QC emission of Yb^{3+} ions could improve the efficiency of Si solar cells.
- 1.2 μm QC emission of Ho^{3+} ions could be useful for enhancing transmission windows of optical amplifiers.

Declaration of interests

The authors declare that they have no known competing financial interests or personal relationships that could have appeared to influence the work reported in this paper.

Journal Pre-proof



Optical Absorption and NIR Photoluminescence of Nd³⁺-Activated Strontium Phosphate Glasses

R.N.A. PRASAD,¹ N. VIJAYA,² P. BABU,³ N. KRISHNA MOHAN,¹
and R. PRAVEENA ^{4,5}

1.—Department of Physics, Akkineni Nageswara Rao College, Gudivada 521 301, India.
2.—Department of Physics, Sri Venkateswara University, Tirupati 517 502, India.
3.—Department of Physics, Government Degree College, Palamaner 517 408, India.
4.—Department of Physics, Gayatri Vidya Parishad College of Engineering (A),
Visakhapatnam 530 048, India. 5.—e-mail: praveena@gvpce.ac.in

Strontium phosphate glasses with various concentrations of Nd₂O₃ have been prepared by melt quenching method. Absorption and photoluminescence spectra and lifetime measurements have been carried out to obtain the optical properties of these glasses. From the absorption spectrum, intensity and radiative parameters have been evaluated using Judd–Ofelt analysis. Near-infrared photoluminescence spectra consist of three bands centered at 875 nm, 1056 nm and 1327 nm, among which the highest intensity has been noticed for the band at 1056 nm that corresponds to the ⁴F_{3/2} → ⁴F_{11/2} transition of Nd³⁺ ion. Laser parameters such as branching ratio, band width, stimulated emission cross section and gain bandwidth for the ⁴F_{3/2} → ⁴F_{11/2} transition are found to be 0.52, 28 nm, 2.31 × 10⁻²⁰ cm² and 6.5 × 10⁻²⁶ cm³, respectively. Decay curves of the ⁴F_{3/2} level of Nd³⁺ ions exhibit a single exponential nature at lower concentrations, while they become non-exponential at higher concentrations (≥ 0.1 mol.%) due to non-radiative energy transfer processes. This feature is also associated with shortening of lifetime from 307 μs to 82 μs when the Nd³⁺ ion concentration increases from 0.1 mol.% to 4.0 mol.%. The results have been compared with those of barium and magnesium phosphate glasses and commercial glasses. The results suggest that these glasses have potential applications as infrared laser materials at 1.05 μm.

Key words: Nd³⁺ ion, strontium phosphate glasses, JO parameters, NIR luminescence, laser applications

INTRODUCTION

Trivalent lanthanide (Ln³⁺) ion-doped glasses have attracted much attention as they have potential applications in the fields of plasma display panels, photovoltaics, antibacterial activity, optical detectors, fiber grating, drug carriers, photocatalysis, lasers, fiber amplifiers, waveguides and telecommunications.^{1–3} Owing to the optical properties of the Ln³⁺-doped glasses and with the prompt evolution of the diode-pumped solid-state lasers,

investigation on newly developed laser glasses has gained more attention.^{4,5} Among the various Ln³⁺ ions, Nd³⁺ ion is one of the important and most extensively studied ions for near-infrared (NIR) lasers as it emits very useful wavelengths at 880 nm, 1050 nm, 1350 nm and 1800 nm corresponding to ⁴F_{3/2} → ⁴I_{J/2} (*J* = 9, 11, 13 and 15) transitions, respectively. Out of these four transitions, the ⁴F_{3/2} → ⁴I_{11/2} transition at 1050 nm is the most intense one and has several practical applications. The other laser transitions at 800 nm and 1350 nm are being used in diode lasers and telecommunications, respectively.

On the other hand, petawatt (PW)-scale laser facilities based on ultrahigh-intensity lasers have

(Received February 21, 2020; accepted July 31, 2020)

been fabricated around the world in the last few decades.^{6,7} Nd³⁺-doped glass amplifiers are being used to develop these ultrahigh-intensity lasers.⁸ But the commercially available Nd³⁺-doped silicate and phosphate^{9,10} glasses and even the hybrid glass structure¹¹ are unable to shorten the pulse duration and enhance the peak power of the laser pulses to the required level (exawatt-level pulse or 10–15 PW in a single beam) due to their narrow emission bandwidth (around 25 nm)¹² and short fluorescence lifetime. Hence, it is important to develop the new Nd laser glasses that can give an ultra-wide emission band for constructing high-energy ultrashort pulse lasers. Therefore, selecting a suitable glass host as an active medium for the laser action is also an important criterion to achieve the desired characteristics, including minimum optical losses, high gain and high-energy storage capability. These characteristics in turn depend on the stimulated emission cross section, band width, coupling efficiency of the pump source and lifetime of the excited level.^{13,14}

Of all the optical glasses, phosphate glasses have been extensively studied due to their exclusive advantages such as low melting point, low dispersion, low softening temperatures, high mechanical, thermal and electrochemical stability, high refractive index, high ionic conductivity, high solubility of Ln³⁺ ions resulting in less clustering, extensive transparency in the ultraviolet-infrared (UV-IR) spectral region, etc.^{15,16} Nevertheless, the hygroscopic nature and poor chemical durability of these glasses are the drawbacks for their practical application as laser gain media. Addition of alkaline earth metals (Mg, Ca, Sr and Ba) to the phosphate glass as a network modifier leads to a disruption of the glass network and enhances the creation of non-bridging oxygen (NBO) defects.¹⁷

In view of the above merits, the authors systematically prepared the Nd³⁺-doped phosphate glasses modified by BaO, MgO and SrO individually as a single modifier. Spectroscopic investigations of Nd³⁺-doped BaO (P₂O₅-BaO-Nd₂O₃: PBN) and MgO (P₂O₅-MgO-Nd₂O₃: PMN) modified phosphate glasses have already been reported earlier^{18,19} by our group. In this report, absorption and NIR photoluminescence properties of Nd³⁺-doped SrO (P₂O₅-SrO-Nd₂O₃: PSN) modified phosphate glasses are studied, and the results obtained are compared with those of BaO- and MgO-modified glasses along with the other reported SrO-based Nd³⁺-doped phosphate glasses as well as commercial glasses. The effect of concentration on the photoluminescence properties of these glasses has also been presented. For the past decade, phosphate glasses with two or three modifiers have been studied so far. To the best of the authors' knowledge, the photoluminescence properties of phosphate glasses with a single modifier (i.e. SrO) have not been reported so far. Therefore, the present work can provide the basis to understand the fundamentals that underlie

the composition dependent luminescence properties of phosphate glasses.

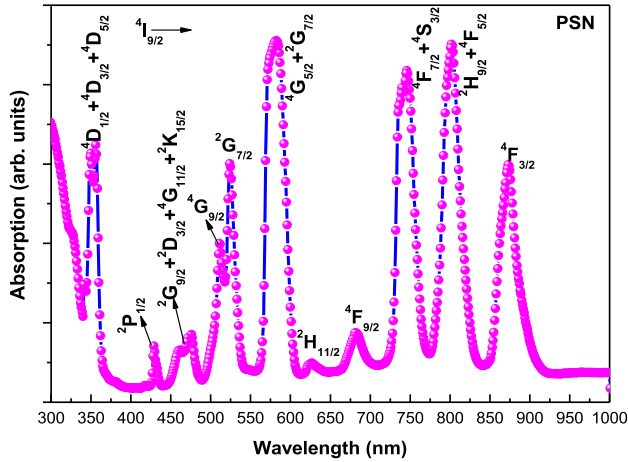
EXPERIMENTAL TECHNIQUES

Nd³⁺-doped strontium phosphate (PSN) glasses of composition (50 - x/2) P₂O₅ + (50 - x/2) SrO + x Nd₂O₃ (where x = 0.05 mol.%, 0.1 mol.%, 0.5 mol.%, 1.0 mol.%, 2.0 mol.%, 3.0 mol.% and 4.0 mol.%) were prepared by the melt quenching method following the procedure described in our earlier paper.¹⁸ High-purity chemicals of strontium metaphosphate (Sr(PO₃)₂) and neodymium oxide (Nd₂O₃) from Sigma-Aldrich were taken as initial materials. Prepared glass samples were labeled as PSN005, PSN01, PSN05, PSN10, PSN20, PSN30 and PSN40 for 0.05 mol.%, 0.1 mol.%, 0.5 mol.%, 1.0 mol.%, 2.0 mol.%, 3.0 mol.% and 4.0 mol.% concentration of Nd₂O₃, respectively.

Refractive index was measured with an Abbe refractometer at the wavelength of 589.3 nm. Archimedes' drainage method was used to obtain the density of glass samples using distilled water. The density and concentration of Nd³⁺ ion in the PSN10 glass were found to be 3.298 g cm⁻³ and 0.2641 × 10²⁰ ions cm⁻³, respectively. The UV-visible-NIR absorption spectrum of the PSN10 glass was recorded on a Perkin-Elmer Lambda 950 UV/VIS/NIR spectrophotometer with a spectral resolution of ± 1 nm. An Edinburgh UV-VIS-NIR (FLS 980) spectrophotometer equipped with an 808-nm pulsed laser diode (excitation source) was used to record NIR luminescence spectra and decay curves. All these measurements were made at room temperature.

RESULTS AND DISCUSSION

The refractive index of the PSN10 glass is found to be 1.586 which is slightly lower than 1.0 mol.% of Nd₂O₃-doped BaO (PBN10) (1.598)¹⁸ and higher than MgO-modified (PMN10) (1.581)¹⁹ phosphate glasses. It is observed that the refractive index increases with increase in cationic radius of the network modifier element. It is also well known that the NBO with increasing polarizability can enhance the index of refraction in the glass host. Therefore, the low refractive index shows the presence of a relatively low concentration of NBOs in the present PSN10 glass compared to that of PBN10 glass.¹⁸ Optical absorption spectrum of Nd³⁺-doped PSN10 glass is depicted in Fig. 1. All the absorption bands fall in the visible-NIR region, whereas the absorption edge is in the ultraviolet (UV) region (~ 300 nm). No sharp absorption edge is observed, which is evidence for the glassy state. It can be seen that the Stark structure is weakly resolved in the glasses due to the inhomogeneous broadening, and hence most of the transitions often overlap in the spectrum. Upon excitation, Nd³⁺ ions are pumped from the ground state (⁴I_{9/2}) to the different excited levels of 4f³-4f³ electronic transitions. Eleven bands


 Fig. 1. Optical absorption spectrum of Nd³⁺-doped PSN10 glass.

centered at 352 nm, 430 nm, 468 nm, 510 nm, 524 nm, 581 nm, 626 nm, 682 nm, 745 nm, 802 nm and 874 nm are observed in the absorption spectrum, which are assigned to the ${}^4I_{9/2} \rightarrow ({}^4D_{1/2} + {}^4D_{3/2} + {}^4D_{5/2})$, $({}^2P_{1/2} + {}^2D_{5/2})$, $({}^2G_{9/2} + {}^2D_{3/2} + {}^4G_{11/2} + {}^2K_{15/2})$, ${}^4G_{9/2}$, ${}^2G_{7/2}$, $({}^4G_{5/2} + {}^2G_{7/2})$, ${}^2H_{11/2}$, ${}^2F_{9/2}$, $({}^4F_{7/2} + {}^4S_{3/2})$, $({}^4F_{5/2} + {}^2H_{9/2})$ and ${}^4F_{3/2}$ transitions, respectively. The absorption spectrum is similar to those of the reported Nd³⁺ glasses,^{9–12,18,19} except for small changes in their relative peak positions, intensities and broadening due to changes in the ligand field around the Nd³⁺ ions in different glass matrices. The Nd³⁺–ligand bond influences the position of the absorption band due to the nephelauxetic effect. The nephelauxetic ratio (β) and bonding parameter (δ) are calculated using the following expressions:^{20,21}

$$\beta = \frac{\nu_c}{\nu_a} \quad (1)$$

$$\delta = \left[\frac{1 - \bar{\beta}}{\bar{\beta}} \times 100 \right] \quad (2)$$

where ' ν_c ' and ' ν_a ' are the energies of the respective transitions in the glass system and aqua solution. The assignment of energy levels of the Nd³⁺ ions in the PSN10 glass and the aquo-ion are made using the reports of Carnall et al.²² as these values are host-independent. The $\bar{\beta}$ is the average of all the β values of the observed transitions in the absorption spectrum. Positive or negative values of δ specify the covalent or ionic nature of the Nd³⁺–O bond, respectively.²³ The experimental energies and δ values are given in Table I. A positive value of δ in this PSN10 glass shows that the bonding of Nd³⁺ ions with their surrounding ligand field is covalent. It is noticed that the δ value is lower compared to those of PBN10¹⁸ and PMN10¹⁹ glasses, indicating that Nd³⁺ ions experience relatively weak covalence in the PSN glass and that the covalence is increased in the order of PSN < PBN < PMN.

Among the absorption transitions, ${}^4I_{9/2} \rightarrow ({}^4G_{5/2} + {}^2G_{7/2})$ is the most intense and is hypersensitive transition (HST). Generally, the HST is more sensitive to the chemical surroundings of the Nd³⁺ ion in the glass matrix. This transition normally has higher values of doubly reduced matrix elements and oscillator strengths compared to other transitions. Experimental oscillator strengths (f_{exp}) of various absorption transitions of Nd³⁺ ion in the PSN10 glass are evaluated by integrating each band as given in Ref. 24. Using these f_{exp} values, Judd–Ofelt (JO)^{25,26} analysis has been performed for the PSN10 glass to obtain the calculated oscillator strengths (f_{cal}) and intensity parameters (Ω_λ , $\lambda = 2, 4, 6$) following the least square method.²⁴ The value of root-mean-square deviation [$\sigma(N)$] indicates the quality of the fit. The values of f_{exp} , f_{cal} and $\sigma(N)$ are given in Table I and are compared to those of PMN10¹⁸ and PBN10¹⁹ glasses. From Table I, it is noticed that the value of $\sigma(N)$ is $\pm 0.87 \times 10^{-6}$ which indicates that f_{exp} and f_{cal} are in good agreement. As expected, the oscillator strengths for the HST are high and it is also noticed that these are relatively higher in PBN10¹⁸ and lower in the present PSN10 glasses, suggesting that a relatively lower nonsymmetric electric field component is acting on the Nd³⁺ ions in the PSN glass.

The obtained intensity parameters (Ω_2 , Ω_4 and Ω_6) from JO analysis for the present PSN10 glass are presented in Table II along with the values of other reported Nd³⁺-doped glasses.^{18,19,27–31} Generally, intensity parameters do not vary much as a function of Nd³⁺ ion concentration. Hence, it is usual practice to calculate the intensity parameters for a 1.0 mol.% doped sample (which is the optimum concentration to obtain reasonable intensities for absorption bands of Ln³⁺ ions) and are used to evaluate radiative properties of the emitting levels of Ln³⁺ ions. It is reported that Ω_2 is more sensitive to the ligand field, and, in turn, the composition of the glass and its value is a measure of the amount of covalent bonding between Nd³⁺ ions and surrounding ligands and site symmetry as well.³² As can be seen from Table II, it is observed that the Ω_2 value is decreasing in the order STPN³⁰ > PKSAN²⁷ > PKSAFN²⁷ > PKSABFN²⁷ > PKSFAFN²⁸ > LG-750³¹ > LHG-8³¹ > LG-770³¹ > LHG-80³¹ > PBN¹⁸ > PMN¹⁹ > PCBSN²⁹ > PSN. It is clear that the Ω_2 value in PSN10 glass is lowest compared to those of the glass systems presented in Table II,^{18,19,27–31} suggesting that there is higher symmetry at the Nd³⁺ ion site and weaker covalence of the Nd³⁺–ligand bond. The higher symmetry at the Nd³⁺ ion site (due to the close packing of oxygen atoms around the Nd³⁺ ion) in the PSN10 glass is also evident from the lower values of oscillator strengths. The weaker Nd–O covalence in the PSN10 glass is also consistent with the result obtained from the nephelauxetic effect. Therefore, both JO theory and the nephelauxetic effect indicate that Nd³⁺ ions in the PSN10 glass experience relatively weaker covalence, and both approaches give the

Table I. Experimental energies (E_{exp} , cm^{-1}), experimental (f_{exp}) and calculated (f_{cal}) oscillator strengths ($\times 10^{-6}$) and bonding parameter (δ) of PSN10, PMN10 and PBN10 glasses

Transition	Energy	Oscillator strengths					
		PSN10		PMN10		PBN10	
	E_{exp}	f_{exp}	f_{cal}	f_{exp}	f_{cal}	f_{exp}	f_{cal}
${}^4\text{I}_{9/2} \rightarrow$							
${}^4\text{F}_{3/2}$	11,456	2.56	1.85	1.54	1.93	2.20	2.67
${}^4\text{F}_{5/2} + {}^2\text{H}_{9/2}$	12,469	4.43	4.74	5.89	5.82	7.34	6.79
${}^4\text{F}_{7/2} + {}^4\text{S}_{3/2}$	13,405	4.51	4.46	5.78	5.96	5.85	6.34
${}^4\text{F}_{9/2}$	14,663	0.51	0.36	0.63	0.46	0.43	0.51
${}^2\text{H}_{11/2}$	15,974	0.15	0.10	0.16	0.13	0.09	0.14
${}^4\text{G}_{5/2} + {}^2\text{G}_{7/2}$	17,212	9.55	9.61	13.20	13.29	16.30	16.34
${}^4\text{G}_{7/2}$	19,084	3.54	2.39	4.48	2.74	4.22	3.58
${}^4\text{G}_{9/2}$	19,531	3.11	1.08	3.01	1.23	2.58	1.57
${}^4\text{G}_{11/2} + {}^2\text{D}_{3/2} + {}^2\text{G}_{9/2} + {}^2\text{K}_{15/2}$	21,008	1.69	0.89	1.30	1.03	1.74	1.29
${}^2\text{P}_{1/2} + {}^2\text{D}_{5/2}$	23,310	0.38	0.50	0.46	0.49	0.74	0.72
${}^4\text{D}_{1/2} + {}^4\text{D}_{3/2} + {}^4\text{D}_{5/2}$	28,090	7.77	9.05	8.56	9.10	12.68	13.07
$\sigma(N)^a$ ($\times 10^{-6}$)		± 0.87 (11)		± 0.79 (11)		± 0.48 (11)	
δ		0.3714		0.6036		0.4016	

$\sigma(N)$ is the root mean square (r.m.s) deviation between experimental and calculated energy levels, and N is the number of levels considered in the fitting.

Table II. Comparison of JO parameters (Ω_i , $\times 10^{-20} \text{ cm}^2$), spectroscopic quality factor (χ), radiative (τ_R , μs), experimental (τ_{exp} , μs) lifetimes, quantum efficiency (η , %), bandwidth ($\Delta\lambda_{\text{eff}}$, nm), emission cross section [$\sigma(\lambda_p)$, $\times 10^{-20} \text{ cm}^2$], gain band width [$\Delta\lambda_{\text{eff}} \times \sigma(\lambda_p)$, $\times 10^{-26} \text{ cm}^3$] in various Nd^{3+} -doped phosphate glasses

Glass	Composition	Ω_2	Ω_4	Ω_6	χ	τ_R	τ_{exp}	η	$\Delta\lambda_{\text{eff}}$	$\sigma(\lambda_p)$	$\Delta\lambda_{\text{eff}} \times \sigma(\lambda_p)$	References
PSN	P_2O_5 , SrO, Nd_2O_3	1.16	3.78	3.00	1.25	451	256	57	28.2	2.31	6.5	Present work
PBN	P_2O_5 , BaO, Nd_2O_3	2.62	5.47	4.24	1.29	331	180	54	24.0	2.79	6.7	18
PMN	P_2O_5 , MgO, Nd_2O_3	2.55	3.74	4.12	0.91	394	232	59	25.0	3.26	8.2	19
PKSAN	P_2O_5 , K_2O , SrO, Al_2O_3 , Nd_2O_3	6.74	3.86	6.35	0.61	319	172	54	27.95	4.05	11.3	27
PKSFAN	P_2O_5 , K_2O , SrO, SrF, Al_2O_3 , Nd_2O_3	5.24	4.30	5.81	0.74	326	211	65	32.6	3.29	10.7	28
PKSAFN	P_2O_5 , K_2O , SrO, Al_2O_3 , Al_2F_3 , Nd_2O_3	6.63	5.07	5.98	0.85	290	188	65	23.7	5.08	12.0	27
PKSABFN	P_2O_5 , K_2O , SrO, Al_2O_3 , BaF, Nd_2O_3	6.50	4.64	5.99	0.77	306	194	63	23.5	4.72	11.1	27
PCBSN	P_2O_5 , CaO, BaO, SrO, Nd_2O_3	2.17	2.46	3.07	0.80	354	284	80	27.5	3.90	10.7	29
STPN	SrO, TiO_2 , P_2O_5 , Nd_2O_3	7.75	4.74	6.05	0.78	282	238	84	26.0	4.89	12.7	30
LHG-80	—	3.6	5.0	5.5	0.91	326	—	—	23.9	4.20	10.0	31
LHG-8	P_2O_5 , Al_2O_3 , K_2O , BaO	4.4	5.1	5.6	0.91	351	—	—	26.5	3.60	9.5	31
LG-770	P_2O_5 , Al_2O_3 , K_2O , MgO	4.3	5.0	5.6	0.89	349	—	—	25.4	3.90	9.9	31
LG-750	P_2O_5 , Al_2O_3 , K_2O , BaO	4.6	4.8	5.6	0.86	367	—	—	25.3	3.70	9.3	31

same conclusion. Chanthima et al.³³ also observed that the asymmetric nature around the Ln^{3+} ion is more in MgO-modified phosphate glass than that of the SrO-modified glass. Further, from Table II, it is also observed that with the addition of K_2O , Al_2O_3 ,

fluorine content^{27,28} and TiO_2 ³⁰ to the phosphate glasses, the covalence of the Nd–O bond increases drastically.

It is also well known that Ω_4 depends on the long-range effects and is related to the bulk properties of

glass, and Ω_6 is related to the rigidity of the glass host, which are influenced by the vibronic transitions of the Ln³⁺ ions bound to the ligand atoms. As can be seen from Table II, the Ω_6 value is found to be lowest in the PSN10 glass compared to those of the other reported glasses, indicating that PSN glass has a less rigid nature. Generally, in the case of Nd³⁺ ions, a higher value of Ω_4 parameter favors an intense ${}^4F_{3/2} \rightarrow {}^4I_{9/2}$ transition, while the Ω_6 parameter improves intensity of the ${}^4F_{3/2} \rightarrow {}^4I_{11/2}$ transition. In fact, the ratio of Ω_4/Ω_6 , called spectroscopic quality factor (χ), is a very important parameter, and it provides the information about the means through which ${}^4F_{3/2}$ level of Nd³⁺ ion can relax to the ground state. In order to get the highest luminescence for ${}^4F_{3/2} \rightarrow {}^4I_{11/2}$ transition, Ω_6 should be slightly greater than Ω_4 . In the PSN10 glass, the χ value is found to be 1.25 which falls within the normal range of 0.2–1.5. As can be seen from Table II, $\Omega_6 > \Omega_4$ for all the reported glasses, except for PSN10 and PBN10¹⁸ glasses; consequently, the χ value is greater than that for the PSN10 and PBN10 glasses. This result is similar to those found in borate,³⁴ LiPbAlB,³⁵ NbI,³⁶ tellurite,³⁷ fluorophosphate³⁸ and ZBSN4³⁹ glasses. Hence, in these glasses, the ${}^4F_{3/2} \rightarrow {}^4I_{9/2}$ transition also plays an important role in relaxing the ${}^4F_{3/2}$ level. Moreover, this high-intensity laser at 875 nm corresponding to the ${}^4F_{3/2} \rightarrow {}^4I_{9/2}$ transition is also useful to produce blue light-emitting devices by the monolithic integration of laser emission.⁴⁰

Further, the JO intensity parameters (Ω_λ) are used to evaluate the radiative properties like radiative transition probability (A_R), branching ratio (β_R) and radiative lifetime (τ_R) for the ${}^4F_{3/2} \rightarrow {}^4I_{9/2,11/2,13/2}$ transitions of Nd³⁺ ion in the PSN10 glass. Radiative lifetime for the ${}^4F_{3/2}$ level of Nd³⁺ ion in the PSN10 glass is found to be 451 μ s which is the highest value compared to those of the other reported glasses presented in Table II. This indicates that the excited level slowly depopulates in the PSN10 glass, which favors the population inversion and, consequently, stimulated emission.

NIR luminescence spectra of PSN glasses were obtained by exciting the samples with an 808-nm laser and are shown in Fig. 2. A partial energy level diagram of the Nd³⁺ ions is shown in Fig. 3 which explains the mechanism involved in NIR luminescence in the Nd³⁺-doped PSN glasses. When excited at 808 nm, initially, the Nd³⁺ ions were pumped to the ${}^4F_{9/2}$ level, from which they made fast non-radiative transition and reached a ${}^4F_{3/2}$ metastable state, as shown in Fig. 3. Thereafter, they made radiative transitions to lower-lying energy levels whose wavelength lies in NIR region. NIR luminescence spectra consisting of three bands at 875 nm, 1056 nm and 1327 nm correspond to the ${}^4F_{3/2} \rightarrow {}^4I_{J/2}$ ($J = 9, 11$ and 13) transitions, respectively. Among them, the ${}^4F_{3/2} \rightarrow {}^4I_{11/2}$ transition at 1056 nm is the most intense and prominent one which has many practical applications as a four-

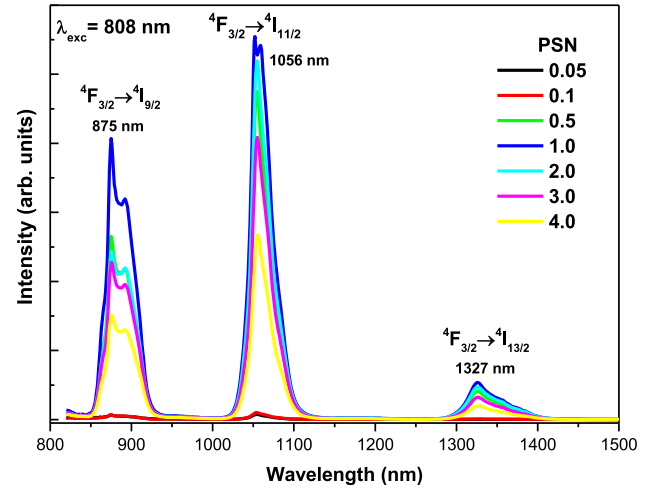


Fig. 2. NIR luminescence spectra of Nd³⁺-doped PSN glasses under 808-nm excitation.

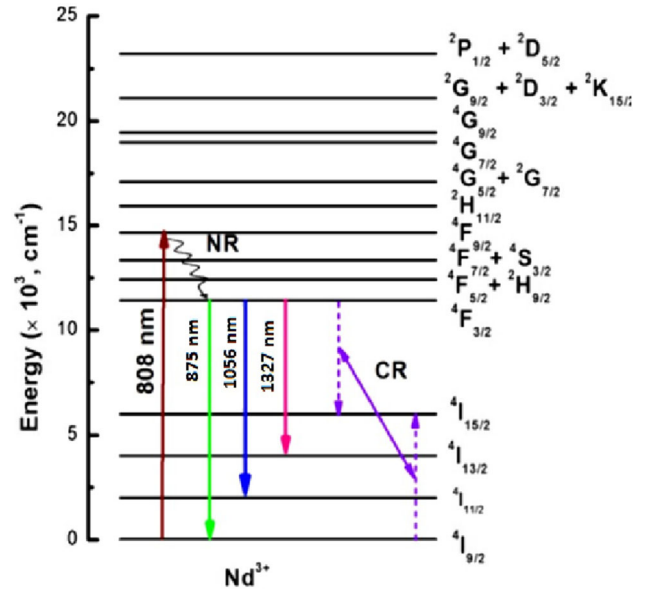


Fig. 3. Partial energy level diagram of Nd³⁺ ions in PSN glasses.

level laser system. The emission band at 875 nm split into two bands, which describes the specificity of the glass host. Intensities of all three transitions with respect to Nd³⁺ ion concentration are depicted in Fig. 4a. As can be seen, at very low concentrations (from 0.05 mol.% to 0.1 mol.%), no change is observed in the intensity, but the intensities of all three transitions increase rapidly from 0.1 mol.% to 1.0 mol.% and then decreases with increase in concentration. This luminescence quenching behavior at higher concentrations above 1.0 mol.% is due to the enhanced energy transfer between the neighboring Nd³⁺ ions via cross-relaxation channels, through ${}^4F_{3/2} + {}^4I_{9/2} \rightarrow {}^4I_{15/2} + {}^4I_{15/2}$ (Fig. 3).⁴¹ Therefore, 1.0 mol.% is the optimum concentration in the present Nd³⁺: PSN glasses. Further, the

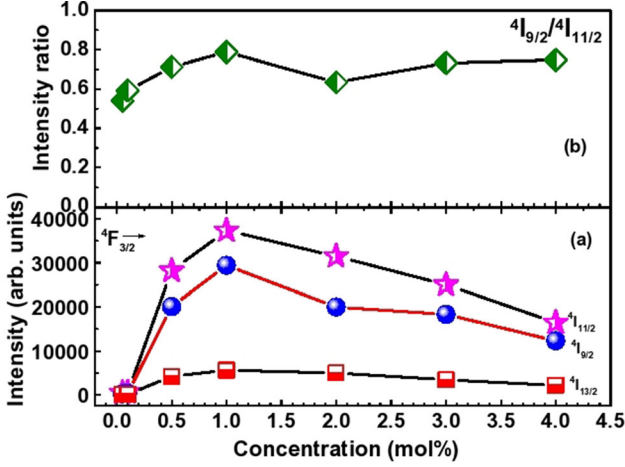


Fig. 4. (a) Variation of peak intensity of $4F_{3/2} \rightarrow 4I_{9/2}$, $4I_{11/2}$ and $4I_{13/2}$ transitions and (b) relative intensity ratio of $4F_{3/2} \rightarrow 4I_{9/2}$ and $4F_{3/2} \rightarrow 4I_{11/2}$ transitions in Nd^{3+} -doped PSN glasses as a function of concentration.

Table III. Emission peak position (λ_p , nm), effective bandwidth ($\Delta\lambda_{eff}$, nm), radiative transition probability (A_R , s^{-1}), peak stimulated emission cross section ($\sigma(\lambda_p)$, $\times 10^{-20}$ cm^2) and experimental and calculated branching ratios (β_R) for $4F_{3/2} \rightarrow 4I_J$ ($J = 9/2, 11/2$ and $13/2$) transitions in PSN10 glass

Transition $4F_{3/2} \rightarrow$	λ_p	$\Delta\lambda_{eff}$	A_R	$\sigma(\lambda_p)$	β_R	
					Exp.	Cal.
$4I_{9/2}$	875	36.26	1012	0.86	0.40	0.46
$4I_{11/2}$	1056	28.21	1010	2.31	0.52	0.46
$4I_{13/2}$	1327	46.74	182	0.63	0.08	0.08

relative intensity ratio of $4F_{3/2} \rightarrow 4I_{9/2}/4F_{3/2} \rightarrow 4I_{11/2}$ transitions is also high at 1.0 mol.% concentration of Nd^{3+} ions, as shown in Fig. 4b.

From the NIR luminescence spectra, effective bandwidth ($\Delta\lambda_{eff}$, nm), radiative transition probability (A_R , s^{-1}), peak stimulated emission cross section [$\sigma(\lambda_p)$, $\times 10^{-20}$ cm^2] and experimental branching ratio (β_R) for $4F_{3/2} \rightarrow 4I_{J/2}$ ($J = 9, 11$ and 13) transitions in PSN10 glass are evaluated and are given in Table III. As can be seen, radiative transition probabilities for both $4F_{3/2} \rightarrow 4I_{9/2}$ and $4I_{11/2}$ transitions are more or less similar, which indicates that the $4F_{3/2} \rightarrow 4I_{9/2}$ transition is competing with the $4F_{3/2} \rightarrow 4I_{11/2}$ transition in the PSN10 glasses, as discussed above. Another essential parameter that characterizes the power of the laser transition is the branching ratio. In Table III, the experimental β_R values are obtained from the ratio of area under the corresponding emission band and total integrated area of all the emission bands (Fig. 2), while the calculated β_R values are obtained from the JO analysis. It is noticed that the

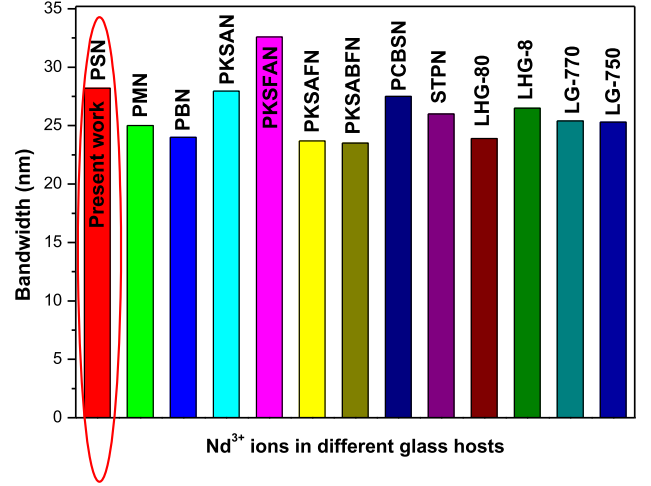


Fig. 5. Bandwidth (nm) in various Nd^{3+} -doped phosphate glasses.

experimental and calculated β_R values are in good agreement. It is observed from the literature that the β_R values for $4I_{9/2,11/2,13/2}$ levels of Nd^{3+} ion in many glasses^{42–44} are approximately in the ratio of 35:55:10, respectively. In the present case, calculated β_R values are in the ratio of 46:46:8 (Table III) as observed in the case of lanthanum sodium zinc tellurite glass.⁴⁵ This is also evident from the values of χ and A_R . However, experimental β_R values are in the ratio of 40:52:8 indicating that the $4F_{3/2} \rightarrow 4I_{11/2}$ transition of Nd^{3+} ion in PSN glass is dominant and is more efficient laser transition than the other two transitions. Furthermore, experimental β_R values (hence the intensity of emission bands) varied marginally in the PBN10,¹⁸ PMN10¹⁹ and PSN10 glasses. However, the β_R value for $4F_{3/2} \rightarrow 4I_{9/2}$ transition is slightly decreased in the order of PMN > PSN > PBN, while it is increased in the order of PMN < PSN < PBN for the $4F_{3/2} \rightarrow 4I_{11/2}$ transition of Nd^{3+} ion. This trend indicates that with increasing cationic radius of the network modifier ions ($Mg^{2+} < Sr^{2+} < Ba^{2+}$), the intensity of $4F_{3/2} \rightarrow 4I_{11/2}$ transition increases. This may be due to greater depolymerization of BaO network modifier oxide.⁴⁶

A low value of $\Delta\lambda_{eff}$ and high value of $\sigma(\lambda_p)$ are preferable for an efficient laser transition. In the present case, lower $\Delta\lambda_{eff}$ and higher $\sigma(\lambda_p)$ values for the $4F_{3/2} \rightarrow 4I_{11/2}$ transition of Nd^{3+} ion in PSN10 glass compared to other two transitions infers that $4F_{3/2} \rightarrow 4I_{11/2}$ transition is a sharp and efficient laser transition. Therefore, based on the above observations, the potential laser transition at 1056 nm in the Nd^{3+} -doped PSN glass can be used for low-threshold and high-gain applications. The $\Delta\lambda_{eff}$ and $\sigma(\lambda_p)$ values for $4F_{3/2} \rightarrow 4I_{11/2}$ transition of Nd^{3+} ion in PSN10 glass are compared with those reported for the other glasses^{18,19,27–31} in Table II. But for the high-energy ultrashort pulse lasers, high radiative lifetime and emission bandwidth values are required. It is observed that the value

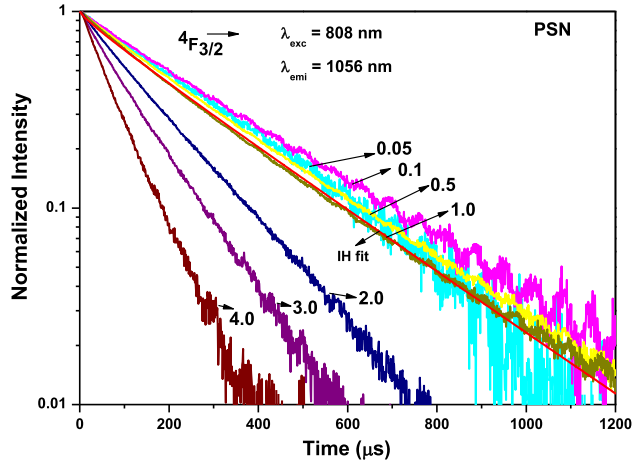


Fig. 6. Decay curves of the ${}^4F_{3/2}$ level for different concentrations of Nd³⁺ ions in PSN glasses under 808-nm excitation, monitoring the emission at 1056 nm. Inokuti–Hirayama (IH) model fit for 1.0 mol.% decay curve is also shown.

of $\Delta\lambda_{\text{eff}}$ is slightly higher in the PSN glass compared to those of other glasses, including commercial glasses except for PKSFAN glass²⁸ (see Fig. 5). Hence, based on the higher radiative lifetime and emission bandwidth values, the present PSN glasses doped with Nd³⁺ ions can find application as high-energy ultrashort pulse laser material. However, the value of $\sigma(\lambda_p)$ for the ${}^4F_{3/2} \rightarrow {}^4I_{11/2}$ transition is found to be lowest in the PSN glass compared to those of other glasses listed in Table II. This could be due to the slightly higher value of $\Delta\lambda_{\text{eff}}$ in the PSN glass. However, the magnitude of $\sigma(\lambda_p)$ is found to be higher in the PSN glass than that of barium fluorophosphate,⁴⁷ phosphate,⁴⁸ LG-650,⁴⁸ L-41,⁴⁸ lead fluorosilicate⁴⁹ and NaF-Na₂O-B₂O₃⁵⁰ glasses, indicating the importance of PSN glass as a potential laser host material. Further, the product of $\Delta\lambda_{\text{eff}} \times \sigma(\lambda_p)$, known as gain bandwidth, is an essential parameter for the design of optical amplifiers. The gain bandwidth is found to be 6.5×10^{-26} cm³ for the ${}^4F_{3/2} \rightarrow {}^4I_{11/2}$ transition of Nd³⁺ ion in the present PSN10 glass. The gain bandwidth is increasing in the order of PSN < PBN < PMN glasses. Further, it is observed that addition of TiO₂, K₂O, Al₂O₃ and AlF₃ modifiers^{27–30} to the strontium phosphate glass greatly enhances the gain bandwidth. Therefore, the present glass forms the basis to understand the modifier effect on the gain bandwidth which will help to improve the function of optical amplifiers. The gain band width value is higher in PSN10 glass than those reported for bismuth borate,⁵¹ fluoroborate⁵² and zinc phosphate⁵³ glasses, indicating that the present PSN glasses can also find application in optical amplifiers.

In order to get more quantitative information on luminescence quenching behavior, the decay curves for the ${}^4F_{3/2}$ level of Nd³⁺ ion in PSN glasses are measured. Figure 6 shows the decay curves of the ${}^4F_{3/2} \rightarrow {}^4I_{11/2}$ transition under 808-nm excitation.

As can be seen, the decay curves are single exponential at lower concentrations up to 0.1 mol.% and turn into non-exponential for higher concentrations of Nd³⁺ ions. The non-exponential decay curves are well fitted to the expression⁵⁴ (see the supplementary Figures S1 to S6):

$$I(t) = A_1 \exp\left(-\frac{t}{\tau_1}\right) + A_2 \exp\left(-\frac{t}{\tau_2}\right) \quad (3)$$

where A_1 and A_2 are constants; τ_1 and τ_2 are extracted from the fitted curves which represent the fast and slow components of decay and are attributed to the radiative and the migration stages of emission, respectively. Therefore, the experimental (τ_{exp}) or average (τ_{avg}) lifetimes of the ${}^4F_{3/2}$ level in these glasses are computed by using the following expression and are presented in Table IV.

$$\tau_{\text{avg}} = \frac{A_1 \tau_1^2 + A_2 \tau_2^2}{A_1 \tau_1 + A_2 \tau_2} \quad (4)$$

As can be seen from Table IV, the experimental lifetimes of the ${}^4F_{3/2}$ level initially increases from 0.05 mol.% to 0.1 mol.% of Nd³⁺ ions and then decreases for higher concentrations. This initial rise and then fall in lifetimes with increasing concentration was also observed for tellurite⁵⁵ and PKBA⁵⁶ glasses. This could be due to either radiative trapping⁵⁵ or differential site occupancy. Variations in the ligand fields around the Nd³⁺ ion may give raise to differences in the lifetimes. The shortening of lifetimes at higher concentrations could be due to the concentration quenching between Nd³⁺ ions. The τ_{exp} values of PSN glasses are compared with those of PBN¹⁸ and PMN¹⁹ glasses and are given in Table IV and shown in Fig. 7. It is also noticed that with increasing concentration, the lifetime values are relatively slowly decreasing in PSN glass compared to those of PBN¹⁸ and PMN¹⁹ glasses. This could be due to the higher symmetry and weaker covalence experienced by the Nd³⁺ ion in the PSN glass compared to PMN and PBN glasses. The τ_{exp} value is found to be higher in PSN10 glass compared to those of other glasses shown in Table II except for PCBSN.²⁹ It is observed that addition of K₂O, Al₂O₃ and fluorine content^{27,28} may lower the lifetime, while CaO + BaO²⁹ and TiO₂³⁰ may enhance the lifetime in the SrO-based phosphate glasses.

On the other hand, in PSN10 glass, considerable variation between τ_{exp} and τ_R for the ${}^4F_{3/2}$ level has been observed, which emphasizes that some non-radiative energy transfer processes (W_{nr}) are involved. W_{nr} values in the PSN glasses are presented in Table IV, which are evaluated using the following expression:

$$W_{\text{nr}} = \left(\frac{1}{\tau_{\text{exp}}} - \frac{1}{\tau_R} \right) \quad (5)$$

Table IV. Lifetime (τ_{exp} , μs), non-radiative energy transfer rate (W_{nr} , μs^{-1}), quantum efficiency (η , %), energy transfer parameter (Q), critical distance (R_o , \AA) and donor-acceptor interaction parameter (C_{DA} , $\times 10^{-40} \text{ cm}^6 \text{ s}^{-1}$) of Nd^{3+} -doped PSN glasses

Concentration		τ_{exp}					W_{nr}	η (%)	Q	R_o	C_{DA}
(mol.%)	(ions cc^{-1})	PSN	PMN	PBN							
0.05	0.069	273	346	260	1.652	61	–	–	–	–	
0.1	0.147	307	315	235	1.469	68	0.047	7.55	6.03		
0.5	0.682	282	300	224	1.599	63	0.157	6.78	3.16		
1.0	1.306	256	232	180	1.762	57	0.250	6.38	2.20		
2.0	2.597	167	170	151	2.701	37	0.701	7.14	4.32		
3.0	3.964	124	–	88	3.637	27	1.087	7.18	4.46		
4.0	5.366	82	57	74	5.500	18	1.650	7.46	5.61		

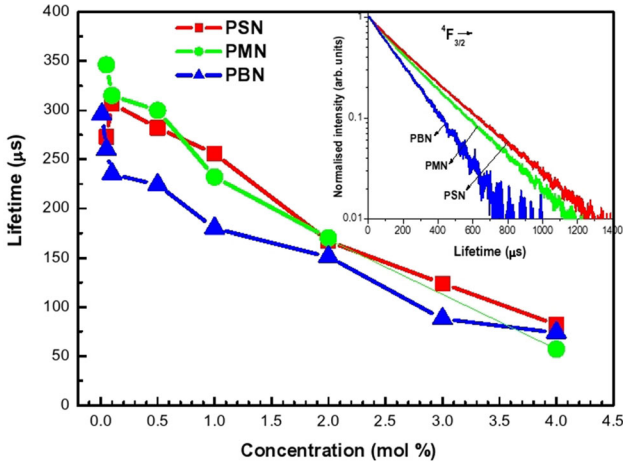


Fig. 7. Variation of lifetime (τ_{exp}) of the ${}^4\text{F}_{3/2}$ level of Nd^{3+} ion in PSN, PMN and PBN glasses. The inset shows the decay profiles of Nd^{3+} ion in PSN10, PMN10 and PBN10 glasses.

As can be seen from Table IV, W_{nr} values are increasing consistently with increase in concentration of Nd^{3+} ions after 0.1 mol.%. It is well known that there are four decay processes, namely multiphonon relaxation (MPR), concentration quenching, energy transfer and presence of OH content, which are responsible for the observed decrease of lifetime through non-radiative energy transfer. It is observed from the literature that the phonon energy of phosphate glass is around 1300 cm^{-1} ⁵⁷, and, hence, four to five phonons are required to overcome the gap between the ${}^4\text{F}_{3/2}$ level and its lower ${}^4\text{I}_{15/2}$ level ($\sim 5250 \text{ cm}^{-1}$). Hence, MPR is one of the processes that contributes to the decrease of lifetime in the present PSN glasses. Concentration quenching is mainly due to the increase in Nd^{3+} ion concentration, which involves two mechanisms: The first one is due to the cross-relaxation where the donor (which is in an excited state) and nearby acceptor (which is in a ground state) exchange energy, and the second one is due to the energy migration between donor to donor and then to traps.

In the present case, the former is playing a dominant role and is evident from the decrease of emission intensities with increasing concentration. Finally, the non-exponential behavior of the decay curves represents the presence of energy transfer. In order to explain the type of energy transfer mechanism, the decay curves are analyzed in the framework of the Inokuti–Hirayama (IH) model following the same procedure given in Ref. 58. The non-exponential decay curves are well-fitted to the IH model for $S = 6$, which confirms the nature of interaction between Nd^{3+} ions is dipole–dipole. The IH fit for the decay curve of 1.0 mol.% is included in Fig. 6. The calculated energy transfer parameter (Q), critical distance (R_o) and donor-to-acceptor energy transfer interaction parameter (C_{DA}) are given in Table IV, which are important to assess the strength of the interaction between donor and acceptor. Generally, with increase in R_o value, Q and C_{DA} parameters will increase. As can be seen from Table IV, the Q value is increasing consistently with increase in Nd^{3+} ion concentration, while the values of R_o and C_{DA} decrease initially up to 2.0 mol.% and then increase for higher concentrations.

Further, in order to determine whether the concentration quenching of lifetime of the ${}^4\text{I}_{15/2}$ level of Nd^{3+} ions in the present PSN glasses is due to a diffusion-limited or fast diffusion process, the decay curves have been analyzed based on the theory developed by Auzel et al.^{59,60} The diffusion-limited process represents strong self-quenching,⁵⁹ whereas the fast diffusion process represents weak self-quenching⁶⁰ between Nd^{3+} ions in the glass host. According to Auzel’s theory, for electric dipole–dipole interaction, the self-quenching by a diffusion-limited process can be calculated using the expression⁵⁹

$$\tau(N) = \frac{\tau_0}{1 + \frac{9}{2\pi} \left(\frac{N}{N_0}\right)^2} \quad (6)$$

and self-quenching by fast diffusion can be calculated by the expression⁶⁰

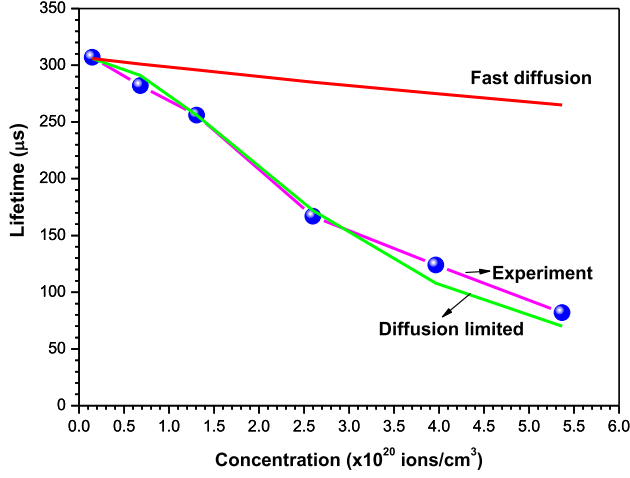


Fig. 8. Quenching of lifetime of the ${}^4F_{3/2}$ level as a function of Nd^{3+} ion concentration in PSN glasses along with the simulated curves using Eqs. 6 and 7.

$$\tau(N) = \frac{\tau_0}{1 + 1.45 \frac{N}{N_c} e^{-\frac{\beta \Delta E}{4}}} \quad (7)$$

where N is the concentration of Nd^{3+} ion, τ_0 is the experimental lifetime at very low concentration, N_o is the critical sensitizer concentration for self-quenching, N_c is the critical concentration for the diffusion step between active ions, β is the exponential parameter for multiphonon-assisted energy transfers in the considered host and ΔE is the energy gap between the ${}^4F_{9/2}$ and ${}^4I_{15/2}$ levels of the Nd^{3+} ion.

In the present study, N_c was taken to be equal to N_o (3.5×10^{20} ions/c.c.), which is calculated from the Eq. 6 for 1.0 mol.% of Nd^{3+} ions by taking $\tau_0 = 307 \mu s$ (experimental lifetime of 0.1 mol.% Nd^{3+} -doped glass). The β value (2.0×10^{-3} cm) was calculated from the equations given in Ref. 61, by taking the values of phonon energy as 1300 cm^{-1} ^{57,58} and the electron phonon coupling constant (g) as 0.054.⁵⁷ By substituting the appropriate values, Eqs. 6 and 7 are used to simulate the lifetimes of the ${}^4F_{3/2}$ level for different Nd^{3+} ion concentrations in the PSN glasses. The results are depicted in Fig. 8. As can be seen from Fig. 8, it is understood that the concentration quenching in the present PSN glasses is purely diffusion-limited up to 2.0 mol.% and then slightly deviated towards fast diffusion for higher Nd^{3+} ion concentrations. This indicates a gradual decrease of the diffusion-limited process and onset of the fast diffusion processes at higher Nd^{3+} ion concentration in the PSN glasses.

Quantum efficiency (η , %) can be known from the ratio of experimental and calculated lifetimes ($= \tau_{\text{exp}}/\tau_R$) which gives the conversion efficiency in laser performance as it is equal to the ratio of number of emitted photons to the number of absorbed photons. The values of η calculated using the above relation are given in Table IV. It is noticed that the magnitude of η is decreasing as a

function of concentration. The η value is found to be lower in the present PSN10 glass than those of glasses that are compared in Table II but higher than those of tellurite,⁶² bismuth borate,^{51,63} fluoroborate,⁵² fluorophosphate,³⁸ lead borate,⁶⁴ BiZn⁶⁵ and borate sodium⁶⁶ glasses. Finally, the important laser parameter, figure of merit (FOM), defined as the product of $\sigma(\lambda_p) \times \tau_{\text{exp}}$, is proportional to the slope efficiency and inversely proportional to the threshold pump power. Hence, a higher value of FOM is required to achieve high gain for a laser material. FOM values vary in the order of PBN ($9.23 \times 10^{-24} \text{ cm}^2 \text{ s}$) < PSN ($10.42 \times 10^{-24} \text{ cm}^2 \text{ s}$) < PMN ($12.84 \times 10^{-24} \text{ cm}^2 \text{ s}$). The FOM value is found to be increasing with decrease in the cationic radius of the network modifier.

CONCLUSIONS

Nd^{3+} -doped strontium phosphate glasses with different concentrations have been prepared by melt quenching method. Absorption and NIR luminescence spectra and lifetime measurements are made to characterize these glasses. JO analysis has been carried out on the 1.0 mol.% of Nd^{3+} -doped PSN glass to derive intensity parameters and in turn to determine radiative properties. Both JO and nephelauxetic parameters show that Nd^{3+} ions experience higher symmetry and weaker covalence in the PSN10 glass. The spectroscopic quality factor is found to lie within the normal range. The values of χ , calculated β_R and A_R reveal that ${}^4F_{3/2} \rightarrow {}^4I_{9/2}$ transition is competing with the ${}^4F_{3/2} \rightarrow {}^4I_{11/2}$ transition of Nd^{3+} ion in the PSN10 glass. A higher value of τ_R for the ${}^4F_{3/2} \rightarrow {}^4I_{11/2}$ transition indicates that the excited level of Nd^{3+} ion slowly depopulates in the PSN10 glass that favors the population inversion.

The NIR luminescence spectra consist of three bands in which the ${}^4F_{3/2} \rightarrow {}^4I_{11/2}$ transition at 1056 nm is the most intense one. Luminescence intensity is found to be higher for the 1.0 mol.% Nd^{3+} -doped PSN glass. Higher values of experimental β_R ($> 50\%$) and $\sigma(\lambda_p)$ and lower value of $\Delta\lambda_{\text{eff}}$ for the ${}^4F_{3/2} \rightarrow {}^4I_{11/2}$ transition compared to other two transitions infer that the ${}^4F_{3/2} \rightarrow {}^4I_{11/2}$ transition of Nd^{3+} ion in PSN10 glass is a sharp and efficient laser transition. The value of $\Delta\lambda_{\text{eff}}$ of the ${}^4F_{3/2} \rightarrow {}^4I_{11/2}$ transition is relatively higher compared to all strontium-based phosphate glasses and also commercial glasses, suggesting the possible application of the present glass in high-energy ultrashort pulse generation. Decay profiles are single exponential at lower concentration and then become non-exponential at higher concentrations accompanied by a decrease in lifetimes. Non-exponential decay curves are analyzed using the IH model, which infers that the energy transfer between Nd^{3+} ions is of a dipole-dipole type. Diffusion-limited processes are responsible for the observed decrease in the lifetimes of the ${}^4F_{3/2}$ level of Nd^{3+} ion in PSN

glass. Higher values of the FOM show better potential of PSN glasses for NIR laser applications.

ACKNOWLEDGMENTS

One of the authors, Praveena, is grateful to the DAE-BRNS, Govt. of India for the sanction of this major research project (No. 2012/20/34/11/BRNS/2997).

CONFLICT OF INTEREST

The authors declare that they have no conflict of interest.

ELECTRONIC SUPPLEMENTARY MATERIAL

The online version of this article (<https://doi.org/10.1007/s11664-020-08383-5>) contains supplementary material, which is available to authorized users.

REFERENCES

1. A.A. Menazea, A.M. Abdelghany, N.A. Hakeem, W.H. Osman, and F.H. Abd El-Kader, *J. Electron. Mater.* 49, 826 (2020).
2. S. Gopi, P. Remya Mohan, E. Sreeja, N.V. Unnikrishnan, C. Joseph, and P.R. Biju, *J. Electron. Mater.* 48, 4300 (2019).
3. D. Van Hau, D.T.T. Nhan, N. Van Duc, V.P. Tuyen, T.-D. Nguyen, T. Thai Hoa, and N. Duc Cuong, *J. Electron. Mater.* 48, 329 (2019).
4. M.M. Ismail, I.K. Batisha, L. Zur, A. Chiasera, M. Ferrari, and A. Lukowiak, *Opt. Mater.* 99, 109591 (2020).
5. M. Soharab, I. Bhaumik, R. Bhatt, A. Saxena, S. Khan, and A.K. Karnal, *Opt. Mater.* 92, 379 (2019).
6. C. Danson, D. Hillier, N. Hopps, and D. Neely, *High Power Laser Sci. Eng.* 3, e3 (2015).
7. V. Bagnoud and F. Wagner, *High Power Laser Sci. Eng.* 4, e39 (2016).
8. A.A. Kuzmin, E.A. Khazanov, and A.A. Shaykin, *Opt. Express* 19, 14223 (2011).
9. D.F. de Sousa, L.A.O. Nunes, J.H. Rohling, and M.L. Baesso, *Appl. Phys. B Lasers Opt.* 77, 59 (2003).
10. L. Hu, D. He, H. Chen, X. Wang, T. Meng, L. Wen, J. Hu, Y. Xu, S. Li, Y. Chen, W. Chen, S. Chen, J. Tang, and B. Wang, *Opt. Mater.* 63, 213 (2017).
11. G.R. Hays, E.W. Gaul, M.D. Martinez, and T. Ditmire, *Appl. Opt.* 46, 4813 (2007).
12. J.P. Zou, C. Le Blanc, D.N. Papadopoulos, G. Chériaux, P. Georges, G. Mennerat, F. Druon, L. Lecherbourg, A. Pellegrina, P. Ramirez, F. Giambrodo, A. Fréneaux, F. Leconte, D. Badarau, J.M. Boudenne, D. Fournet, T. Valloton, J.L. Paillard, J.L. Veray, M. Pina, P. Monot, J.P. Chambaret, P. Martin, F. Mathieu, P. Audebert, and F. Amiranoff, *High Power Laser Sci. Eng.* 3, e2 (2015).
13. S. Surendra Babu, R. Rajeswari, K. Jang, E.J. Cho, K.H. Jang, H.J. Seo, and C.K. Jayasankar, *J. Lumin.* 130, 1021 (2010).
14. C. Tian, X. Chen, and Y. Shuibao, *Solid State Sci.* 48, 171 (2015).
15. R.O. Omrani, S. Krimi, J.J. Videau, I. Khattech, A. El Jaouli, and M. Jemal, *J. Non Cryst. Solids* 390, 5 (2014).
16. A. Jha, B. Richards, G. Jose, T.T. Fernandez, P. Joshi, X. Jiang, and J. Lousteau, *Prog. Mater. Sci.* 57, 1426 (2012).
17. W. Vogel, *Glass Chemistry* (Berlin: Springer, 1994).
18. P. Ravi, N. Vijaya, and N. Krishna Mohan, *Int. J. Sci. Res. Phys. Appl. Sci.* 6, 45 (2018).
19. R.N.A. Prasad, R. Praveena, N. Vijaya, P. Babu, and N. Krishna Mohan, *Mater. Res. Express* 6, 096204 (2019).
20. C.K. Jorgensen, *Orbitals in Atoms and Molecules* (London: Academic Press, 1962).
21. S.P. Sinha, *Complexes of the Rare Earths* (Oxford: Pergamon, 1966).
22. W.T. Carnall, P.R. Fields, and K. Rajnak, *J. Chem. Phys.* 49, 4424 (1968).
23. E. Rukmini and C.K. Jayasankar, *Phys. B* 212, 167 (1995).
24. R. Praveena, R. Vijaya, and C.K. Jayasankar, *Spectrochim. Acta A* 70, 577 (2008).
25. B.R. Judd, *Phys. Rev.* 127, 750 (1962).
26. G.S. Ofelt, *J. Chem. Phys.* 37, 511 (1962).
27. K. Upendra Kumar, P. Babu, K.H. Jang, H.J. Seo, C.K. Jayasankar, and A.S. Joshi, *J. Alloys Compd.* 458, 509 (2008).
28. R. Vijaya, V. Venkatramu, P. Babu, L. Rama Moorthy, and C.K. Jayasankar, *Mater. Chem. Phys.* 117, 131 (2009).
29. Z. Mazurak, M. Czaja, R. Lisiecki, and A. Meijerink, *J. Mater. Sci. Eng. Adv. Technol.* 5, 1 (2012).
30. D.V.R. Murthy, T. Sasikala, B.C. Jamalaiah, A.M. Babu, J.S. Kumar, M. Jayasimhadri, and L.R. Moorthy, *Opt. Commun.* 284, 603 (2011).
31. J.H. Campbell and T.I. Suratwala, *J. Non Cryst. Solids* 263, 318 (2000).
32. C.K. Jorgensen and R. Reisfeld, *J. Less Common Met.* 93, 107 (1983).
33. N. Chanthima, Y. Tariwong, T. Sareein, J. Kaewkhao, and N.W. Sangwaranatee, *Appl. Mech. Mater.* 879, 27 (2018).
34. E.W.J.L. Omen and A.M.A. Van Dungeon, *J. Non Cryst. Solids* 111, 205 (1989).
35. N. Deopa, A.S. Rao, M. Gupta, and G. Vijaya Prakash, *Opt. Mater.* 75, 127 (2018).
36. M. Zambelli, A. Speghini, G. Ingleto, C. Locatelli, M. Bettinelli, F. Vetrone, J.C. Boyer, and J.A. Capobianco, *Opt. Mater.* 25, 215 (2004).
37. E. Pecoraro, J.A. Sampaio, L.A.O. Nunes, S. Gama, and M.L. Baesso, *J. Non Cryst. Solids* 277, 73 (2000).
38. J.H. Choi, A. Margaryan, A. Margaryan, and F.G. Shi, *J. Lumin.* 114, 167 (2005).
39. I. Pal, A. Agarwal, S. Sanghi, M.P. Aggarwal, and S. Bhardwaj, *J. Alloys Compd.* 587, 332 (2014).
40. T.F. Xue, L.Y. Zhang, J.J. Hu, M.S. Liao, and L.L. Hu, *Opt. Mater.* 47, 24 (2015).
41. A.D. Sontakke, K. Biswas, A.K. Mandal, and K. Annapurna, *Appl. Phys. B* 101, 235 (2010).
42. J. Azevedo, J. Coelho, G. Hungerford, and N. Sooraj Hus-sain, *Phys. B* 405, 4696 (2010).
43. I. Pal, A. Agarwal, S. Sanghi Sanjay, and M.P. Aggarwal, *Indian J. Pure Appl. Phys.* 51, 18 (2013).
44. B. Karthikeyan, R. Philip, and S. Mohan, *Opt. Commun.* 246, 153 (2005).
45. M. Sobczyk, *J. Quant. Spectrosc. Rad. Transf.* 119, 128 (2013).
46. S. Srihari Sastry and B.R. Venkateswara Rao, *Indian J. Pure Appl. Phys.* 52, 491 (2014).
47. G.A. Kumar, A. Martinez, and E.D.L. Rosa, *J. Lumin.* 99, 141 (2002).
48. G.A. Kumar, P.R. Biju, C. Venugopal, and N.V. Unnikrishnan, *J. Non Cryst. Solids* 221, 47 (1997).
49. K. Zou, H. Guo, M. Lu, W. Li, C. Hou, W. Wei, J. He, B. Peng, and B. Xiangli, *Opt. Express* 17, 10001 (2009).
50. B. Karthikeyan and S. Mohan, *Mater. Res. Bull.* 39, 1507 (2004).
51. K. Mariselvam, R. Arun Kumar, and P. Manasa, *Inf. Phys. Technol.* 49, 18 (2018).
52. K. Mariselvam, R. Arun Kumar, and K. Suresh, *Physica B* 534, 68 (2018).
53. D.D. Ramteke, R.E. Kroon, and H.C. Swart, *J. Non Cryst. Solids* 457, 157 (2017).
54. T. Fuji, K. Kodaira, O. Kawachi, N. Tanaka, H. Yamashita, and M. Anpo, *J. Phys. Chem. B* 101, 10631 (1997).

Optical Absorption and NIR Photoluminescence of Nd³⁺-Activated Strontium Phosphate Glasses

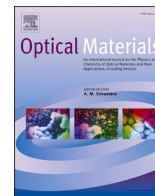
55. S. Shen, M. Naftaly, and A. Jha, *Opt. Commun.* 205, 101 (2002).
56. P. Babu, H.J. Seo, K.H. Jang, R. Balakrishnaiah, C.K. Jayasankar, K.S. Lim, and V. Lavin, *J. Opt. Soc. Am. B* 24, 2218 (2007).
57. P. Babu, H.J. Seo, K.H. Jang, R. Balakrishnaiah, C.K. Jayasankar, and A.S. Joshi, *J. Phys. Condens. Matter* 17, 4859 (2005).
58. R. Praveena, K.H. Jang, C.K. Jayasankar, and H.J. Seo, *J. Alloys Compd.* 496, 335 (2010).
59. F. Auzel, F. Bonfigli, S. Gagliari, and G. Baldacchini, *J. Lumin.* 94–95, 293 (2001).
60. F. Auzel, G. Baldacchini, L. Laversenne, and G. Boulon, *Opt. Mater.* 24, 103 (2003).
61. N. Yamada, S. Shionoya, and T. Kushida, *J. Phys. Soc. Jpn.* 32, 1577 (1972).
62. Z. Zhou, Y. Zhou, M. Zhou, X. Su, and P. Cheng, *J. Non Cryst. Solids* 470, 122 (2017).
63. Y. Che, Y. Huang, M. Huang, R. Chen, and Z. Luo, *J. Am. Ceram. Soc.* 88, 19 (2005).
64. J. Pisarska, W.A. Pisarski, and W.R. Romanowski, *Opt. Laser Technol.* 42, 805 (2010).
65. G. Gupta, A.D. Sontakke, P. Karmakar, K. Biswas, S. Balaji, R. Saha, R. Sen, and K. Annapurna, *J. Lumin.* 149, 163 (2014).
66. R.T. Karunakaran, K. Marimuthu, S. Arumugam, S. Surendra Babu, S.F. Leon-Luis, and C.K. Jayasankar, *Opt. Mater.* 32, 1035 (2010).

Publisher's Note Springer Nature remains neutral with regard to jurisdictional claims in published maps and institutional affiliations.



Contents lists available at ScienceDirect

Optical Materials

journal homepage: <http://www.elsevier.com/locate/optmat>

Role of excitation wavelength and dopant concentration on white light tunability of dysprosium doped titania-fluorophosphate glasses

N. Ravi^a, G. Neelima^{a,b}, Nanda Kumar Reddy Nallabala^c, Venkata Krishnaiah Kummara^{d,e,*}, R. Ravanamma^{a,b}, V. John Reddy^{b,j}, M. Prasanth^{b,f}, K. Suresh^a, P. Babu^g, V. Venkatramu^{h,i}

^a Department of Physics, Rajeev Gandhi Memorial College of Engineering & Technology, Nandyal-518501, India

^b Department of Physics, JNT University, Anantapuramu-515002, India

^c Department of Physics, Madanapalle Institute of Technology and Science, Madanapalle-517 325, India

^d Laser Applications Research Group, Ton Duc Thang University, Ho Chi Minh City, Viet Nam

^e Faculty of Applied Sciences, Ton Duc Thang University, Ho Chi Minh City, Viet Nam

^f Department of Physics, JNTUACE, Kalikiri-517234, India

^g Department of Physics, SVCR Government Degree College, Palamaner-517408, India

^h Department of Physics, Yogi Vemana University, Kadapa-516 005, India

ⁱ Department of Physics, Krishna University Dr. MRAR PG Centre, Nuzvid-521 201, India

^j Department of H&S (Physics), Nalla Narasimha Reddy Educational Society's Group of Institutions, Hyderabad, India

ARTICLE INFO

Keywords:

Oxyfluorophosphate glasses

Dy³⁺ ions

FTIR

Photoluminescence

Decay curves

White light tunability

ABSTRACT

Dysprosium-doped fluorophosphate glasses (P₂O₅-CaF₂-BaF₂-TiO₂-Dy₂O₃) have been prepared using melt-quenching technique and characterized their optical, structural, thermal and photoluminescence properties. Thermal stability (128 °C) of 0.5 mol% Dy₂O₃-doped glass has been estimated using Differential thermal analysis. Functional groups for 0.5 mol% Dy₂O₃-doped glass have been studied by Fourier Transform Infrared spectrum. Absorption spectra have been utilized for estimating the Judd-Ofelt (JO) parameters and allied properties. Several excitation wavelengths (350, 365, 387, 425, 452 and 472 nm) have been used for pumping the Dy³⁺ ions and analyzed for white luminescence. Intense emission has been observed for 0.5 and 1.5mol% of Dy₂O₃-doped glasses under 387 nm excitation. The ⁴F_{9/2} → ⁶H_{13/2} transition at 573 nm has unveiled a high stimulated emission cross-section (σ_{SE}) of 41.52 × 10⁻²² cm² for 0.5 mol% Dy₂O₃-doped glass. CIE coordinates fall close to the white region in CIE diagram, and hence these glasses are suitable for cold white light emitting diode applications.

1. Introduction

In the present market, white light emitting diodes (WLEDs) are premier light sources rather than the conventional fluorescent and incandescent light sources owing to their low power consumption, long operating lifetime, high brightness, higher efficiency, excellent reliability and environmental responsive characteristics [1–3]. Higher photoluminescence efficiency is essential to meliorate for these types of opto-electronic device applications [4]. In general, trivalent lanthanide (Ln³⁺) ions are active centers of luminescence in photonics and opto-electronics device applications. However, researchers are motivated extensively towards Ln³⁺:glasses for evolving the devices such as plasma displays, lasers, amplifiers, optical temperatures and WLEDs [5].

Trivalent dysprosium (Dy³⁺) (4f⁹) ion is one of the exciting Ln³⁺ ions

for exploring the luminescence properties owing to their usage in laser devices [6], telecommunication [7] and color display applications [8]. Moreover, Dy³⁺ ions exhibit intense yellow emission due to the ⁴F_{9/2} → ⁶H_{13/2} (electric dipole) transition than blue emission due to the ⁴F_{9/2} → ⁶H_{15/2} (magnetic dipole) transition [9–13]. Consequently, at the suitable ratio yellow-to-blue (Y/B) intensity ratio, Dy³⁺ ions are more fascinated for WLEDs. Therefore, it is recommended to use Dy³⁺ ions for white light sources.

Phosphate (P₂O₅) glasses are the prominent host materials for embedding Ln³⁺ ions for lighting applications among other glass formers due to their advantages such as reasonably low phonon energy and good stability. Oxyfluoride glasses have been offered their predominant properties by reason of collective advantages of matrices of oxide and fluoride such as low melting point, a low index of refraction and a low

* Corresponding author. Laser Applications Research Group, Ton Duc Thang University, Ho Chi Minh City, Viet Nam.

E-mail address: kvkrishaniah@tdtu.edu.vn (V.K. Kummara).

<https://doi.org/10.1016/j.optmat.2020.110593>

Received 12 August 2020; Received in revised form 10 October 2020; Accepted 27 October 2020

0925-3467/© 2020 Elsevier B.V. All rights reserved.

phonon energy, hence enhances the radiative transitions [14,15]. In addition, fluorophosphate glasses have been studied as dominant materials for solid state lasers. The influence of excitation wavelengths on color tunability of oxyfluorosilicate glasses modified with CaF_2 have been discussed for WLEDs [2]. Photoluminescence (PL) studies have been performed for Dy^{3+} -doped oxyfluorosilicate glasses modified with BaF_2 [16]. In this work, Dy^{3+} -doped titania fluorophosphate glasses are obtained by modifying phosphate network with CaF_2 and BaF_2 .

Dy^{3+} -doped glasses with various glass formers and modifiers are made with different molar ratios for the WLEDs applications, which include tellurite glasses: $47\text{TeO}_2\text{-}25\text{WO}_3\text{-}25\text{Li}_2\text{O-}3\text{Dy}_2\text{O}_3$ (TWLD_{3.0}) [2], germinate glasses: $30\text{B}_2\text{O}_3\text{-}40\text{GeO}_2\text{-}29\text{Gd}_2\text{O}_3\text{-}1\text{Dy}_2\text{O}_3$ (BGGD_{1.0}) [17], silicate glasses $35.7\text{SiO}_2\text{-}25.5\text{B}_2\text{O}_3\text{-}17\text{BaO}\text{-}3.4\text{K}_2\text{O}_3\text{-}4\text{Al}_2\text{O}_3\text{-}15\text{BaCl}_2\text{-}0.5\text{Dy}_2\text{O}_3$ (SBBaKABDy_{0.5}) [18], borate glasses: $50\text{B}_2\text{O}_3\text{-}x\text{LiF}\text{-}(30-x)\text{CaO-}20\text{Bi}_2\text{O}_3\text{-}1.0\text{Dy}_2\text{O}_3$ (BLfCBiDy_{1.0}) [19], phosphate glasses: $70\text{P}_2\text{O}_5\text{-}10\text{Bi}_2\text{O}_3\text{-}10\text{Na}_2\text{CO}_3\text{-}9\text{SrCO}_3\text{-}1.0\text{Dy}_2\text{O}_3$ (NaBiSrPDy_{1.0}) [20], $69.4\text{P}_2\text{O}_5\text{-}5\text{B}_2\text{O}_3\text{-}25\text{BaO}\text{-}0.6\text{Dy}_2\text{O}_3$ (PBBaDy_{0.6}) [21], $65\text{P}_2\text{O}_5\text{-}17\text{NaF}\text{-}17\text{Gd}_2\text{O}_3\text{-}1.0\text{Dy}_2\text{O}_3$ (PNfGdDy_{1.0}) [22], $44\text{P}_2\text{O}_5\text{-}17\text{K}_2\text{O}\text{-}9\text{Al}_2\text{O}_3\text{-}28\text{Nb}_2\text{O}_5\text{-}2.0\text{Dy}_2\text{O}_3$ (PKANbDy_{2.0}) [23].

The present research aims to examine the influence of Dy^{3+} ion concentration and excitation wavelengths on photoluminescence properties in particular white light tunability. From the differential thermal analysis (DTA) spectrum of PCBT_{0.5} glass, glass transition temperature, crystalline temperature and thermal stability are evaluated. By using Fourier transform infrared (FTIR) spectrum, the functional groups of Dy^{3+} ion doped titaniafluorophosphate glasses are assessed. The optical, PL and spectroscopic properties of PCBT_{0.5} glasses are analyzed. Lifetimes of the Dy^{3+} ions for various concentrations are estimated by means of the decay profiles. Color tunability of these glasses has been studied based on various concentrations of Dy^{3+} ions and pump wavelengths.

2. Experimental details

2.1. Glass synthesis

Melt-quenching technique [24] has been used for the synthesis of glasses with a composition of $60\text{P}_2\text{O}_5$ (99.9%) - 20CaF_2 (99.5%) - 15BaF_2 (99.0%) - 5TiO_2 (99.0%) - $x\text{Dy}_2\text{O}_3$ (99.8%) ($x = 0.5, 1.0, 1.5, 2.0$ and 2.5 mol %). The glasses were designated as PCBT_{0.5}, PCBT_{1.0}, PCBT_{1.5}, PCBT_{2.0} and PCBT_{2.5} for 0.5, 1.0, 1.5, 2.0 and 2.5 mol % Dy_2O_3 , respectively. 10 g of chemicals were thoroughly mixed by grinding for 1 h, then transferred to an alumina crucible and placed in a rectangular box-type heating furnace at $1300\text{ }^\circ\text{C}$ at a rate of $10\text{ }^\circ\text{C}/\text{min}$ for 90 min. The melt is poured into a pre-heated brass plate, maintained at $500\text{ }^\circ\text{C}$ and rapidly quenched. Then the glass was annealed at $500\text{ }^\circ\text{C}$ for 4 h and cooled to room temperature (RT). These glasses are polished for their optical quality and are used for optical characterization.

2.2. Characterization techniques

The DTA was performed by PerkinElmer (model- Diamond TG/DTA) from room temperature (RT) to $1000\text{ }^\circ\text{C}$ at a heating rate of $10\text{ }^\circ\text{C}/\text{min}$. The Fourier transform infrared (FTIR) spectra were obtained at RT (in the range of $500\text{-}3900\text{ cm}^{-1}$) by a ThermoFisher Scientific (model: Nicolet 6700 FTIR spectrometer). Absorption spectrum of PCBT_{2.0} glass was obtained by VARIAN Cary 5000 spectrophotometer in the region of $350\text{-}1900\text{ nm}$. PL spectra were measured by Edinburg Spectrofluorometer (FLS-980) with Xe lamp as an excitation source. Decay curves were measured with the same spectrometer under the Xe lamp excitation in the pulsed mode. Typical density (ρ) and thickness (t) of the glasses are found to be $3.11\text{ gm}/\text{cm}^3$ and 0.37 cm respectively.

3. Results and discussion

3.1. Thermal studies

The DTA curve of PCBT_{0.5} glass in Fig. 1 shows an endothermic peak corresponding to the glass transition temperature (T_g) at $552\text{ }^\circ\text{C}$ and the exothermic peak at $704\text{ }^\circ\text{C}$ associated to the peak crystalline temperature (T_c). The onset crystallization temperature (T_x at $629\text{ }^\circ\text{C}$) of PCBT_{0.5} glass is assessed by plotting a tangent in the straight section of the crystalline peak. The thermal stability (ΔT) of the glass, $T_x\text{-}T_g$, is an essential parameter for the optical fiber drawing. The glass should exhibit ΔT as high as possible to decrease scattering losses thereby increase optical performance of the fiber. The thermal stability (ΔT) is found to be $128\text{ }^\circ\text{C}$ which is higher than $103\text{ }^\circ\text{C}$ of calcium fluoride modified oxyfluorophosphate glass [25].

3.2. FTIR analysis

FTIR vibrational profile of PCBT_{0.5} glass at RT in the energy region of $500\text{-}3900\text{ cm}^{-1}$ is shown in Fig. 2. The spectrum shows numerous absorption bands around $752, 902, 1091, 1563, 1635, 2331, 3440$ and 3755 cm^{-1} . Usually, the IR bands in the range of $1200\text{-}1300\text{ cm}^{-1}$ is due to $\text{P}=\text{O}$ bonds from phosphate polymerization units. Phosphate ($\text{P}-\text{O}^-$) stretching bands reflected the energy range of $900\text{-}1100\text{ cm}^{-1}$ because of non-bridging oxygens (NBOs) and band at $\sim 750\text{ cm}^{-1}$ owing to the bridging oxygens (BOs) of $\text{P}-\text{O}-\text{P}$ vibrations [26]. The peaks at around ~ 3755 and 3440 cm^{-1} are attributed to $\text{H}-\text{O}-\text{H}$ stretching hydroxyl groups vibrations owing to NBOs in phosphate because of its high hygroscopic nature. The vibrational band $\sim 2331\text{ cm}^{-1}$ is owing to asymmetric stretching vibrations of the $\text{O}-\text{H}$ bond. The absorption bands at 1590 cm^{-1} and 1695 cm^{-1} are because of the bending vibrations of $\text{H}-\text{O}-\text{H}$ bonds due to moisture during the preparation and/or inherent present of OH ions in phosphate compounds. In general, IR spectrum of the glass sample is measured by the KBr pellet technique and is likely to be influenced by number of factors, including the atmospheric conditions around the IR spectrophotometer. In particular, the atmospheric moisture is easily absorbed by the sample or by the pellet, causing the appearance of IR bands belonging to H_2O molecules although the sample under investigation does not contain H_2O as a unit in the network. It is anticipated that IR bands of water arise mainly because of the hygroscopic nature of the glasses with higher phosphate content, and change in these bands with composition is indicative of changes in their hygroscopicity and hence changes in the glass structure or vice versa [27]. The intensity of the band at 1091 cm^{-1} is accredited to the end groups (Q^0) species of symmetric vibrations of (PO_3). The vibration of $\text{Ca}/\text{Ba}-\text{O}-\text{P}$ bonds is assigned to the band at 902 cm^{-1} due to asymmetric

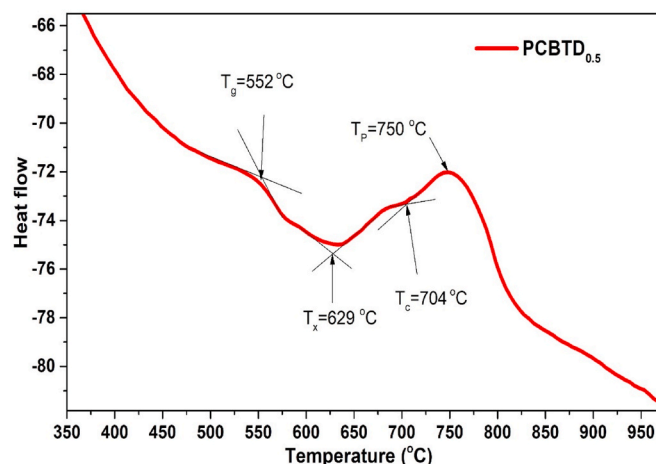


Fig. 1. DTA thermograph of PCBT_{0.5} glass.

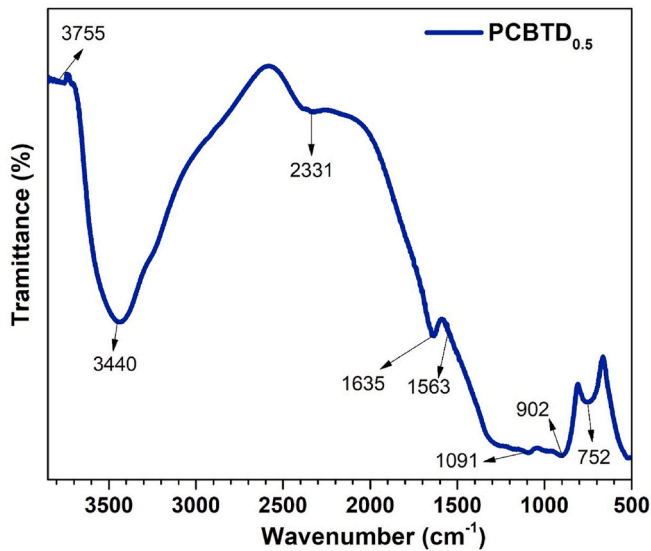


Fig. 2. FTIR profile of the PCBTd_{0.5} glass in the energy range of 500–3900 cm⁻¹.

stretching from metaphosphate of (PO₄)³⁻ groups. In addition, the band at 752 cm⁻¹ is for P–O–Ti symmetrical stretching mode [28].

3.3. Optical properties - optical absorption spectrum

The optical absorption spectrum (UV–Visible–NIR) of PCBTd_{2.0} glass in the wavelength range of 350–1900 nm is shown in Fig. 3. The spectrum exhibits eleven bands positioned at around 377, 387, 424, 452, 472, 748, 797, 894, 1093, 1268 and 1675 nm assigned to the transitions from ground ⁶H_{15/2} level to the different higher energy states, ⁴M_{19/2}, ⁴K_{17/2}, ⁴G_{11/2}, ⁴I_{15/2}, ⁴F_{9/2}, ⁶F_{3/2}, ⁶F_{5/2}, ⁶F_{7/2}, ⁶F_{9/2} + ⁶H_{7/2}, ⁶F_{11/2} + ⁶H_{9/2} and ⁶H_{11/2} of Dy³⁺ ions, respectively. From these bands, the 1268 nm band with an energy of 7886 cm⁻¹ corresponds to the ⁶H_{15/2} → ⁶F_{11/2} + ⁶H_{9/2} transition which is referred as hypersensitive transition because of its highest intensity compared to rest of the bands. It follows the selection rules (|ΔS| = 0, |ΔL| ≤ 2 and |ΔJ| ≤ 2) owing to the degree of asymmetry about Dy³⁺ ions [1,2]. Further, the strength of the ⁶H_{15/2} → ⁶F_{11/2} + ⁶H_{9/2} transition is highly sensitive to the ligand field of the Dy³⁺ ions. This absorption band shows the interaction of electric and

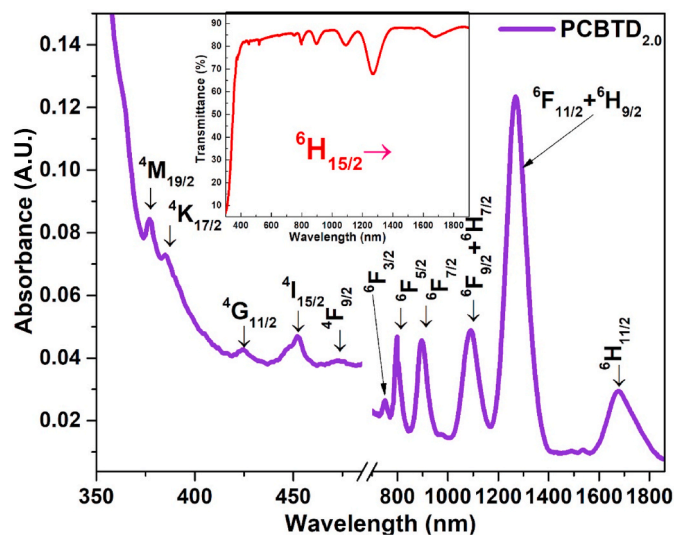


Fig. 3. Absorption spectrum in the UV–visible–NIR region of PCBTd_{2.0} glass. Inset shows the transmittance spectrum of the same glass.

magnetic dipoles, which leads to the transfer of energy (ET) during mutual relaxation (CR) between Dy³⁺ ions. In addition, the PCBTd_{2.0} glass transmittance spectrum shows about 90% of the most preferred transparency for optical applications, as shown in the inset of Fig. 3.

3.4. Judd-Ofelt theory

By applying the Judd-Ofelt (JO) theory [29,30] to the absorption spectrum of PCBTd_{2.0} glass, the JO intensity parameters are obtained from the JO theory. Intensity parameters and oscillator strengths are assessed by least square fitting method. Moreover, the optical absorption strength of the Dy³⁺ ions are associated to the JO parameters Ω_λ (λ = 2, 4, 6). These parameters illustrate the electric and magnetic-dipole strengths of the ligand field in the glass matrix [31]. Root mean square (rms) eccentricity between the experimental (*f_{exp}*) and calculated (*f_{cal}*) oscillator strengths is estimated as ± 0.287 × 10⁻⁶ which indicates a good quality of fit between *f_{exp}* and *f_{cal}*. In addition, it shows a trend of Ω₂ > Ω₄ > Ω₆ and are compared with the other glass trends shown in Table 1. The present glass exhibits higher covalence of Dy–O bonds. As can be seen, most of the Dy³⁺-doped phosphate glasses follow a similar trend in JO parameters.

Some of the evaluated parameters of the PCBTd_{2.0} glass such as radiative lifetime (τ_{rad}), experimental lifetime (τ_{exp}), emission cross-section (σ_{SE}, cm²) and gain bandwidth are presented in Table 2. The gain bandwidth (σ_{SE} × Δλ_{eff}, 10⁻²⁸, cm³) for the ⁴F_{9/2} → ⁶H_{13/2} transition of Dy³⁺ ions shows higher for the PCBTd_{0.5} glass among the glasses under study. It is found that the ⁴F_{9/2} → ⁶H_{13/2} transition displays a higher peak emission cross-section of 41.52 × 10⁻²² cm² at 573 nm for PCBTd_{0.5} glass among the glasses in the present investigation. This value obtained is found to be higher compared to 9.53 × 10⁻²² for YCaSBDy_{0.5} [33], 20.93 × 10⁻²² for BGGD_{1.0} [17], 21.3 × 10⁻²² for BaBPDy_{0.4} [21] and 39.4 × 10⁻²² for PPBGaDy_{2.5} [38] glasses whereas lower than 42.95 × 10⁻²² for TZPPNDy_{1.0} [36], 61.28 × 10⁻²² for DyNaFGdP_{1.0} [22], 62.86 × 10⁻²² for ZTFBD_{0.5} [37], 64 × 10⁻²² for PKANbDy_{2.0} [23] and 90.1 for NaBiSrPDy_{1.0} [20] glasses, as shown in Table 2.

3.5. Photoluminescence excitation

The excitation (λ_{ex}) spectrum of PCBTd_{0.5} glass is measured by monitoring the emission at 573 nm and is depicted in Fig. 4. The Dy³⁺ ion bands perceived in the excitation spectrum are centered at 350, 365, 387, 425, 452 and 472 nm and their associated transitions are ⁶H_{15/2} → ⁶P_{7/2}, ⁶P_{5/2}, ⁴M_{19/2} + ⁴K_{17/2} + ⁴M_{21/2} + ⁴I_{13/2} + ⁴F_{7/2}, ⁴G_{11/2}, ⁴I_{15/2} and ⁴F_{9/2}, respectively. A broad and intense excitation band is perceived at 387 nm due to the combination of five deconvoluted bands 377, 387, 389, 393 and 396 nm which resembles to the transition ⁶H_{15/2} → ⁴M_{19/2} + ⁴K_{17/2} + ⁴M_{21/2} + ⁴I_{13/2} + ⁴F_{7/2} resolved in the inset of Fig. 4. Moreover, the band at 387 nm is selected for exciting the Dy³⁺ ions in PCBTd glasses.

Table 1

Assessment of Judd-Ofelt (JO) intensity parameters (Ω₂, Ω₄ and Ω₆, × 10⁻²⁰ cm²), their trend for the PCBTd_{2.0} glass and other reported Dy³⁺ glasses.

Glass	Ref.	Ω ₂	Ω ₄	Ω ₆	Trend
PCBTd _{2.0}	[PW]	20.25	9.61	8.92	Ω ₂ > Ω ₄ > Ω ₆
TWLD _{3.0} (Tellurite)	[2]	16.00	2.39	3.75	Ω ₂ > Ω ₆ > Ω ₄
MgB2O3Dy _{0.7} (Borate)	[9]	23.02	12.86	12.17	Ω ₂ > Ω ₄ > Ω ₆
BGGD _{1.0} (Germanate)	[17]	3.65	0.65	1.57	Ω ₂ > Ω ₆ > Ω ₄
NaBiSrPDy _{1.0} (Phosphate)	[20]	2.48	0.82	0.61	Ω ₂ > Ω ₄ > Ω ₆
BaBPDy _{0.4} (Phosphate)	[21]	4.47	1.27	0.99	Ω ₂ > Ω ₄ > Ω ₆
DyNaFGdP _{1.0} (Phosphate)	[22]	16.83	8.87	6.25	Ω ₂ > Ω ₄ > Ω ₆
PKANbDy _{2.0} (Phosphate)	[23]	23.01	0.72	3.53	Ω ₂ > Ω ₆ > Ω ₄
GePbDy ₁₀ (Germanate)	[32]	6.41	1.02	2.25	Ω ₂ > Ω ₆ > Ω ₄
YCaSBDy _{0.5} (Borate)	[33]	2.84	0.15	0.95	Ω ₂ > Ω ₆ > Ω ₄
AYCBSMTD _{2.0} (Tellurite)	[34]	3.09	0.88	2.19	Ω ₂ > Ω ₆ > Ω ₄
PbAlSiDy _{1.0} (Silicate)	[35]	15.71	0.92	2.83	Ω ₂ > Ω ₆ > Ω ₄

Table 2

Comparison of radiative (τ_{rad} , ms) and experimental (τ_{exp} , ms) lifetimes of ${}^4\text{F}_{9/2}$ level, stimulated emission cross sections (σ_{SE} , $\times 10^{-22}$ cm 2) and gain bandwidth ($\sigma_{\text{SE}} \times \Delta\lambda_{\text{eff}}$ 10^{-28} cm 2) of ${}^4\text{F}_{9/2} \rightarrow {}^6\text{H}_{13/2}$ transition and Y/B ratios of Dy $^{3+}$ -doped PCBT $_{0.5}$ glass with other reported Dy $^{3+}$ -glasses.

Glass matrix	Ref.	τ_{R} (ms)	τ_{exp} (ms)	$\sigma_{\text{em}} \times 10^{-22}$ cm 2	Y/B	$\sigma_{\text{SE}} \times \Delta\lambda_{\text{eff}}$ 10^{-28} cm 3
PCBT $_{0.5}$	[PW]	0.78	0.15	41.52	3.10	39.77
TWLD $_{3.0}$	[2]	0.075	0.05	–	2.46	–
BGGD $_{1.0}$	[17]	0.84	0.38	20.93	2.25	40.83
NaBiSrPDy $_{1.0}$	[20]	0.13	0.06	90.1	–	126
BaBPDy $_{0.4}$	[21]	2.01	0.65	21.3	–	28.71
DyNaFGdP $_{1.0}$	[22]	0.61	0.53	61.28	1.94	–
PKANbDy $_{2.0}$	[23]	0.44	0.17	64.00	5.08	118.97
YCaSBDy $_{0.5}$	[33]	1.78	0.69	9.53	1.30	17.08
TZPPNdY $_{1.0}$	[35]	0.37	0.33	42.95	–	59.25
ZTFBD $_{0.5}$	[36]	0.89	0.40	62.86	1.11	45.11
PPBGaDy $_{2.5}$	[38]	0.55	0.44	39.4	2.05	58.3

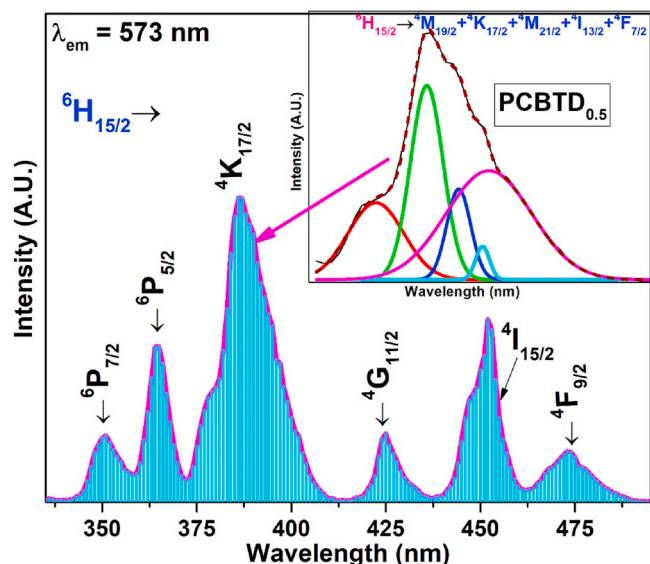


Fig. 4. PL excitation spectrum of PCBT $_{0.5}$ glass upon monitoring the emission at 573 nm.

3.6. Photoluminescence spectra

The luminescence spectra of the Dy $^{3+}$ ions doped PCBT glasses are obtained from 400 to 800 nm by exciting at 387 nm and are shown in Fig. S1 (provided in the supplementary information). Four emission bands are observed in the spectra at 483, 573, 662 and 753 nm correspond to the ${}^4\text{F}_{9/2} \rightarrow {}^6\text{H}_{15/2}$, ${}^6\text{H}_{13/2}$, ${}^6\text{H}_{11/2}$, and ${}^6\text{H}_{9/2}$ transitions, respectively. Among these, the ${}^4\text{F}_{9/2} \rightarrow {}^6\text{H}_{15/2}$ transition ($\Delta J = 3$) is due to magnetic-dipole (MD) that gives blue emission with low emission intensity and the ${}^4\text{F}_{9/2} \rightarrow {}^6\text{H}_{13/2}$ transition ($\Delta J = \pm 2$) is due to electric-dipole (ED) that yields highest intensity, among the other transitions, known as hypersensitive transition [19,20]. Moreover, the PCBT $_{0.5}$ glass gives intense yellow emission for the ${}^4\text{F}_{9/2} \rightarrow {}^6\text{H}_{15/2}$ transition. Gradual decrease in the intensity of yellow emission was noticed with the increase of Dy $^{3+}$ ions up to 2.5 mol% concentration from 0.5 mol%. The PCBT $_{0.5}$ glass is optimum under 387 nm excitation as it gives intense emission for 0.5 mol% of Dy $_{2\text{O}_3}$, which can be further exploited under different excitation wavelengths.

PL spectra of PCBT glasses upon several excitation wavelengths are shown in Fig. 5. Further, to optimize the white light emission of these glasses, the optimum glass (PCBT $_{0.5}$) is excited by several excitation wavelengths. In fact, for PCBT $_{0.5}$ glass exhibits an intense emission that can be excited under different wavelengths which include 350, 365, 387,

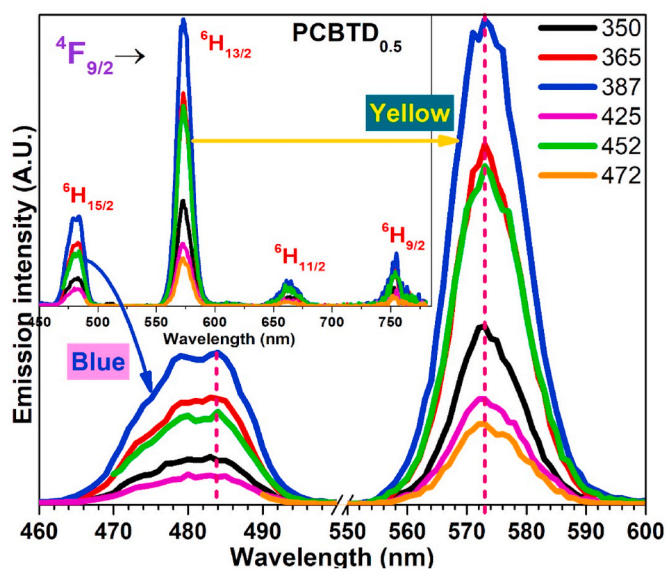


Fig. 5. PL emission spectra of two transitions of Dy $^{3+}$ ions in PCBT $_{0.5}$ glass under 350, 365, 387, 425, 452 and 472 nm excitations. Inset demonstrates the PL spectra of the same glass in the range of 450–810 nm under different excitation wavelengths.

425, 452 and 472 nm. When the excitation wavelength increased from 350 to 387 nm, the peak position for the ${}^4\text{F}_{9/2} \rightarrow {}^6\text{H}_{13/2}$ transition shifts slightly towards higher wavelengths (lower energy) and later the shift decreases with increase in the excitation wavelength, as shown in Fig. 5. The PL spectra of PCBT $_{0.5}$ glass is obtained upon several excitation wavelengths. It is observed that the strength of the bands is significantly high at the excitation wavelength of 387 nm. Similar trend is also observed for blue emission.

The Dy $^{3+}$ ions are pumped to the higher states in the glass, the peak positions of the emission spectra shift slightly from their mean positions. Yellow emission intensity of various Dy $^{3+}$ ion concentration is influenced by different excitation wavelengths, as displayed in Fig. 6. Consequently, 0.5 mol% of Dy $_{2\text{O}_3}$ -doped glass conveyed high emission intensity under 387 nm excitation, however for 1.0 mol% Dy $_{2\text{O}_3}$ -doped glass high intensity was perceived for the excitation wavelength of 365 nm compared to 387 nm. Moreover, the glass with 2.5 mol% Dy $_{2\text{O}_3}$ content shows an intense yellow emission under the 452 nm excitation wavelength compared to the 387 nm. For the rest of the concentrations, intense emission was reported for the excitation wavelength of 387 nm. This is because of the manifestation of high concentration of Dy $^{3+}$ ions.

For various Dy $^{3+}$ ions concentrations, the shift of peak positions under several excitation wavelengths is presented in Fig. S2. Intense yellow emission at 573 nm for the ${}^4\text{F}_{9/2} \rightarrow {}^6\text{H}_{13/2}$ transition of Dy $^{3+}$ ions doped glasses is obtained under different excitation wavelengths. It is interesting to note that under 387 nm excitation, a blue shift is observed for yellow emission with increase of Dy $^{3+}$ ions concentration. A red shift known as Stokes shift towards higher wavelengths from 573 nm to 574.09 nm ($\Delta\lambda = 1.09$ nm) is observed for 1.0 mol% of Dy $_{2\text{O}_3}$ -doped glass under different excitations. Furthermore, at higher concentrations of 2.0 and 2.5 mol% of Dy $_{2\text{O}_3}$, the yellow emission was shifted in the range of 571.9–573 nm ($\Delta\lambda = 1.1$ nm) and 571.99–574 nm ($\Delta\lambda = 2.0$ nm) that is towards blue shift known as anti-Stokes shift which may be owing to increase of Dy $^{3+}$ ions. Shift in the peak positions is around 2 nm which is significantly more at higher Dy $^{3+}$ ions concentration (2.5 mol%) compared to 0.51 nm at low concentrations (0.5 mol%). Over all, a red shift is observed when Dy $^{3+}$ ions concentration is increased in these glasses.

On the other hand, full width at half maxima (FWHM) and integrated area (intensity) for yellow emission are shown in Figs.S3 (a) and (b). The FWHM increases in the range of 13.0–14.4 nm with increase in the

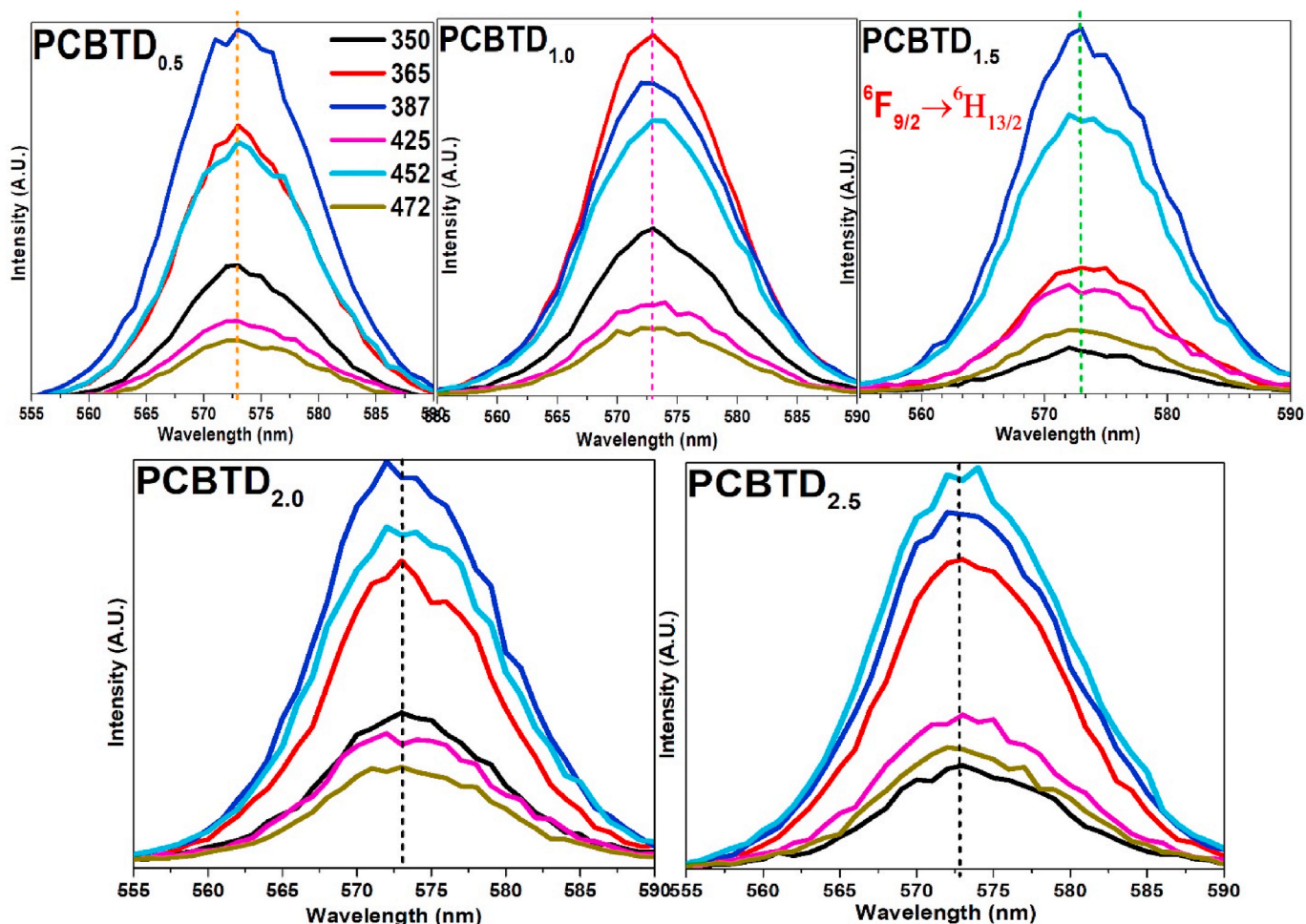


Fig. 6. PL emission spectra for several concentrations of Dy^{3+} -doped PCBTD glasses upon different $\lambda_{\text{ex}} = 350, 365, 387, 425, 452$ and 472 nm.

excitation wavelengths in the range of 350–472 nm for PCBTD_{0.5} glass. Later, it decreases to a value of 13.9 nm for 425 nm wavelength excitation and increases slightly to 14.1 nm for the excitation wavelengths 452 and 472 nm. On the other hand, for PCBTD_{0.5} glass, under 350 & 387 nm excitation wavelengths, the integrated intensity increases significantly and then decrease for higher excitation wavelengths.

Y/B ratio is obtained by exploring the integrated area of the two prominent transitions, ${}^4\text{F}_{9/2} \rightarrow {}^6\text{H}_{13/2}$ and ${}^4\text{F}_{9/2} \rightarrow {}^6\text{H}_{15/2}$. This is used to know the material that has the co-ordination number and equilibrium around the Dy^{3+} ions [39]. The Y/B intensity ratio increases till 1.5 mol % of Dy_2O_3 content and declines with further increase of Dy^{3+} ions concentration, as shown in Fig. S4. Usually, the behavior of Y/B intensity ratio be contingent on the trend of PL intensity in regard to Dy^{3+} concentration. Among the present glass systems, the PCBTD_{0.5} glass shows an intense emission with a higher value of FWHM (14.39 nm). On the other hand, Y/B ratio declines with the increase of Dy^{3+} ion concentration beyond 1.5 mol% Dy_2O_3 . This is due to concentration quenching which leads to the ET between the Dy^{3+} ions. Similar results were discerned for the other glasses [40].

Energy level diagram of Dy^{3+} ions in PCBTD glasses including the radiative and non-radiative channels is shown in Fig. 7. Several excitation wavelengths that includes 350, 365, 387, 425, 452, and 472 nm are employed to vary the emission colors of Dy^{3+} ions. Under 350 nm excitation, Dy^{3+} ions are excited to the ${}^6\text{P}_{7/2}$ from the ${}^6\text{H}_{15/2}$ level. They de-excite to the ${}^4\text{F}_{9/2}$ meta-stable state (whose lifetime is relatively high) through non-radiative transitions because of short lifetime and low energy separation among the higher energy levels [38]. Similar phenomena is applicable to all excitation wavelengths except 472 nm, in this

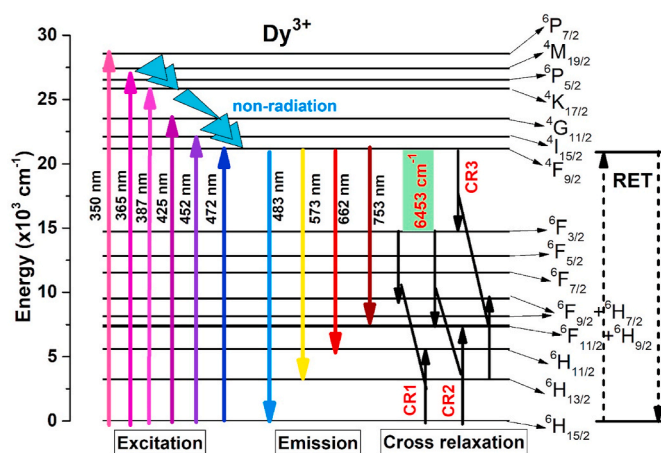


Fig. 7. Partial energy level structure of Dy^{3+} ions in PCBTD glasses. The various excitation, emission and CR channels are also shown along with non-radiation processes. RET: Resonance energy transfer.

case the Dy^{3+} ions are excited resonantly to ${}^4\text{F}_{9/2}$ level. From the ${}^4\text{F}_{9/2}$ level, radiative emission transitions, ${}^4\text{F}_{9/2} \rightarrow {}^6\text{H}_{15/2}$, ${}^6\text{H}_{13/2}$, ${}^6\text{H}_{11/2}$ and ${}^6\text{H}_{9/2}$ occur giving rise to blue, yellow, red and NIR emissions, respectively. At higher concentrations, the energy transfer (ET) through cross-relaxations (CR1, CR2 and CR3) between the adjacent Dy^{3+} ions occur because of multi-polar interaction, which leads to concentration

quenching of luminescence. In general, CR1, CR2 and CR3 occurs when the ET from the emission transitions perfectly counterparts with transitions of the absorption [25].

$$\text{CR1: } {}^6\text{F}_{3/2}, {}^6\text{H}_{15/2} \rightarrow {}^6\text{F}_{9/2} + {}^6\text{H}_{7/2}, {}^6\text{H}_{11/2}$$

$$\text{CR2: } {}^6\text{F}_{3/2}, {}^6\text{H}_{15/2} \rightarrow {}^6\text{F}_{11/2} + {}^6\text{H}_{9/2}$$

$$\text{CR3: } {}^4\text{F}_{9/2}, {}^6\text{H}_{13/2} \rightarrow {}^6\text{F}_{3/2}, {}^6\text{F}_{9/2} + {}^6\text{H}_{7/2}$$

Resonant energy transfer (RET) is established among the Dy^{3+} ion levels ${}^4\text{F}_{9/2} \leftrightarrow {}^6\text{H}_{15/2}$ and vice versa. The luminescence properties are changed due to RET, CR1, CR2 and CR3 with an increase in the concentration of Dy^{3+} ions. This can be confirmed by analyzing the decay curves, as shown in the next sections.

3.7. Fluorescence decay curves

Decay profiles of level ${}^4\text{F}_{9/2}$ of Dy^{3+} ions in PCBDT glass were measured upon 387 nm excitation by monitoring emission at 573 nm and are presented in Fig. 8. The decay curves show a non-exponential pattern for all the concentrations of Dy^{3+} ions. This is due to ET attributable to dipole-dipole interactions among the Dy^{3+} ions via CR channels. These curves were fitted using the following Eq. (1),

$$I(t) = A_1 \exp(-t/\tau_1) + A_2 \exp(-t/\tau_2) \quad (1)$$

where A_1 & A_2 and τ_1 & τ_2 are the constants and decay times correspond to the slow and fast components of the decay curves, respectively. τ_{exp} is experimental lifetime for the ${}^4\text{F}_{9/2}$ level, evaluated with the following Eq. (2),

$$\tau_{\text{exp}} = \frac{A_1 \tau_1^2 + A_2 \tau_2^2}{A_1 \tau_1 + A_2 \tau_2} \quad (2)$$

Decrease of τ_{exp} values for Dy^{3+} ions are noticed with increase of Dy^{3+} ions concentration which are found to be 151, 145, 129, 35 and 20 μs for the PCBDT_{0.5}, PCBDT_{1.0}, PCBDT_{1.5}, PCBDT_{2.0} and PCBDT_{2.5} glasses, respectively. The PCBDT_{0.5} glass discloses a higher lifetime of 151 μs compared to the rest of the studied glasses. In the case of glasses doped with RE^{3+} ions, ET through CR mechanism is accountable for the behavior of non-exponential. However, the decrease of lifetime in PCBDT glasses indicates the presence of ET from excited to neighboring unexcited Dy^{3+} ions [40].

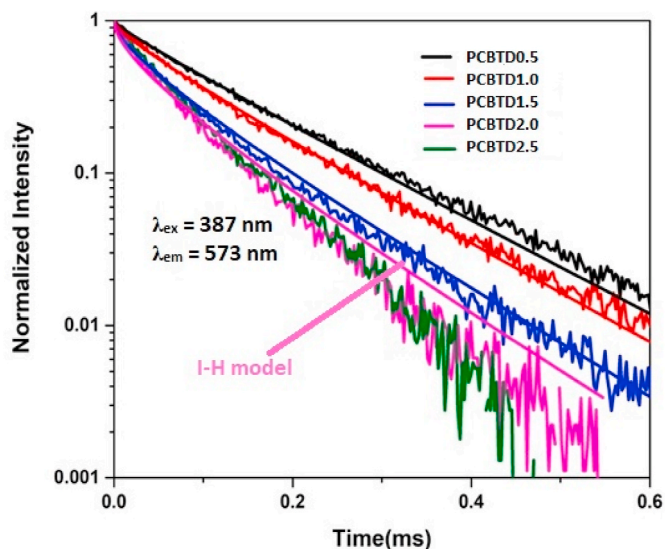


Fig. 8. Decay profiles for the excited state, ${}^4\text{F}_{9/2}$ of Dy^{3+} ions in PCBDT glasses under 387 nm excitation. Solid lines are fittings of the non-exponential curves to the I-H model.

The Inokuti-Hirayama (IH) model [41] is utilized when the ET process between an activator and sensitizer ions is much faster than energy diffusion. According to IH model, the PL intensity is defined by the following Eq.,

$$I(t) = I_0 \exp\left\{-\frac{t}{\tau_0} - Q\left(\frac{t}{\tau_0}\right)^{3/S}\right\} \quad (3)$$

where $S = 6, 8$ and 10 , t is the time afterward excitation, τ_0 is the intrinsic decay time of the activators in the absence of acceptors, Q is the ET parameter given by Eq.,

$$Q = \frac{4\pi}{3} \Gamma\left(1 - \frac{3}{S}\right) N_0 R_0^3 \quad (4)$$

where $S = 6, 8$ and 10 for dipole-dipole ($\Gamma(x) = 1.77$), dipole-quadrupole ($\Gamma(x) = 1.43$) and quadrupole-quadrupole ($\Gamma(x) = 1.3$) interactions, respectively. N_0 is activator ion concentration and R_0 is the critical transfer distance between the activator and sensitizer. The activator-sensitizer interaction parameter (C_{DA}) is defined by Eq.,

$$C_{DA} = \frac{R_0^S}{\tau_0} \quad (5)$$

The decay curve is well correlated with Eq. (3) when $S = 6$, which shows that the ET in CR among the Dy^{3+} ions in the PCBDT glass is dipole, as shown in Fig. 8. The energy transfer parameter (Q), activator-sensitizer interaction parameter (C_{DA}) and critical distance (R_0) are evaluated for 2.0 mol% Dy_2O_3 doped glass and are found to be 0.433, $4.45 \times 10^{-42} \text{ cm}^6/\text{s}$ and 8.5 \AA , respectively.

3.8. CIE color coordinate diagram

Emission color of Dy^{3+} -doped PCBDT glasses is examined with CIE (Commission Internationale de l'Éclairage) 1931 chromaticity diagram. The color coordinates of CIE (x, y) were estimated according to the procedure described elsewhere [42] and are presented in Table 3 and Fig. 9. The chromaticity coordinates (x, y) are found to be (0.4, 0.45), (0.4, 0.45), (0.41, 0.46), (0.41, 0.45) and (0.4, 0.46) for the PCBDT_{0.5}, PCBDT_{1.0}, PCBDT_{1.5}, PCBDT_{2.0} and PCBDT_{2.5} glasses, respectively. In addition, the corresponding correlated color temperature (CCT) values are calculated for different excitation wavelengths to know the emitted light is either “cold” or “warm” in nature. According to the McCamy’s approach [43], the CCT value for the PCBDT glass is evaluated from the following Eq. (6).

$$\text{CCT} = -449n^3 + 3525n^2 - 6823n + 5520.33 \quad (6)$$

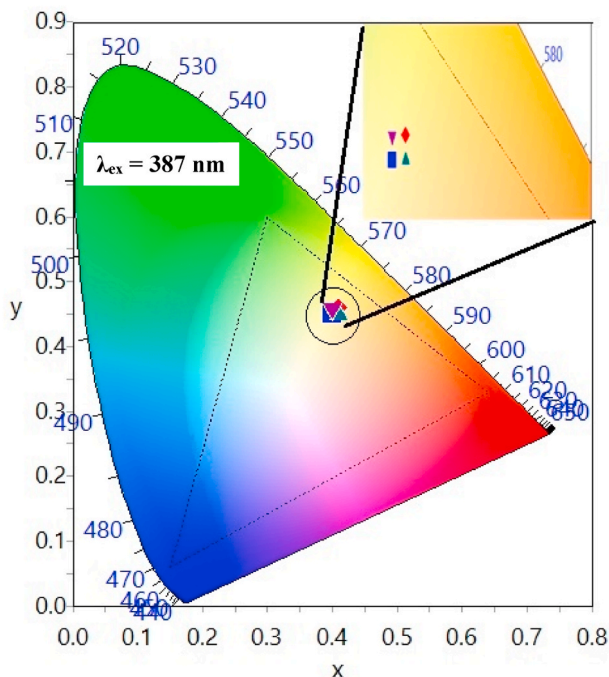
where $n = (x-x_e)/(y-y_e)$ is the converse slope line, $x_e = 0.332$ and $y_e = 0.186$ are the epicenter. Table 3 presents the color coordinates and CCT values of Dy^{3+} -doped glasses under different excitation wavelengths. The CCT values are obtained in the region of 3814–4057 K. Basically, light sources with CCT less than or equal to 3200 K usually exhibit a warm white light, whereas the light sources with CCT \sim 3700–5000 K emit pure white light, as displayed in Fig. 9. In these PCBDT glasses, the CCT values of 4000 K indicates the emission of pure white light. Location of the color coordinates with magnification is shown in the inset of Fig. 9.

As can be seen, color coordinates of the PCBDT_{0.5} glass are almost close to the region of white light under different excitation wavelengths and are shown in Fig. 10. The emission color of the glass shifts from warm white to pure white light region as can be seen from their CCT values which are obtained in the range of 3413–4752 K. For all excitation wavelengths, the emission chromaticity is almost same. However, owing to higher CCT values around 3814–6332 K for PCBDT_{2.0} glass, i. e., emission chromaticity is very near to the white light region and shifts from pure white to cool white light region. Especially, for the several excitation wavelengths of 350, 365 and 425 nm, the emission appeared

Table 3

CIE chromaticity (x, y) coordinates and CCT values of PCBTd glasses at several excitation wavelengths.

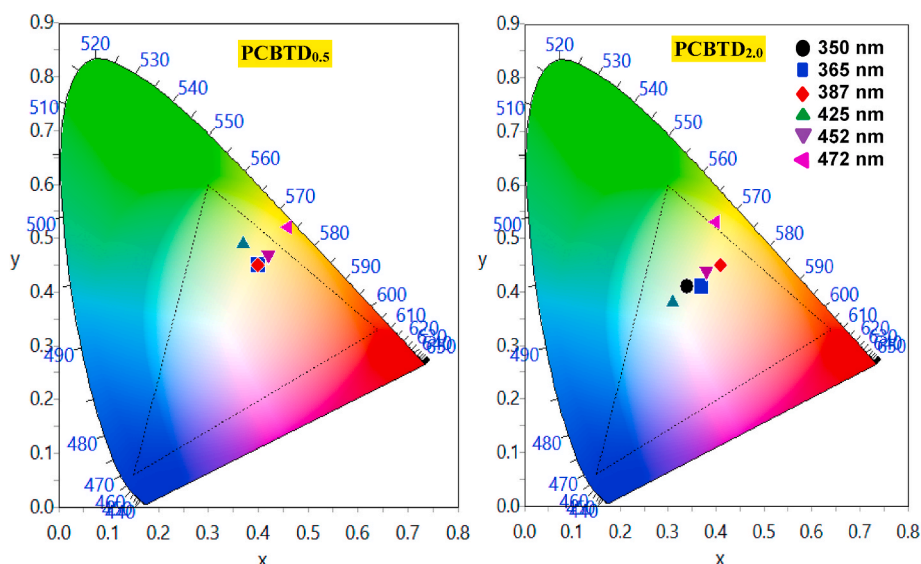
λ_{ex} (nm)	PCBTd _{0.5}			PCBTd _{1.0}			PCBTd _{1.5}			PCBTd _{2.0}			PCBTd _{2.5}		
	x	y	CCT												
350	0.4	0.45	4006	0.4	0.45	4006	0.38	0.42	4278	0.34	0.41	5294	0.38	0.43	4328
365	0.4	0.45	4006	0.4	0.45	4006	0.4	0.45	4006	0.37	0.41	4475	0.39	0.45	4207
387	0.4	0.45	4006	0.4	0.45	4006	0.41	0.46	3870	0.41	0.45	3814	0.4	0.46	4057
425	0.37	0.49	4752	0.36	0.48	4929	0.36	0.48	4929	0.31	0.38	6332	0.35	0.48	–
452	0.42	0.47	3747	0.41	0.47	3923	0.42	0.47	3747	0.38	0.44	4374	0.41	0.47	3923
472	0.46	0.52	3413	0.46	0.52	3413	0.46	0.52	3413	0.4	0.53	–	0.45	0.52	3549

**Fig. 9.** Position of emission color Dy³⁺-doped PCBTd glasses through CIE diagram. Inset shows the magnified region of the color coordinates.

almost in the white light region and is presented in Fig. 10. The study revealed that the effect of excitation wavelengths is more significant on emission color of Dy³⁺ ions compared to the Dy³⁺ ion concentrations. The 2.0 and 2.5 mol% of Dy³⁺ ions doped glasses are most significant samples for the fabrication of w-LEDs. Effect of different excitation wavelengths on emission properties were reported for Dy³⁺-doped oxyfluoride silicate [3], borogermante [17], calcium alumina-borosilicate [5], oxyfluoride glass [42] and sodium-aluminum phosphate [44] glasses.

4. Conclusion

Dy³⁺-doped titaniafluorophosphate (PCBTd) glasses have been fabricated by usual melt-quenching procedure and investigated their structural, optical and photoluminescence properties. DTA analysis of PCBTd_{0.5} glass shows that the glass exhibits a good thermal stability (128 °C). FTIR analysis revealed the presence of functional groups of the phosphate network and other vibrational and stretching structural units. JO intensity parameters have been evaluated for the PCBTd_{2.0} glass. Intense yellow (573) and moderate-intense blue (483) emissions were observed under 387 nm excitation. Yellow to blue (Y/B) intensity ratios and CIE color coordinates are estimated from emission spectra for several Dy³⁺ ions concentrations and excitation wavelengths which show feasibility for the extraction of white light. Fluorescence decay rates of the ⁴F_{9/2} level of the Dy³⁺ ions show a progressive non-exponential behavior associated with quenching of lifetimes with increase in Dy³⁺ ions concentration due to the increase in ET process between Dy³⁺ ions. Effect of different excitation wavelengths and various Dy³⁺ ion concentrations on color coordinates and CCT values are discussed and displayed in CIE diagram. Different excitation wavelengths are used for the white light tunability of these glasses.

**Fig. 10.** Location of CIE color coordinates of PCBTd_{0.5} and PCBTd_{2.0} glasses under different excitation wavelengths.

CRedit authorship contribution statement

N. Ravi: Conceptualization, Data curation, Roles/, Writing - original draft, Formal analysis, Investigation, Resources, Supervision. **G. Neelima:** Methodology, Formal analysis. **Nanda Kumar Reddy Nallabala:** Formal analysis, Writing - review & editing. **Venkata Krishnaiah Kummara:** Conceptualization, Data curation, Roles/, Writing - original draft, Formal analysis, Investigation, Resources, Supervision. **R. Ravanamma:** Methodology, Formal analysis. **V. John Reddy:** Software, Validation, Visualization. **M. Prasanth:** Software, Validation, Visualization. **K. Suresh:** Software, Validation, Visualization. **P. Babu:** Formal analysis, Writing - review & editing. **V. Venkatramu:** Formal analysis, Writing - review & editing.

Declaration of competing interest

The authors declare that they have no known competing financial interests or personal relationships that could have appeared to influence the work reported in this paper.

Acknowledgements

One of the authors Venkatramu is grateful to DST, New Delhi for the sanction of research project (No. INT/PORTUGAL/P-04/2017) under India-Portugal bilateral scientific and technological cooperation. Another author, Dr. Nallabala Nanda Kumar Reddy thankfully acknowledges the financial support from the Department of Science and Technology (DST), Science and Engineering Research Board, Government of India, project No. ECR/2017/002868.

Appendix A. Supplementary data

Supplementary data related to this article can be found at <https://doi.org/10.1016/j.optmat.2020.110593>.

References

- [1] U. Caldiño, A. Lira, A.N. Meza-Rocha, I. Camarillo, R. Lozada-Morales, Development of sodium-zinc phosphate glasses doped with Dy³⁺, Eu³⁺ and Dy³⁺/Eu³⁺ for yellow laser medium, reddish-orange and white phosphor applications, *J. Lumin.* 194 (2018) 231–239.
- [2] O. Kibril, A.E. Ersundu, M. Çelikkbilek Ersundu, Dy³⁺ doped tellurite glasses for solid-state lighting: an investigation through physical, thermal, structural and optical spectroscopy studies, *J. Non-Cryst. Solids* 513 (2019) 125–136.
- [3] Chaofeng Zhu, Xianghua Zhang, Hongli Ma, Claire Timlin, Sb-, Dy-, and Eu-doped oxyfluoride silicate glasses for light emitting diodes, *J. Alloys Compd.* 647 (2015) 880–885.
- [4] Yukio Narukawa, Masatsugu Ichikawa, Daisuke Sanga, Masahiko Sano, Takashi Mukai, White light emitting diodes with super-high luminous efficacy, *J. Phys. Appl. Phys.* 43 (35) (2010) 354002.
- [5] Yao Zhou, Chaofeng Zhu, Meimei Zhang, Jianan Liu, Optical properties of Eu- and Dy-doped calcium aluminoborosilicate glasses for LED applications, *J. Alloys Compd.* 688 (2016) 715–720.
- [6] Y. Fujimoto, O. Ishii, M. Yamazaki, Yellow laser oscillation in Dy³⁺-doped waterproof fluoro-aluminate glass fibre pumped by 398.8 nm GaN laser diodes, *Electron. Lett.* 46 (2010) 586–587.
- [7] Ralph H. Page, Kathleen I. Schaffers, Stephen A. Payne, William F. Krupke, Dy-doped chlorides as gain media for 1.3 μm telecommunications amplifiers, *J. Lightwave Technol.* 15 (1997) 786–793.
- [8] Chaofeng Zhu, Jia Wang, Meimei Zhang, Xiaorong Ren, Jianxing Shen, Yuanzheng Yue, Eu-, Tb-, and Dy-doped oxyfluoride silicate glasses for LED applications, *J. Am. Ceram. Soc.* 97 (3) (2014) 854–861.
- [9] A. Ichoja, S. Hashim, S.K. Ghoshal, L.H. Hashim, R.S. Omar, Physical, structural and optical studies on magnesium borate glasses doped with dysprosium ion, *J. Rare Earths* 36 (12) (2018) 1264–1271.
- [10] Sk Nayab Rasool, L. Rama Moorthy, C.K. Jayasankar, Optical and luminescence properties of Dy³⁺ ions in phosphate based glasses, *Solid State Sci.* 22 (2013) 82–90.
- [11] P. Babu, Kyoung Hyuk Jang, Eun Sik Kim, Liang Shi, R. Vijaya, V. Lavin, C. K. Jayasankar, Hyo Jin Seo, Optical properties and energy transfer in Dy³⁺-doped transparent oxyfluoride glasses and glass ceramics, *J. Non-Cryst. Solids* 356 (4–5) (2010) 236–243.
- [12] N. Vijaya, K. Uendra Kumar, C.K. Jayasankar, “Dy³⁺ -doped zinc fluorophosphate glasses for white luminescence applications,” *Spectrochim. Acta Mol. Biomol. Spectrosc.* 113 (2013) 145–153.

- [13] P. Babu, Kyoung Hyuk Jang, Ch Srinivasa Rao, Liang Shi, C.K. Jayasankar, Víctor Lavín and Hyo Jin Seo, “White light generation in Dy³⁺-doped oxyfluoride glass and transparent glass-ceramics containing CaF₂ nanocrystals,” *Optic Express* 19 (3) (2011) 1836–1841.
- [14] Haruka George, Nisha Deopa, Sumandeep Kaur, Aman Prasad, M. Sreenivasulu, M. Jayasimhadri, A.S. Rao, Judd-Ofelt parametrization and radiative analysis of Dy³⁺ ions doped Sodium Bismuth Strontium Phosphate glasses, *J. Lumin.* 215 (2019) 116693.
- [15] C. T. Lin, S. W. Yung, J. Lin, W. S. Chen, C. H. Lai, Y. M. Lee, J. S. Lin, Luminescence properties of Tm³⁺/Dy³⁺ co-doped zinc-aluminum phosphate glasses for white LED, *Adv. Mater. Res.*, Vol. 602–604, pp 821–828.
- [16] G. Lakshminarayana, Jianrong Qiu, Photoluminescence of Pr³⁺, Sm³⁺ and Dy³⁺-doped SiO₂-Al₂O₃-BaF₂-GdF₃ glasses, *J. Alloys Compd.* 476 (2009) 470–476.
- [17] Melis Gokce, Deniz Kocyigit, Spectroscopic investigations of Dy³⁺ doped borogermanate glasses for laser and wLED applications, *Opt. Mater.* 89 (2019) 568–575.
- [18] Nilanjana Shasmal, Basudeb Karmakar, White light-emitting Dy³⁺-doped transparent chloroborosilicate glass: synthesis and optical properties, *Journal of Asian Ceramics Societies* 7 (2019) 42–52.
- [19] P. Narwal, Manjeet S. Dahiya, A. Yadav, A. Hooda, A. Agarwal, S. Khosa, Improved white light emission in Dy³⁺ doped LiF-CaO-Bi₂O₃-B₂O₃ glasses, *J. Non-Cryst. Solids* 498 (2018) 470–479.
- [20] Haruka George, Nisha Deopa, Sumandeep Kaur, Aman Prasad, M. Sreenivasulu, M. Jayasimhadri, A.S. Rao, Judd-Ofelt parametrization and radiative analysis of Dy³⁺ ions doped Sodium Bismuth Strontium Phosphate glasses, *J. Lumin.* 215 (2019) 116693.
- [21] Sujita Karki, C.R. Kesavulu, H.J. Kim, J. Kaewkhao, N. Chanthima, S. Kothan, S. Kaewjaeng, Physical, optical and luminescence properties of the Dy³⁺-doped barium borophosphate glasses, *J. Non-Cryst. Solids* 521 (2019) 119483.
- [22] S. Ravangong, N. Chanthima, R. Rajaramakrishna, H.J. Kim, N. Sangwanatee, J. Kaewkhao, Dy³⁺ ions doped (Na₂O/NaF)-Gd₂O₃-P₂O₅ glasses for solid state lighting material applications, *Solid State Sci.* 97 (2019) 105972.
- [23] T. Srihari, C.K. Jayasankar, Fluorescence properties and white light generation from Dy³⁺-doped niobium phosphate glasses, *Opt. Mater.* 69 (2017) 87–95.
- [24] G. Neelima, Venkata Krishnaiah Kummara, C.S. Dwaraka Viswanath, K. Thyagarajan, N. Ravi, T. Jayachandra Prasad, *Ceram. Int.* 44 (13) (2018) 15304–15309.
- [25] S. Cui, J. Massera, M. Lastusaari, L. Hupa, L. Petit, Novel oxyfluorophosphate glasses and glass-ceramics, *J. Non-Cryst. Solids* 445–446 (2016) 40–44.
- [26] K.P. Muller, Struktur und eigenschaften von glasern und glasbildenden schmelzen. Teil III. Untersuchungen über die struktur abgeschreckter alkalibor- und alkaliphosphatgläser mittels infrarot, *Glastechn. Ber.* 42 (1969) 83.
- [27] C. Dayanand, G. Bhikshamaiah, V. Jaya Tyagaraju, M. Salagram, A.S.R. Krishna Murthy, Structural investigations of phosphate glasses: a detailed infrared study of the x(PbO)-(1-x)P₂O₅, vitreous system, *J. Mater. Sci.* 31 (1996) 1945–1967.
- [28] D. Toloman, D.A. Magdas, I. Bratu, L.M. Giurgiu, I. Ardelean, Infrared spectra of calcium phosphate glasses, *Int. J. Mod. Phys. B* 24 (3) (2010) 351–358.
- [29] B.R. Judd, Optical absorption intensities of rare earth ions, *Phys. Rev.* 127 (1962) 750–761.
- [30] G.S. Ofelt, Intensities of crystal spectra of rare earth ions, *J. Chem. Phys.* 37 (1962) 511–520.
- [31] M. Brian, Walsh, Judd-Ofelt theory: principles and practices, *Advances in Spectroscopy for Lasers and Sensing* (2006) 403–433.
- [32] B. Klimesz, G. Dominiak-Dzik, M. Zelechower, W. Ryba-Romanowski, Optical study of GeO₂-PbO-PbF₂ oxyfluoride glass single doped with lanthanide ions, *Opt. Mater.* 30 (2008) 1587–1594.
- [33] C.R. Kesavulu, H.J. Kim, S.W. Lee, J. Kaewkhao, N. Chanthima, Y. Tariwong, Physical, vibrational, optical and luminescence investigations of Dy³⁺-doped yttrium calcium silicoborate glasses for cool white LED applications, *J. Alloys Compd.* 726 (2017) 1062–1071.
- [34] Feifei Huang, Lili Hu, Danping Chen, Observation of 2.8 μm emission from diode-pumped Dy³⁺-doped fluoroaluminate glasses modified by TeO₂ 40 (8) (2014) 12869–12873.
- [35] M. Sundara Rao, V. Sudarsan, M.G. Brik, Y. Gandhi, K. Bhargavi, M. Piasecki, I. V. Kityk, N. Veeraiiah, De-quenching influence of aluminum ions on Y/B ratio of Dy³⁺ ions in lead silicate glass matrix, *J. Alloys Compd.* 575 (2013) 375–381.
- [36] Kamel Damak, El Sayed Yousef, Christian Rüssel, Ramzi Maalej, White light generation from Dy³⁺ doped tellurite glass, *J. Quant. Spectrosc. Radiat. Transfer* 134 (2014) 55–63.
- [37] P. Suthanthirakumar, K. Marimuthu, Investigations on spectroscopic properties of Dy³⁺ doped zinc telluro-fluoroborate glasses for laser and white LED applications, *J. Mol. Struct.* 1125 (2016) 443–452.
- [38] G. Chinna Ram, T. Narendrudu, S. Suresh, A. Suneel Kumar, M.V. Sambasiva Rao, V. Ravi Kumar, D. Krishna Rao, Investigation of luminescence and laser transition of Dy³⁺ ion in P₂O₅-PbO-Bi₂O₃-R₂O₃ (R = Al, Ga, In) glasses, *Opt. Mater.* 66 (2017) 189–196.
- [39] Marta Kuwik, Agata Górny, Joanna Pisarska, A. Wojciech, Pisarski, Lead-based glasses doped with Dy³⁺ ions for W-LEDs, *Mater. Lett.* 254 (2019) 62–64.
- [40] C.R. Kesavulu, C.K. Jayasankar, White light emission in Dy³⁺-doped lead fluorophosphate glasses, *Mater. Chem. Phys.* 130 (2011) 1078–1085.
- [41] M. Inokuti, F. Hirayama, Influence of energy transfer by the exchange mechanism on donor luminescence, *J. Chem. Phys.* 43 (1965) 1978–1989.

- [42] K. Venkata Krishnaiah, K. Upendra Kumara, C.K. Jayasankar, Spectroscopic properties of Dy³⁺-doped oxyfluoride glasses for white light emitting diodes, *Materials Express* 3 (1) (2013) 61–70.
- [43] C.S. McCamy, Correlated color temperature as an explicit, Function of Chromaticity Coordinates 17 (2) (1992) 142–144.
- [44] A. Amarnath Reddy, M. Chandra Sekhar, K. Pradeesh, S. Surendra Babu, G. Vijaya Prakash, Optical properties of Dy³⁺-doped sodium–aluminum–phosphate glasses, *J. Mater. Sci.* 46 (2011) 2018–2023.



Optical and white light emission properties of Dy³⁺ ions doped zinc oxyfluorotellurite glasses

P. Babu^{a,*}, V. Chandrappa^b, N. Vijaya^b, C.K. Jayasankar^{b,**}, Hyo Jin Seo^c

^a Department of Physics, SVCR Government Degree College, Palamaner - 517408, India

^b Department of Physics, Sri Venkateswara University, Tirupati - 517 502, India

^c Department of Physics, Pukyong National University, Busan 608-737, Republic of Korea

ARTICLE INFO

Keywords:

Oxyfluorotellurite glasses
Dy³⁺ ions
Luminescence properties
White light

ABSTRACT

The dysprosium ions-doped zinc oxyfluorotellurite glasses of three different compositions have been synthesized and analyzed their vibrational, thermal, optical and white light emission properties. The differential thermal analysis curves, Fourier Transform Infrared, absorption, emission and excitation spectra and lifetimes from the luminescent level (⁴F_{9/2}) have been measured and analyzed. Absorption spectra have been characterized in the frame of Judd-Ofelt model to determine essential radiative properties namely, transition probabilities, calculated lifetimes and branching ratios of the ⁴F_{9/2} luminescent level. Photoluminescence spectra of the glasses are measured by exciting with 388 nm broad band and 355 nm laser. The glasses emit intense white luminescence with 388 nm broad band excitation. The CIE chromaticity color coordinates of one of the glass are nearer to the equal energy point. Decay time profiles of the ⁴F_{9/2} state are non-exponential for three glasses under study where their effective lifetimes have been evaluated. Quantum efficiencies of the glasses vary from 30 to 62% with change in ZnF₂ content.

1. Introduction

Glass is an interesting material for research and development and as host for rare-earths (RE) because of its wide potential uses as high-power solid state lasers, sensors, and in optical communication, etc. Recently, considerable studies have been focused on the RE³⁺-doped TeO₂ based glasses to enhance their photoluminescence (PL) properties [1,2]. These properties can be tuned by changing the modifier, and/or activator ion concentration in the host glass. Such modifications yield the host network stronger and acquire necessary properties which will have potential applications in the fields of medicine and industry.

Tellurite glasses are potential candidates as hosts for RE³⁺ ions because of their lower phonon energies (700-800 cm⁻¹) and higher refractive indices than those of other oxide glasses (such as borate, phosphate and silicate). These properties are highly useful for higher radiative emission rates of RE³⁺ ions. Further, tellurite glasses have additional merits such as better transparency in the 0.35–6 μm region, better glass stability and RE³⁺ ions doping. Oxyfluoride tellurite glasses are characterized by the favourable properties such as lower phonon energies and a relatively higher thermal stability, higher chemical

durability and ease of preparation. Also, tellurite glasses are useful for fabrication of planar waveguides and optical fibers [1–6]. Rare earth ions-doped tellurite glasses find potential applications as optical devices such as optical fibers, optical amplifiers, display devices, solid state lasers, waveguides, optical modulators and frequency doublers. These matrices have good optical quality and are stable against atmospheric moisture over other oxide glasses [7–12].

The Dy³⁺ ion emits several interesting wavelengths that covers the region from visible to near-infrared (NIR) and are useful for the fabrication of photonic components and devices. The visible emission of Dy³⁺ ion primarily exhibit two strong bands, blue and yellow, corresponding to the ⁴F_{9/2} → ⁶H_{15/2} and ⁴F_{9/2} → ⁶H_{13/2} transitions, respectively. In these, the ⁴F_{9/2} → ⁶H_{15/2} transition is hypersensitive in principle and its intensity vary mainly depending on the nature of host. This gives rise to characteristic yellow (Y)-to-blue (B), (Y/B), intensity ratios which vary significantly with Dy³⁺ ions concentration and/or with glass composition. At a suitable ratio of Y/B, the Dy³⁺ ions will produce white luminescence [13]. The emission at 1.32 μm is useful for application in fiber amplifiers used in optical communication systems [14,15]. Dy³⁺-doped BaYF₅ nanoparticles are found to have potential application as

* Corresponding author.

** Corresponding author.

E-mail addresses: drpbabu@gdcplnr.edu.in (P. Babu), ckjaya@yahoo.com (C.K. Jayasankar).

temperature sensor [13]. Further, the Dy^{3+} ions can emit mid-IR luminescence from 2.9 to 4.4 μm [14–16] with proper excitations.

In view of the importance of tellurite glasses and interesting luminescence properties of Dy^{3+} ions, several authors investigated Dy^{3+} -doped tellurite glasses of different compositions and Dy^{3+} ion concentrations [1–10,20–34]. Kibrisli et al. [2], studied Dy_2O_3 -doped tellurite glasses, with the composition of $50TeO_2-25WO_3-25Li_2O$, for solid state lighting applications through physical, thermal, structural and optical spectroscopy. They concluded that lower Dy_2O_3 content is necessary for an improved colour purity, quantum efficiency and non-radiative transition rate in this glass system. Structural, thermal, optical and white light emission properties of Dy^{3+} -doped titanium-tungstate-tellurite glasses were investigated and found that the glasses were suitable for generation of white light [3]. The Er^{3+} -doped tellurite glasses of the composition, $TeO_2-ZnO-Na_2O-Er_2O_3$, were investigated and found that these were promising materials for laser and optical amplifiers [4].

Heavy metal germanium tellurite glasses containing silver nano particles doped with Dy^{3+} ions were investigated under 454 nm excitation and were found to emit efficient warm yellowish-white light [6]. Tellurite glasses with the composition TeO_2-Tl_2O-ZnO were found to exhibit second harmonic generation [7]. Erbium doped niobic-tungsten-tellurite glasses were investigated [8] for laser and amplifier device applications through thermal stability and spectroscopic properties. Tellurite glasses co-doped with Dy^{3+} and Eu^{3+} ions were studied and were found to be promising for the UV and blue converted white light emitting diodes [9]. Tuyen et al. [10], studied Dy^{3+} -doped alumina lithium telluroborate glasses through JO analysis, spectroscopic and energy transfer properties. They also investigated white light emission properties and found that Y/B ratio depends strongly on the components of host and weakly on the concentration of Dy^{3+} -ions. Several other authors were also investigated RE^{3+} -doped tellurite glasses [17–32] to explore their thermal, structural, optical and white light emission properties.

Present work focuses on the preparation and characterization of Dy^{3+} -doped oxyfluorotellurite glasses via differential thermal analysis (DTA), Fourier Transform Infrared (FTIR), absorption, excitation and emission spectra and lifetime analyses. The obtained results are analyzed and compared with the similar properties of studied Dy^{3+} -glass systems.

2. Experimental details

Three different compositions of Dy^{3+} in oxyfluorotellurite (TZNDy) glasses having a composition (in mol %) of $(74-x) TeO_2 + 20 ZnO + x ZnF_2 + 5 Na_2O + 1 Dy_2O_3$, $x = 0, 10$ and 20 , referred as TZNDy_{1.0}, T10ZofNDy_{1.0} and T20ZofNDy_{1.0} glasses, respectively, were made by traditional melt and sudden quenching method. About 20 g of the batch was mixed well in an agate mortar and thoroughly mixed batch so obtained was kept in a platinum crucible and placed in an high temperature furnace maintained at 860 °C for 1 h. The bubble free and homogenous melt thus obtained was poured on to a preheated stainless steel mould kept at 250 °C and the resulting glass samples were annealed at 250 °C for 6 h to free them from thermal strain and stress. Refractive indices and densities of the samples were determined by Brewster angle and Archimedes' methods, respectively. The thermal properties of the glasses were measured by using DTA at 10 °C/min heating rate under a N_2 atmosphere (TG-DTA 2020, Bruker AXS K.K.). The FTIR spectra were recorded on Nicolet Magna 550 IR spectrometer.

Absorption spectra were recorded using Lambda-950 Perkin Elmer Spectrophotometer. The luminescence spectra were measured using JOBIN YVON Fluorolog-3 Spectrofluorimeter exciting at 388 nm and also using 355 nm line of Nd:YAG (Spectron Laser Sys. SL802G) laser. For laser excitation, the signal was detected through a 0.75 m monochromator (Acton research Corp. Pro-750) by using a PMT (Hamamatsu R928). Lifetimes were evaluated by exciting at 355 nm with LeCroy 9310 digital storage oscilloscope connected to a computer.

3. Theory

The intensities of absorption bands are expressed in terms of experimental oscillator strengths (f_{exp}) by the expression [2,10,12,35],

$$f_{exp} = 4.318 \times 10^{-9} \int \epsilon(\nu) d\nu \quad (1)$$

where $\epsilon(\nu)$ is the molar absorptivity at energy ν (cm^{-1}) which can be obtained by Beer-Lambert's law [10].

Theoretical oscillator strengths (f_{cal}) for the induced electric dipole transition from the ground state to an excited state can be calculated from the Judd-Ofelt (JO) theory using the expression [2,10,12,35],

$$f_{cal} = \frac{8\pi^2 m c \nu}{3h(2J+1)} \frac{(n^2+2)^2}{9n} \sum_{\lambda=2,4,6} \Omega_{\lambda} \|U^{\lambda}\|^2 \quad (2)$$

where J is the total angular momentum of the ground state, n is the refractive index of the material, Ω_{λ} ($\lambda = 2, 4, 6$) are the JO intensity parameters and $\|U^{\lambda}\|^2$ are the squared doubly reduced matrix elements of the unit tensor operator of the rank $\lambda = 2, 4, 6$. These elements are independent of the host and hence are taken from our earlier studies [35].

Radiative properties such as radiative transition probability (A_R), branching ratio (β_R), calculated lifetime (τ_R), peak stimulated emission cross-section ($\sigma(\lambda_p)$) can be calculated from the JO intensity parameters as follows:

Radiative transition probability (A_R) from an initial level, ψJ to a final level $\psi' J'$ can be obtained using the following expression [2,3],

$$A_R(\psi J, \psi' J') = \frac{64\pi^4 e^2 \nu^3}{3h(2J+1)} \left[\frac{n(n^2+2)^2}{9} S_{ed} + n^3 S_{md} \right] \quad (3)$$

where S_{ed} is electric dipole and S_{md} is the magnetic dipole line strengths of a given transition. S_{ed} and S_{md} values can be determined using the expressions [2],

$$S_{ed}(\psi J, \psi' J') = e^2 \left(\sum_{\lambda=2,4,6} \Omega_{\lambda}(\psi J) \|U^{\lambda}\| \|\psi' J'\|^2 \right) \quad (4)$$

$$S_{md}(\psi J, \psi' J') = \left(\frac{e^2}{4m^2 c^2} \right) \Omega_{\lambda}(\psi J) \|L + 2S\| \|\psi' J'\|^2 \quad (5)$$

Calculated branching ratio β_{cal} , can be determined using the following relation [2,3,35],

$$\beta_{cal}(\psi J, \psi' J') = \frac{A_R(\psi J, \psi' J')}{A_T(\psi' J')} \quad (6)$$

where A_T is the total radiative transition probability which is the sum of all A_R values from an excited state. The experimental branching ratio β_{exp} , values are determined from the ratio of integrated area of corresponding emission band to the total integrated area of emission.

The calculated lifetime of an excited state can be evaluated using the relation [2,35],

$$\tau_{cal} = \frac{1}{A_T(\psi' J')} \quad (7)$$

Peak stimulated emission cross-section, $\sigma(\lambda_p)$, can be calculated for each emission peak wavelength using the expression [2,3,35],

$$\sigma(\lambda_p)(\psi J, \psi' J') = \frac{\lambda_p^4}{8\pi c n^2 \Delta\lambda_{eff}} A_R(\psi J, \psi' J') \quad (8)$$

where $\Delta\lambda_{eff}$ is the effective bandwidth of corresponding emission band calculated by deviding the band area by height.

4. Results and discussion

4.1. Physical and thermal properties

Physical properties of the TZNDy glasses such as densities (d), concentration (C) of Dy^{3+} ions and refractive indices (n) are presented in Table 1. As can be seen, 'd' and 'n' values follow the same trend of increase from TZNDy_{1.0} to T10ZofNDy_{1.0} and then decrease for T20ZofNDy_{1.0}. The 'd' and 'n' values of TZNDy are slightly lower compared to those of 49TeO₂ + 25WO₃ + 25Li₂O + 1Dy₂O₃ (TWLDy_{1.0}) [2] and 74TeO₂ + 10TiO₂ + 15WO₃ + 1Dy₂O₃ (TTiWdy_{1.0}) [3] glasses.

Differential thermal analysis profiles of TZNDy glasses are depicted in Fig. 1. Glass transition (T_g) and onset of crystallization (T_x) temperature, and the difference between T_x and T_g (called thermal stability factor, $\Delta T = T_x - T_g$) of TZNDy glasses are shown in Fig. 1 and also in Table 1. It is found that, with the replacement of TeO₂ by ZnF₂ from 0 to 20 mol %, both T_g and T_x are gradually increased whereas the value of ΔT decreased from 122 to 119 °C. The thermal stability factor ΔT is one of the most important criterion for fiber drawing. The larger the value of ΔT , better the glass stability [23]. Larger value of ΔT minimizes the scattering loss caused by the crystallization of drawn fiber [3]. In general, glass host with $\Delta T > 100$ °C is suitable for drawing conventional fiber. The present results indicate that the TZNDy_{1.0} glass has a better glass forming ability than the other glasses and is suitable for fiber drawing and for other optical devices.

4.2. FTIR spectral analysis

The FTIR spectral analysis is one of the spectroscopic techniques used to study the structure of the glasses. Fig. 2 illustrates the FTIR spectra of TZNDy glasses. As can be seen, five FTIR bands peaking at 460, 702, 1045, 1635 and 3490 cm^{-1} are observed distinctly. These peaks are found to be almost at the same positions for all the present glasses indicating that there may not be any change in structure of the glass with the increase of ZnF₂ content. The broad band at 3490 cm^{-1} corresponds to the OH stretching (ν_{OH}). This band may be due to presence of the inclusion of water molecules in the pores [24]. The band in the range of 445–465 cm^{-1} belong to the symmetrical stretching and bending modes of continuous chains of corner sharing sites of TeO₃, TeO₄ and TeO₃₊₁ polyhedra [25,26]. This indicates that in these glasses, the vibrations of the Te–O–Te linkage are caused by the transformation of TeO₄ into TeO₃ groups. The band at 702 cm^{-1} corresponds to the asymmetric vibrations of the continuous network structure by the joining of TeO₄ trigonal bipyramids and Te–O–Te bond consisting of a long short Te–O bond [27]. Two overtones of peaks at 460 and 702 cm^{-1} are observed at around 1090 and 1635 cm^{-1} , respectively.

4.3. Absorption spectra and Judd-Ofelt analysis

Absorption spectra of the TZNDy glasses along with their band assignments in the wavelength range of 400–1950 nm are given in Fig. 3. The peaks originate from the ground level, $^6H_{15/2}$ to different excited states (shown in Fig. 3) belong to the $4f^9$ (Dy^{3+}) electronic configuration. As can be seen, the profile and the peak position of each transition remain unchanged with the addition of ZnF₂ content. The absorption level peaked at 1281 nm, corresponds to the $^6H_{15/2} \rightarrow ^6F_{11/2}$ transition,

Table 1

Densities (d , $g\text{cm}^{-3}$), concentrations (C , $\times 10^{20}$ ions/cc), refractive indices (n), glass transition temperature (T_g , °C), onset of crystallization temperature (T_x , °C) and glass stability factors ($\Delta T = T_x - T_g$, °C) of TZNDy glasses.

Glass Label	d	C	n	T_g	T_x	$\Delta T = T_x - T_g$
TZNDy _{1.0}	4.63	1.975	1.96	292	414	122
T10ZofNDy _{1.0}	4.81	2.136	2.00	296	416	120
T20ZofNDy _{1.0}	4.50	2.181	1.89	309	428	119

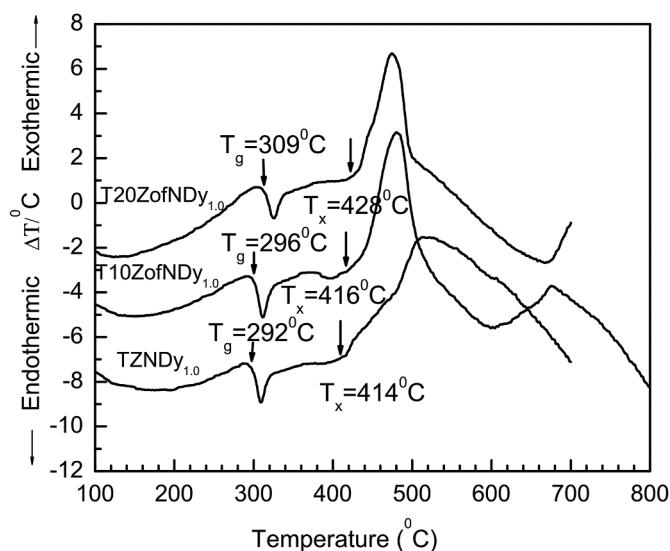


Fig. 1. DTA curves of TZNDy glasses.

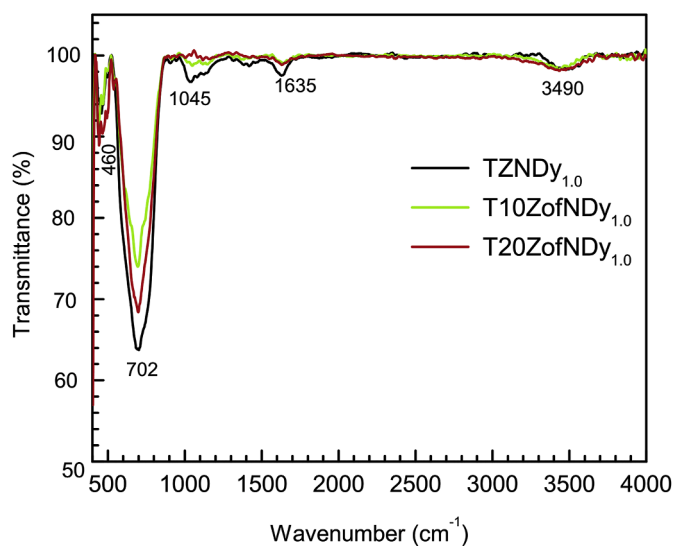


Fig. 2. FTIR spectra of TZNDy glasses.

is dominant and obeys the selection rule, $|\Delta L| \leq 2$, $|\Delta S| = 0$ and $|\Delta J| \leq 2$. This is called hypersensitive transition (HST) and its intensity is more sensitive to the local environment surrounding the Dy^{3+} ions.

At first, the experimental oscillator strengths (f_{exp}) for the absorption transitions of Dy^{3+} ion are determined from the absorption spectrum by calculating the integrated area of each absorption band following the procedure described in our earlier works [36]. The JO model [37,38] has been used to evaluate the calculated (f_{cal}) oscillator strengths. The f_{exp} and f_{cal} values of all absorption peaks for the present TZNDy glasses along with other reported tellurite based glasses [2,3,28–30] are presented in Table 2. As can be seen, the magnitude of oscillator strength is higher for the $^6H_{15/2} \rightarrow ^6F_{11/2}$ transition as it is a HST. The f_{exp} values of HSTs of TZNDy glasses varies with glass composition as $T10ZofNDy_{1.0} > T20ZofNDy_{1.0} > TZNDy_{1.0}$ and are higher than those of the reported Dy^{3+} glasses [2,3,28,29]. These variations in f_{exp} values of HSTs are due to change in environment in the vicinity of the Dy^{3+} ions in the glasses. For other transitions, f_{exp} values of the titled glass systems are comparable to those of reported ones. Finally, three important parameters, called JO (Ω_λ , $\lambda = 2, 4$ and 6) parameters are calculated from the electric-dipole and magnetic-dipole components of f_{exp} and f_{cal} using

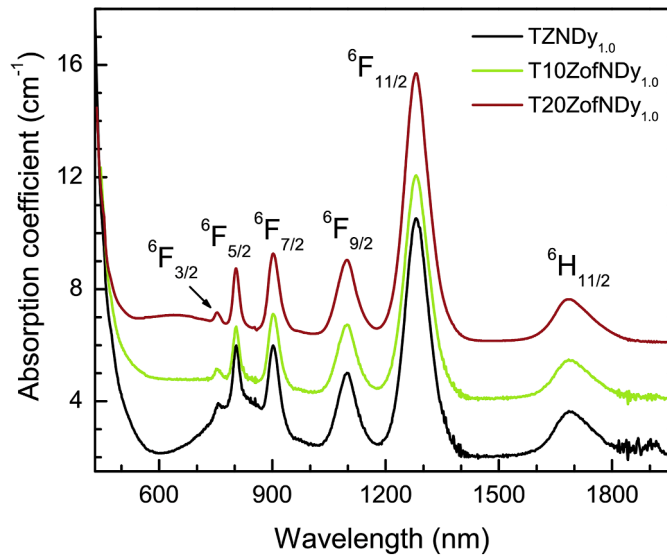


Fig. 3. Optical absorption spectra of Dy³⁺ ions in TZNDy glasses.

least squares fitting approach for all the three TZNDy glasses and are presented in Table 3.

The JO parameters are very useful to evaluate the local structural geometry and bonding nature in the surroundings of RE³⁺ ions. The JO parameters of TZNDy glasses are shown in Table 3 along with those of studied Dy³⁺-doped tellurite based glasses: TWLDy_{1.0} [2], TTIWDy_{1.0} [3], 39H₃BO₃ + 30TeO₂ + 30PbF₂ + 1Dy₂O₃ (BTPfDy_{1.0}) [28], 76TeO₂ + 10ZnO + 9PbO + 1PbF₂ + 3Na₂O + 1Dy₂O₃ (TZPofNDy_{1.0}) [29], 60TeO₂ + 12Pb₂O₅ + 20ZnF₂ + 3Nb₂O₅ + 5Dy₂O₃ (TPbZfNbDy_{5.0}) [30], 59B₂O₃ + 10TeO₂ + 15CaO + 10Nb₂O₅ + 5ZnO + 1Dy₂O₃ (BTCNbZDy_{1.0}) [31] and 40TeO₂ + 29B₂O₃ + 15MgO + 15K₂O + 1Dy₂O₃ (TBMKDY_{1.0}) [32]. Generally, the parameter Ω₂ is related to the effects of short-range coordination and the other parameters Ω₄ and Ω₆ depend on the effect of long-range. The Ω₂ is a measure of the symmetry of ligand field in any glass host. The Ω₂ value depends on the covalence nature of RE-ligand bond while Ω₆ is inversely proportional to the covalence of RE-ligand bond and it also measure the rigidity of the host matrix [33,34]. The JO parameters follow the similar trend as Ω₂ > Ω₄ > Ω₆ for both T10ZofNDy_{1.0} and T20ZofNDy_{1.0} glasses, whereas they follow Ω₂ > Ω₆ > Ω₄ trend for TZNDy_{1.0} glass indicating that the addition of ZnF₂ changes the surrounding ligand field of Dy³⁺:glass. The larger value of Ω₂ is an indication for the higher asymmetry and covalency of local environment around the Dy³⁺ ions [33]. From Table 3, one can notice that the magnitude of Ω₂ (x10⁻²⁰ cm²) increases from 5.94 to 11.62 with the increase in ZnF₂ component from 0 to 20 mol %. Moreover, larger variation in Ω₂ parameter indicates its strong dependence on the surroundings of the Dy³⁺ ion than the other two parameters (Ω₄ and Ω₆). The value of Ω₂ in T20ZofNDy_{1.0} glass is found to be higher than those of TZNDy_{1.0} and T10ZofNDy_{1.0} glasses as well as those of reported Dy³⁺:glasses [2,3,28–32] shown in Table 3, indicating the

existence of higher covalance between Dy³⁺ ion and surrounding ligand environment. On the other hand the Ω₄ and Ω₆ magnitude in the titled glass systems are comparable to those of the reported ones in Table 3.

Using the refractive index and JO parameters, important radiative characteristics such as transition probabilities (A), branching ratios (β_R) and lifetimes (τ_R) associated with transitions from the ⁴F_{9/2} luminescent level to the next lower lying ⁶H_J (J = 11/2, 13/2 and 15/2) levels are evaluated for all the TZNDy glasses and are presented in Table 4. From Table 4, one can see that, ‘A’ value of the ⁴F_{9/2} → ⁶H_{11/2} level is the highest compared to those of other two levels indicating its highest transition probability which is reflected in the emission spectrum, where the band corresponding to this transition is most intense. For all the three transitions, maximum ‘A’ values are found for T10ZfNDy_{1.0} glass and minimum values for TZNDy_{1.0} glass. The calculated β_R values for all the three TZNDy glasses are in the order of ⁴F_{9/2} → ⁶H_{11/2} < ⁴F_{9/2} → ⁶H_{15/2} < ⁴F_{9/2} → ⁶H_{13/2}. The quantity of radiative (calculated) lifetimes

Table 3
Judd-Ofelt parameters (Ω_λ±5%, x10⁻²⁰ cm²) of TZNDy glasses along with those of some reported Dy³⁺:glasses.

Glass	Ω ₂	Ω ₄	Ω ₆	Trend
TZNDy _{1.0} [Present work]	5.94	1.39	1.87	Ω ₂ > Ω ₆ > Ω ₄
T10ZofNDy _{1.0} [Present work]	10.56	3.00	2.95	Ω ₂ > Ω ₄ > Ω ₆
T20ZofNDy _{1.0} [Present work]	11.62	2.88	2.48	Ω ₂ > Ω ₄ > Ω ₆
TWLDy _{1.0} [2]	5.90	0.93	1.22	Ω ₂ > Ω ₆ > Ω ₄
TTIWDy _{1.0} [3]	3.37	0.30	1.07	Ω ₂ > Ω ₆ > Ω ₄
BTPfDy _{1.0} [28]	7.75	2.31	2.70	Ω ₂ > Ω ₆ > Ω ₄
TZPofNDy _{1.0} [29]	5.66	0.84	2.17	Ω ₂ > Ω ₆ > Ω ₄
TPbZfNbDy _{5.0} [30]	2.32	0.64	4.64	Ω ₂ > Ω ₆ > Ω ₄
BTCNbZDy _{1.0} [31]	11.30	3.30	2.60	Ω ₂ > Ω ₄ > Ω ₆
TBMKDY _{1.0} [32]	9.23	1.15	1.56	Ω ₂ > Ω ₆ > Ω ₄

Table 4
Effective bandwidths (Δλ_{eff} ±0.1, nm) of the emission bands under 355 nm excitation, radiative transition probabilities (A_R±2%, s⁻¹), peak stimulated emission cross-sections (σ(λ_p)±0.2, × 10⁻²¹ cm²), experimental and calculated branching ratios (β_R±2%) for the ⁴F_{9/2} → ⁶H_J (J = 11/2, 13/2,15/2) transitions and radiative lifetime (τ_R±2%, μs) of the ⁴F_{9/2} level of Dy³⁺ ions in TZNDy glasses.

Glass Transition	Δλ _{eff}	A	σ(λ _p)	β _R		τ _R
				Exp.	Cal.	
TZNDy_{1.0}						
⁶ H _{11/2}	12.23	155	0.86	0.03	0.08	483
⁶ H _{13/2}	10.83	1299	4.52	0.64	0.73	
⁶ H _{15/2}	12.26	333	5.97	0.33	0.19	
T10ZofNDy_{1.0}						
⁶ H _{11/2}	12.80	589	1.40	0.03	0.08	267
⁶ H _{13/2}	10.91	2445	8.13	0.62	0.74	
⁶ H _{15/2}	12.26	589	0.86	0.35	0.18	
T20ZofNDy_{1.0}						
⁶ H _{11/2}	11.21	240	1.56	0.02	0.09	326
⁶ H _{13/2}	10.95	2059	7.64	0.62	0.76	
⁶ H _{15/2}	12.79	411	0.69	0.36	0.15	

Table 2

Absorption levels, band positions (λ_p, nm), experimental (f_{exp}) and calculated (f_{cal}) oscillator strengths (× 10⁻⁶) of TZNDy glasses and experimental oscillator strengths of some reported Dy³⁺:glasses. All the transitions are from the ground state, ⁶H_{15/2}.

Level	λ _p	TZNDy _{1.0}		T10ZofNDy _{1.0}		T20ZofNDy _{1.0}		TWLDy _{1.0} [2]	TTIWDy _{1.0} [3]	BTPfDy _{1.0} [28]	TZPofNDy _{1.0} [29]	TPbZfNbDy _{5.0} [30]
		f _{exp}	f _{cal}	f _{exp}	f _{cal}	f _{exp}	f _{cal}					
⁶ H _{11/2}	1685	1.12	1.42	2.08	2.42	1.76	2.08	1.59	0.61	1.27	1.53	2.29
⁶ H _{9/2,1,11/2}	1281	7.70	7.66	14.44	14.39	13.86	13.82	6.53	4.74	6.76	7.31	4.04
⁶ H _{7/2,1,9/2}	1098	2.46	2.57	4.60	4.75	3.76	3.89	1.49	1.18	2.65	2.81	4.90
⁶ F _{7/2}	902	2.54	2.22	4.30	3.78	3.37	2.94	0.77	1.68	2.16	2.48	2.10
⁶ F _{5/2}	804	0.56	1.05	2.20	1.72	1.86	1.30	0.34	0.10	1.38	1.69	0.28
⁶ F _{3/2}	752	1.18	0.20	0.46	0.32	0.37	0.25	0.06	0.29	0.19	0.23	0.21
δ _{rms}		±0.49		±0.33		±0.33						

of the $^4F_{9/2}$ level first decreases and then increases with increase in ZnF_2 component. This could be caused by the structural modifications in the surrounding of the Dy^{3+} ions.

4.4. Luminescence properties

Selection of proper excitation wavelength is an important parameter to analyze the emission properties of any RE^{3+} ion. The absorption spectrum of present Dy^{3+} -doped glasses do not show any bands in ultraviolet–visible region because of the dominant absorption of tellurite host in this region. Excitation spectrum, measured in the range of 300–550 nm for the T20ZofNDy_{1.0} glass, monitoring the well known emission of the Dy^{3+} ion at 577 nm which belongs to the $^4F_{9/2} \rightarrow ^4H_{13/2}$ level, is shown in Fig. 4. The excitation peaks centered at 351, 367, 387, 428, 454 and 473 nm are attributed to the $^6H_{15/2} \rightarrow ^6P_{7/2}$, $^4P_{3/2}$, $^4I_{13/2}$, $^6G_{11/2}$, $^4I_{15/2}$ and $^4F_{9/2}$ levels, respectively. It is well-known that excitation energy corresponding to the intense excitation peak can give better luminescence. The excitation bands peaked at 354, 388 and 453 nm are found to be most intense in UV–visible region. However, our experimental facilities are limited to UV excitation only. Hence, the luminescence spectra are recorded using 355 nm and 388 nm excitation wavelengths.

Photoluminescence (PL) spectra of TZNDy are measured in the spectral region of 430–700 nm with 388 nm broad band and 355 nm laser excitations and are shown in Figs. 5 and 6, respectively. The luminescence spectra show principal characteristic emission peaks of Dy^{3+} ion consisting of the band, $^4F_{9/2} \rightarrow ^6H_{15/2}$ at 482 nm (due to magnetic-dipole) and the band $^4F_{9/2} \rightarrow ^6H_{13/2}$ at 575 nm (due to electric-dipole) and a relatively feeble band, $^4F_{9/2} \rightarrow ^6H_{11/2}$ at 666 nm. It is well known that the yellow emission of Dy^{3+} belongs to the HST follows the selection rule $|\Delta J| \leq 2$, and is highly sensitive to the surroundings of the active Dy^{3+} ions. The blue emission marginally varies with the crystal-field effect surrounding the Dy^{3+} ion. When Dy^{3+} is kept in a low-symmetry local site, the yellow emission usually dominates in the emission spectrum, and when it is in a high-symmetry site, the blue emission dominates in the de-excitation spectrum [39,40]. Further, higher Y/B ratio is an indication for the higher degree of covalency between Dy^{3+} ion and surrounding oxygen ions [37]. The Y/B ratios for TZNDy glasses, under 388 and 355 nm excitations are evaluated and are presented in Table 5. From Table 5, Y/B ratios of the present glass systems are <1 for broadband excitation and ~ 2 for 355 nm laser excitation. The Y/B ratios of TZNDy are compared to those of reported 1.0 mol

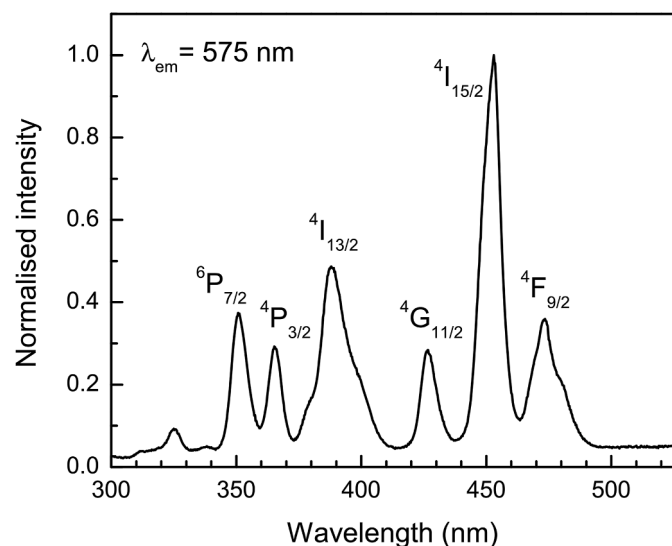


Fig. 4. Excitation spectrum of T20ZofNDy_{1.0} glass monitoring the 577 nm emission.

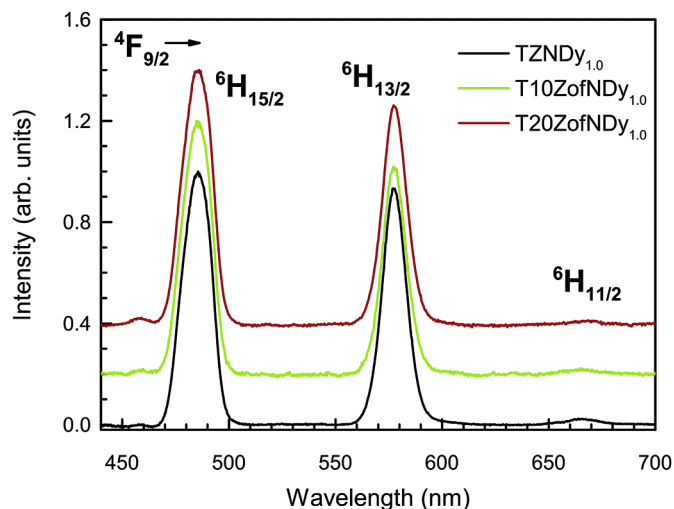


Fig. 5. Luminescence spectra of TZNDy glasses under 388 nm broadband excitation.

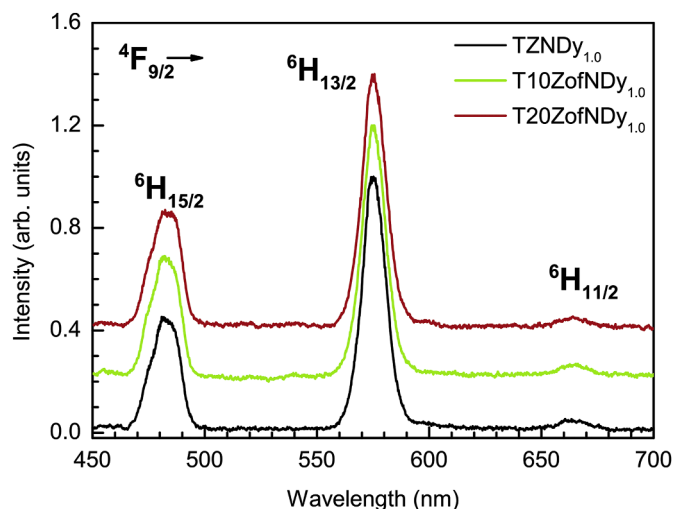


Fig. 6. Luminescence spectra of TZNDy glasses under 355 nm laser excitation.

% Dy^{3+} -doped glasses [1–3,29,31], $41P_2O_5 + 17K_2O + 8Al_2O_3 + 23ZnF_2 + 10LiF + 1Dy_2O_3$ (PKAZFLfDy_{1.0}) [41], $30KH_2PO_4 + 24(NaPO_3)_6 + 25TiO_2 + 20CaCl_2 + 1Dy_2O_3$ (PKNTiClDy_{1.0}) [42], $30KH_2PO_4 + 24(NaPO_3)_6 + 25TiO_2 + 20SrCl_2 + 1Dy_2O_3$ (PKNTiSiDy_{1.0}) [42], $(60-x)TeO_2 + 25WO_3 + 15PbF_2 + 1Dy_2O_3$ (TWPfDy_{1.0}) [43], $46.7SiO_2 + 35.9BaO + 1.0Al_2O_3 + 4.03(Li_2O + Na_2O + K_2O) + 11.22Y_2O_3 + 1.15Dy_2O_3$ (SBALNKYDy_{1.15}) [44] in Table 5. Among the reported glasses shown in Table 5, laser excitation was used only for TTiWDy_{1.0} [3] and TZPofNDy_{1.0} [29] and for the remaining systems, broadband excitation was used.

From the PL spectra, other radiative properties such as experimental branching ratio, effective bandwidth ($\Delta\lambda_{eff}$), and stimulated emission cross-sections ($\sigma(\lambda_p)$) for the $^4F_{9/2} \rightarrow ^6H_{11/2,13/2,15/2}$ transitions of TZNDy glasses are determined and are presented in Table 4. From Table 4, one can see that, $\Delta\lambda_{eff}$ values of the $^4F_{9/2} \rightarrow ^6H_{13/2}$ band are lower compared to those of other two bands. Also, the values of $\sigma(\lambda_p)$ and calculated branching ratios (β_{cal}) for the $^4F_{9/2} \rightarrow ^6H_{13/2}$ (HST) are higher than those of other transitions. Moreover, the $\sigma(\lambda_p)$ ($\times 10^{-21} \text{ cm}^2$) value of this HST changes from 4.52 to 8.13 with change in ZnF_2 content. The luminescence branching ratio is one of the crucial parameter that indicates the lasing nature of a transition and it was shown that an emission level with $\beta_R \geq 60\%$ is relatively more potential for laser

Table 5

Yellow to blue intensity ratios (Y/B), chromaticity color coordinates (x, y) and correlated color temperature (CCT, K) of TZNDy glasses under 388 nm broadband and 355 nm laser excitations and those of some reported 1.0 mol % Dy³⁺-doped glasses.

System	Y/B	Chromaticity co-ordinates		CCT (K)
		x	Y	
388 nm Excitation				
TZNDy _{1.0}	0.83	0.341	0.387	5222
T10ZofNDy _{1.0}	0.71	0.321	0.366	5950
T20ZofNDy _{1.0}	0.74	0.325	0.372	5782
355 nm Excitation				
TZNDy _{1.0}	1.93	0.394	0.429	4003
T10ZofNDy _{1.0}	1.77	0.390	0.420	4040
T20ZofNDy _{1.0}	1.76	0.385	0.427	4187
Reported				
TWLDy _{1.0} [2]	2.40	0.38	0.43	4221
TTiWDy _{1.0} [3]	2.02	0.38	0.41	–
TZPofNDy _{1.0} [29]	0.88	0.38	0.43	4312
BTCNbZDy _{1.0} [31]	0.65	0.31	0.36	6439
PKAZfNdY _{1.0} [41]	0.77	0.32	0.37	5992
PKNTiCIDy _{1.0} [42]	1.23	0.33	0.34	5609
PKNTiSIDy _{1.0} [42]	1.38	0.33	0.34	5609
TWPFdy _{1.0} [43]	1.02	0.34	0.40	5270
SBALNKDY _{1.15} [44]	2.03	0.385	0.437	4233

action. As can be seen from Table 4, there is reasonably good coincidence between calculated and experimental β_R values which indicates the accuracy of the calculations. The value of β_R (both experimental and calculated) for the ⁴F_{9/2} → ⁶H_{13/2} level in all the TZNDy glasses is estimated to be >60%, showing the suitability of present glass systems for lasing applications at this wavelength.

The Δλ_{eff}, σ(λ_p) and β_{cal} of the ⁴F_{9/2} → ⁶H_{13/2} level as well as radiative predicted lifetime (τ_R) of the ⁴F_{9/2} luminescent state of Dy³⁺ ion in various tellurite based glasses [3,28–32] are compared in Table 6. As can be seen, relatively larger value of σ(λ_p) for ⁴F_{9/2} → ⁶H_{13/2} channel in T10ZofNDy_{1.0} glass, compared to already studied Dy³⁺-glasses, indicate that this glass is a suitable gain media for potential laser emission in yellow spectral region. The value of τ_R is found to decrease from 483 to 267 and then increase to 326 μs when ZnF₂ increased from 0 to 20 mol % and these values are comparable with other reported glasses [29,30] shown in Table 6. Out of all the Dy³⁺:tellurite glasses [3,28–32] compared in Table 6, TZNDy glasses show lower Δλ_{eff} and higher σ(λ_p) values. The β_{cal} values of TZNDy glasses are higher than all the compared glass systems except that of BTCNbZDy_{1.0} [31] glass. Calculated lifetimes of the ⁴F_{9/2} state in the present glasses are comparable to those of TZPofNDy_{1.0} [29] and TPbZfNdY_{5.0} [30] glasses and are less than those

Table 6

Effective bandwidths (Δλ_{eff}±0.1, nm) of the emission bands under 355 nm excitation, stimulated emission cross-section (σ(λ_p)±0.2, x 10⁻²¹ cm²) and calculated branching ratio (β_{cal}) of ⁴F_{9/2} → ⁶H_{13/2} transition, radiative lifetime (τ_R±2%, μs) of the ⁴F_{9/2} level, gain bandwidth (σ(λ_p) x Δλ_{eff}), x10⁻²⁷ and optical gain (σ(λ_p) x τ_R), x10⁻²⁴ of the ⁴F_{9/2} level of Dy³⁺ ions in various tellurite based glasses.

Glass	Δλ _{eff}	σ	β _{cal}	τ _R	σ(λ _p) x Δλ _{eff}	σ(λ _p) x τ _R
TZNDy _{1.0} [Present work]	10.83	4.52	0.73	483	4.90	2.18
T10ZofNDy _{1.0} [Present work]	10.91	8.13	0.74	267	8.87	2.17
T20ZofNDy _{1.0} [Present work]	10.95	7.64	0.76	326	8.37	2.49
TTiWDy _{1.0} [3]	16	2.4	0.53	–	3.84	–
BTPFDy _{1.0} [28]	16	2.86	0.63	–	4.58	–
TZPofNDy _{1.0} [29]	14.56	4.07	0.63	374	5.93	1.52
TPbZfNdY _{5.0} [30]	–	–	0.61	453	–	–
BTCNbZDy _{1.0} [31]	17.06	3.22	0.83	999	5.49	3.22
TBMKDY _{1.0} [32]	13.11	6.05	0.69	778	7.93	2.51

of BTCNbZDy_{1.0} [31] and TBMKDY_{1.0} [32] glasses.

The parameters, optical gain (σ(λ_p) × τ_R) and gain bandwidth (σ(λ_p) × Δλ_{eff}) are very essential ones to predict the amplification of the RE³⁺ ions doped medium. An optical amplifier is characterized by higher quantities of gain bandwidth and optical gain [31]. As can be noticed from Table 6, σ(λ_p) × τ_R and σ(λ_p) × Δλ_{eff} of the titled TZNDy are nearer to those of the Dy³⁺:tellurites [3,28–32]. Out of all the glasses compared in Table 6, T10ZofNDy_{1.0} and T20ZofNDy_{1.0} glasses show higher values of gain bandwidth.

4.5. CIE chromaticity coordinates

The emission spectrum of Dy³⁺ ion under UV excitation exhibits two prominent bands in the blue and yellow regions. By properly adjusting the intensities of these bands one can generate the white luminescence. In view of this, an attempt is made to measure luminescence from TZNDy glasses by changing the excitation wavelength. Emission spectra of TZNDy glasses are recorded by exciting at 388 nm broadband and 355 nm laser excitations and are shown in Figs. 5 and 6, respectively. From Figs. 5 and 6, one can see that the blue band is dominant under broadband excitation whereas the yellow band is found to be more intense than blue under laser excitation. This clearly indicates that the symmetry sites occupied Dy³⁺ can be changed by excitation source also rather than changing the composition.

The white light emission properties of TZNDy glasses are examined with the help of chromaticity co-ordinate of colors under different excitation sources. These co-ordinates are obtained by converting the luminescence spectra of present glasses into standard CIE 1931 chromaticity co-ordinate graphs. The obtained graphs of colour are listed in Table 5 and located in chromaticity frame shown in Fig. 7. As can be seen, the co-ordinates falls in yellow region under 355 nm laser excitation. But intense white luminescence is noticed when the glasses are excited with 388 nm radiation. The CIE color co-ordinates of TZNDy glasses along with other reported 1.0 mol % Dy³⁺-doped glasses [1–3, 29,31,41–44] are presented in Table 5. From Table 5, the evaluated co-ordinates of colour for the present glasses (for 388 nm excitation) are very nearer to white light illuminate and are comparable to those of studied Dy³⁺:glasses. Further, the color coordinates of T20ZofNDy_{1.0}

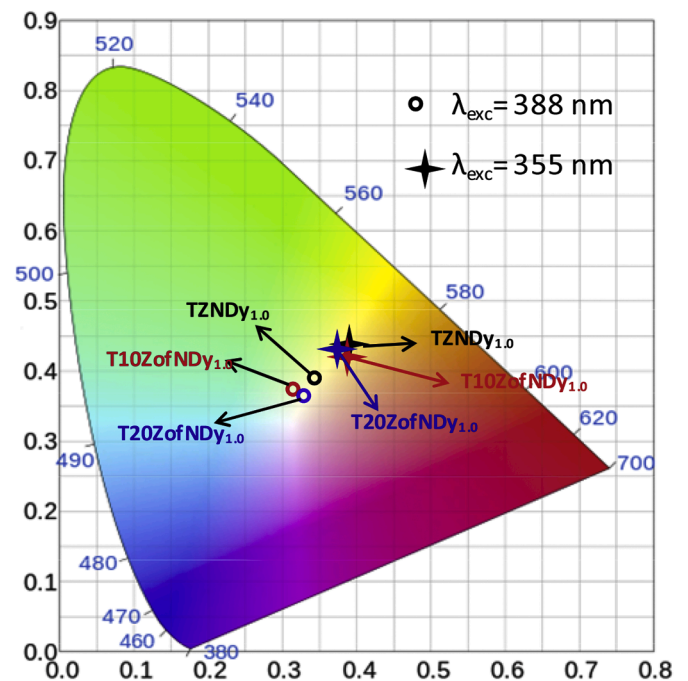


Fig. 7. CIE 1931 chromaticity diagram showing the chromaticity coordinates (x, y) of TZNDy glasses under 355 nm and 388 nm excitations.

glass (0.33, 0.37) are very nearer to the equal energy position (0.33, 0.33).

The quality of the light source is generally assessed by calculating correlated color temperature (CCT) [8], which indicates the temperature of a nearest Planckian black-body radiator to the operating position in the chromaticity graphical representation. The CCT values are determined based on the color coordinators through the Mc Camy's Eq. [45],

$$CCT = -449n^3 + 3525n^2 - 6823n + 5520.33 \quad (9)$$

Here $n = (x-x_e)/(y-y_e)$ indicates the inverse slope line where $x_e = 0.332$ and $y_e = 0.186$ relates the epicenter. The CCT values of the present glasses are calculated for 388 and 355 nm excitations and are collected in Table 5 along with the reported values of 1.0 mol % Dy^{3+} -doped glasses [2,3,29,31,41–44]. The CCT quantities calculated with 388 nm broadband source are closer to that of normal day light (5500 K) and those with 355 nm laser excitation are nearer to that of fluorescent tube (3935 K) [46]. From Table 5, CCT values of reported glass systems of TWLDy_{1.0} [2], TZPofNDy_{1.0} [29] and SBALNKYDy_{1.15} [44] are nearer to that of fluorescent tube and the rest of the systems [1,31,41–43] are nearer to that of day light.

4.6. Decay curves

Decay curves of the $^4F_{9/2}$ state of Dy^{3+} ion in TZNDy glasses are recorded by exciting with 355 nm laser and observing the emission at 577 nm which are presented in Fig. 8. All the decay profiles exhibit non-exponential behaviour and hence, the average lifetime (τ) is determined using the below Eqn.,

$$\tau_{exp} = \frac{\int tI(t)dt}{\int I(t)dt} \quad (10)$$

and are found to be 145, 166 and 163 μ s for TZNDy_{1.0}, T10ZofNDy_{1.0} and T20ZofNDy_{1.0} glasses, respectively. It is observed that there is no significant variation in experimental lifetimes with increase in ZnF₂ content from 10 to 20% where as significant variation is noticed for the radiative lifetime. The quantum efficiency is expressed as the ratio of number of emitted to the absorbed photons. In the case of RE³⁺ ions-doped systems, it is taken as the ratio of τ_{exp} to τ_R for the given states ($\eta = \frac{\tau_{exp}}{\tau_R} \times 100$). The quantity of η for the $^4F_{9/2}$ state of Dy^{3+} in the present TZNDy_{1.0}, T10ZofNDy_{1.0} and T20ZofNDy_{1.0} glasses are found to be 30, 62 and 50, respectively. Out of the three glasses, ' η ' is maximum (62) for the T10ZofNDy_{1.0} glass and minimum (30%) for the TZNDy_{1.0} glass. The ' η ' values of the present Dy^{3+} glasses are comparable to those of the studied ones, PKAZfNdY_{1.0} (55) [41] and TWLDy_{1.0} (61) [2] but less than that of TTiWDy_{1.0} (90) glass [3].

5. Conclusions

Thermal, structural, optical and white light emission properties of TZNDy glasses have been systematically investigated using DTA curves, FTIR, absorption, excitation and emission spectra and decay times. It is found that thermal stability factor decreases from 122 to 119 °C with the replacement of TeO₂ by ZnF₂ from 0 to 20 mol %. By applying the Judd-Ofelt model to the absorption spectra of TZNDy glasses, three JO parameters are evaluated and are in turn used to predict the radiative properties of the emitting level, $^4F_{9/2}$, such as radiative transition probabilities, branching ratios, calculated lifetimes and peak stimulated emission cross-sections. From the emission spectra, obtained with 388 nm excitation, experimental branching ratios are evaluated and are found to be in good agreement with the calculated ones. The CIE chromaticity co-ordinates of colour are determined from the emission spectra. It is found that the titled glasses emit bright white light under

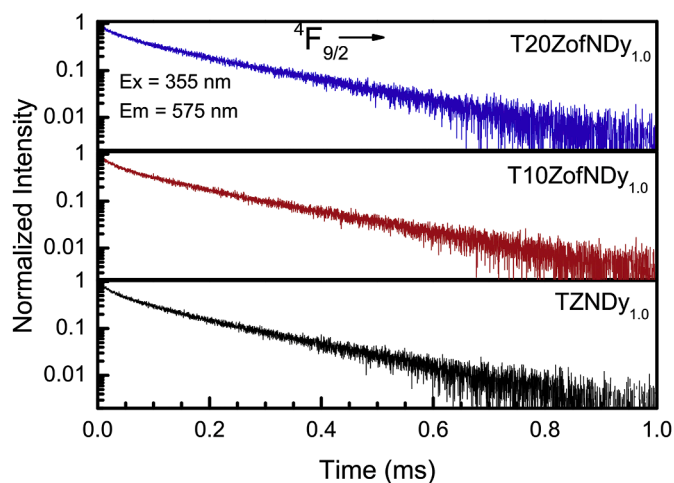


Fig. 8. Decay curves for the $^4F_{9/2}$ level of Dy^{3+} ions in TZNDy glasses.

388 nm broadband excitation. Among the glass systems studied, the color coordinates of the T20ZofNDy_{1.0} glass are very nearer to the equal energy point. The decay curves of the $^4F_{9/2}$ state of Dy^{3+} ions show non-exponential behavior for the studied glasses. Quantum efficiency for the $^4F_{9/2}$ state is found to be maximum for the T10ZofNDy_{1.0} glass. The results obtained in the present study can find potential applications in the design of optical display devices.

CRedit author statement

P. Babu, Conceptualization, Investigation, Writing - Writing - original draft. V. Chandrappa, Methodology, Investigation. N. Vijaya, Formal analysis, Investigation. C.K. Jayasankar, Resources, Writing - Writing - review & editing. Hyo Jin Seo, Resources, Supervision.

Declaration of competing interest

The authors declare that they have no known competing financial interests or personal relationships that could have appeared to influence the work reported in this paper.

Acknowledgement

One of the authors, C.K. Jayasankar is grateful to UGC, New Delhi, for awarding BSR Faculty Fellowship (No.F.18-1/2011 (BSR)) and DAE-BRNS, Mumbai for sanctioning Major Research Project (No.2009/34/36/BRNS/3174).

References

- [1] M. Walas, A. Pastwa, T. Lewandowski, A. Synak, I. Grycznski, W. Sadowski, B. Koscielska, Luminescent properties of Ln³⁺ doped tellurite glasses containing AlF₃, Opt. Mater. 59 (2016) 70–75, <https://doi.org/10.1016/j.optmat.2016.01.040>.
- [2] O. Kibrisli, A.E. Ersundu, M. Celikbilek Ersundu, Dy³⁺ doped tellurite glasses for solid state lighting: an investigation through physical, thermal, structural and optical spectroscopy studies, J. Non-Cryst. Solids 513 (2019) 125–136, <https://doi.org/10.1016/j.jnoncrysol.2019.03.020>.
- [3] L. Jyothi, G. Upender, R. Kuladeep, D. Narayana Rao, Structural, thermal, optical properties and simulation of white light of titanium-tungstate-tellurite glasses doped with dysprosium, Mater. Res. Bull. 50 (2014) 424–431, <https://doi.org/10.1016/j.materresbull.2013.11.013>.
- [4] I. Jlassi, H. Elhouichet, M. Ferid, C. Barthou, Judd-Ofelt analysis and improvement of thermal and optical properties of tellurite glasses by adding P₂O₅, J. Lumin. 130 (2010) 2394–2401, <https://doi.org/10.1016/j.jlumin.2010.07.026>.
- [5] J.E. Stanworth, Tellurite glasses, J. Soc. Glass. Technol. 38 (1954) 425.
- [6] C. Hua, L. Shen, E.Y.B. Pun, D. Li, H. Lin, Dy³⁺ doped tellurite glasses containing silver nanoparticles for lighting devices, Opt. Mater. 78 (2018) 72–81, <https://doi.org/10.1016/j.optmat.2018.02.006>.
- [7] M. Soulis, J.-R. Dulclère, T. Haykawa, V. Courdec, M. Dutreilh-Colas, P. Thomas, Second harmonic generation induced by optical poling in new TeO₂-Ti₂O-ZnO

- glasses, *Mater. Res. Bull.* 45 (2010) 551–557, <https://doi.org/10.1016/j.materresbull.2010.01.024>.
- [8] N.G. Boetti, J. Lousteau, A. Chiasera, M. Ferrari, E. Mura, G.C. Scarpignato, S. Abrate, D. Milanese, Thermal stability and spectroscopic properties of erbium-doped niobic-tungsten-tellurite glasses for laser and amplifier devices, *J. Lumin.* 132 (2012) 1265–1269, <https://doi.org/10.1016/j.jlumin.2011.12.057>.
- [9] C. Yu, Z. Yang, A. Huang, Z. Chai, J. Qiu, Z. Song, D. Zhou, Photoluminescence properties of tellurite glasses doped Dy^{3+} and Eu^{3+} for the UV and blue converted WLEDs, *J. Non-Cryst. Solids* 457 (2017) 1–8, <https://doi.org/10.1016/j.jnoncrysol.2016.11.025>.
- [10] V.P. Tuyen, V.X. Quang, P.V. Do, L.D. Thanh, N.X. Ca, V.X. Hoa, L.V. Tuat, L.A. Thi, M. Nogami, An in-depth study of the Judd-Ofelt analysis, spectroscopic properties and energy transfer of Dy^{3+} in aluminio-lithium-telluroborate glasses, *J. Lumin.* 210 (2019) 435–443, <https://doi.org/10.1016/j.jlumin.2019.03.009>.
- [11] D.V. Phan, V.X. Quang, H.V. Tuyen, T. Ngoc, V.P. Tuyen, L.D. Thanh, N.X. Ca, N. T. Hien, Structure, optical properties and energy transfer in potassium-aluminoborotellurite glasses doped with Eu^{3+} ions, *J. Lumin.* 216 (2019) 116748, <https://doi.org/10.1016/j.jlumin.2019.116748>.
- [12] V.X. Quang, P.V. Do, N.X. Ca, L.D. Thanh, V.P. Tuyen, P.M. Tan, V.X. Hoa, N. T. Hien, Role of modifier ion radius in luminescence enhancement from 5D_4 level of Tb^{3+} ion doped alkali-alumino-telluroborate glasses, *J. Lumin.* 221 (2020) 117039, <https://doi.org/10.1016/j.jlumin.2020.117039>.
- [13] A.N. Belsky, N.M. Khaidukov, J.C. Krupa, V.N. Makhov, A. Philippov, Luminescence of $CsGd_2F_7:Er^{3+}$, Dy^{3+} under UV excitation, *J. Lumin.* 94–95 (2001) 45–49.
- [14] J.G. Choi, J. Heo, 1.3 μm emission and multiphonon relaxation phenomenon in $PbO-Bi_2O_3-Ga_2O_3$ glasses doped with rare-earths, *J. Non-Cryst. Solids* 217 (1997) 199–207.
- [15] Z. Yang, W. Chen, L. Luo, Dy^{3+} -doped Ge-Ga-Sb-Se glasses for 1.3 μm optical amplifiers, *J. Non-Cryst. Solids* 351 (2005) 2513–2518, <https://doi.org/10.1016/j.jnoncrysol.2005.07.008>.
- [16] Z. Cao, S. Zhou, G. Jiang, Y. Chen, C. Duan, M. Yin, Temperature dependent luminescence of Dy^{3+} -doped $BaYF_5$ nanoparticles for optical thermometry, *Curr. Appl. Phys.* 14 (2014) 1069–1071, <https://doi.org/10.1016/j.cap.2014.05.020>.
- [17] Y. Tian, R. Xu, L. Hua, J. Zhang, Broadband 2.84 μm luminescence properties and Judd-Ofelt analysis in Dy^{3+} -doped $ZrF_4-BaF_2-LaF_3-AlF_3-YF_3$ glass, *J. Lumin.* 132 (2012) 128–131, <https://doi.org/10.1016/j.jlumin.2011.08.017>.
- [18] M. Zhang, A. Yang, Y. Peng, B. Zhang, H. Ren, W. Guo, Y. Yang, C. Zhai, Y. Wang, Z. Yang, D. Tang, Dy^{3+} -doped Ga-Sb-S chalcogenide glasses for mid-infrared lasers, *Mater. Res. Bull.* 70 (2015) 55–59, <https://doi.org/10.1016/j.materresbull.2015.04.019>.
- [19] L. Gomes, J. Lousteau, D. Milanese, E. Mura, S.D. Jackson, Spectroscopy of mid-infrared (2.9 μm) fluorescence and energy transfer in Dy^{3+} -doped tellurite glasses, *J. Opt. Soc. Am. B* 31 (2014) 429–435, <https://doi.org/10.1364/JOSAB.31.000429>.
- [20] Wojciech A. Pisarski, Joanna Pisarska, Lidia Zur, Tomasz Goryczka, Structural and optical aspects for Eu^{3+} and Dy^{3+} ions in heavy metal glasses based on $PbO-Ga_2O_3-XO_2$ (X = Te, Ge, Si), *Opt. Mater.* 35 (2013) 1051–1056, <https://doi.org/10.1016/j.optmat.2012.12.012>.
- [21] M. Reza Dousti, S. Raheleh Hosseini, Enhanced upconversion emission of Dy^{3+} -doped tellurite glass by heat-treated silver nanoparticles, *J. Lumin.* 154 (2014) 218–223, <https://doi.org/10.1016/j.jlumin.2014.04.028>.
- [22] M. Vijayakumar, K. Marimuthu, Tailoring the luminescence of Eu^{3+} co-doped Dy^{3+} incorporated aluminofluoro-borophosphate glasses for white light applications, *J. Lumin.* 178 (2016) 414–424, <https://doi.org/10.1016/j.jlumin.2016.06.016>.
- [23] G. Wang, S. Xu, S. Dai, J. Yang, L. Hu, Z. Jiang, Thermal stability, spectra and laser properties of Yb:lead-zinc-telluride oxide glasses, *J. Non-Cryst. Solids* 336 (2004) 102–106, <https://doi.org/10.1016/j.jnoncrysol.2004.01.009>.
- [24] S.K.J. Al-Ani, S.S. Al-Rawi, A.H. Jassim, H.A. Al-Hilli, FTIR spectra of Molybdenum tellurite glasses, *Iraqi J. Appl. Phys.* 2 (2006) 23–25.
- [25] H. Burger, K. Kneipp, H. Hobert, W. Vogel, V. Kozhukharov, S. Neov, Glass formation, properties and structure of glasses in the TeO_2-ZnO system, *J. Non-Cryst. Solids* 151 (1992) 134–142.
- [26] T. Sekiya, N. Mochida, A. Ohtsuka, Raman spectra of $MO-TeO_2$ (M = Mg, Sr, Ba and Zn) glasses, *J. Non-Cryst. Solids* 168 (1994) 106–114.
- [27] P. Wang, C. Wang, W. Li, M. Lu, B. Peng, Effects of Al_2O_3 on the thermal stability, glass configuration of Yb^{3+} -doped $TeO_2-K_2O-ZnO-Al_2O_3$ based tellurite laser glasses, *J. Non-Cryst. Solids* 359 (2013) 5–8, <https://doi.org/10.1016/j.jnoncrysol.2012.09.031>.
- [28] M.V. Vijaya Kumar, B.C. Jamalalah, K. Rama Gopal, R.R. Reddy, Optical absorption and fluorescence studies of Dy^{3+} -doped lead telluroborate glasses, *J. Lumin.* 132 (2012) 86–90, <https://doi.org/10.1016/j.jlumin.2011.07.021>.
- [29] K. Damak, El S. Yousef, C. Rüssel, R. Maâlej, White light generation from Dy^{3+} -doped tellurite glass, *J. Quant. Spectrosc. Radiat. Transfer* 134 (2014) 55–63, <https://doi.org/10.1016/j.jqsrt.2013.10.013>.
- [30] B. Klimesz, W. Ryba-Romanowski, R. Lisiecki, Oxyfluorotellurite glasses doped by dysprosium ions. Thermal and optical properties, *Opt. Mater.* 42 (2015) 538–543, <https://doi.org/10.1016/j.optmat.2015.02.012>.
- [31] O. Ravi, C. Madhukar Reddy, B. Sudhakar Reddy, B. Deva Prasad Raju, Judd-Ofelt analysis and spectral properties of Dy^{3+} ions doped niobium containing tellurium calcium zinc borate glasses, *Opt Commun.* 312 (2014) 263–268, <https://doi.org/10.1016/j.optcom.2013.09.044>.
- [32] K. Maheshvaran, K. Marimuthu, Structural and optical investigations on Dy^{3+} -doped boro-tellurite glasses, *J. Alloys Compd.* 509 (2011) 7427–7433, <https://doi.org/10.1016/j.jallcom.2011.04.055>.
- [33] R. Cases, M.A. Chammaro, Judd-Ofelt analysis and multiphonon relaxations of rare earth ions in fluorohafnate glasses, *J. Solid State Chem.* 90 (1991) 313–319.
- [34] A. Awang, S.K. Ghoshal, M.R. Sahar, M.R. Dousti, R.J. Amjad, F. Nawaz, Enhanced spectroscopic properties and Judd-Ofelt parameters of Er-doped tellurite glass: Effect of gold nanoparticles, *Curr. Appl. Phys.* 13 (2013) 1813–1818, <https://doi.org/10.1016/j.cap.2013.06.025>.
- [35] P. Babu, C.K. Jayasankar, Spectroscopic properties of Dy^{3+} ions in lithium borate and lithium fluoroborate glasses, *Opt. Mater.* 15 (2000) 65–79.
- [36] S. Surendra Babu, P. Babu, C.K. Jayasankar, Th. Tröster, W. Sievers, G. Wortmann, Optical properties of Dy^{3+} -doped phosphate and fluorophosphates glasses, *Opt. Mater.* 31 (2009) 624–631, <https://doi.org/10.1016/j.optmat.2008.06.019>.
- [37] B.R. Judd, Optical absorption intensities of rare-earth ions, *Phys. Rev.* 127 (1962) 750–761.
- [38] G.S. Ofelt, Intensities of crystal spectra of rare-earth ions, *J. Chem. Phys.* 37 (1962) 511–520.
- [39] M. Jian-Xin, Y. Chuang-Tao, C. Qing-Qing, Photoluminescence characterization of Ce^{3+} and Dy^{3+} doped Li_2CaGeO_4 phosphors, *J. Lumin.* 130 (2010) 1320–1323, <https://doi.org/10.1016/j.jlumin.2010.02.047>.
- [40] M. Yu, J. Lin, Z. Wang, J. Fu, S. Wang, H.J. Zhang, Y.C. Han, Fabrication, patterning and optical properties of nanocrystalline $YVO_4:A$ (A = Eu^{3+} , Dy^{3+} , Sm^{3+} , Er^{3+}) phosphor films via sol-gel soft lithography, *Chem. Mater.* 14 (2002) 2224–2231.
- [41] N. Vijaya, K. Upendra Kumar, C.K. Jayasankar, Dy^{3+} -doped zinc fluorophosphate glasses for white luminescence applications, *Spectrochim. Acta A* 113 (2013) 145–153, <https://doi.org/10.1016/j.saa.2013.04.036>.
- [42] D.V.R. Murthy, B.C. Jamalalah, A. Mohan Babu, T. Sasikala, L. Rama Moorthy, The luminescence properties of Dy^{3+} -doped alkaline earth titanium phosphate glasses, *Opt. Mater.* 32 (2010) 1112–1116, <https://doi.org/10.1016/j.optmat.2010.03.009>.
- [43] A. Mohan Babu, B.C. Jamalalah, J. Suresh Kumar, T. Sasikala, L. Rama Moorthy, Spectroscopic and photoluminescence properties of Dy^{3+} -doped lead tungsten tellurite glasses for laser materials, *J. Alloys Compd.* 509 (2011) 457–462, <https://doi.org/10.1016/j.jallcom.2010.09.058>.
- [44] Xin-yuan Sun, Shi-ming Huang, Xiao-san Gong, Qing-chun Gao, Zi-piao Ye, Chun-yan Cao, Spectroscopic properties and simulation of white light in Dy^{3+} -doped silicate glass, *J. Non-Cryst. Solids* 356 (2010) 98–101, <https://doi.org/10.1016/j.jnoncrysol.2009.10.009>.
- [45] C.S. McCamy, Correlated color temperature as an explicit function of chromaticity coordinates, *Color Res. Appl.* 17 (1992) 142–144.
- [46] E.C. Fuchs, C. Sommer, F.P. Wenzl, B. Bitschnau, A.H. Paulitsch, A. Muhlanger, K. Gatterer, Polyspectral white light emission from Eu^{3+} , Tb^{3+} , Dy^{3+} , Tm^{3+} co-doped $GdAl_3(BO_3)_4$ phosphors obtained by combustion synthesis, *Mater. Sci. Eng. B* 156 (2009) 73–78, <https://doi.org/10.1016/j.mseb.2008.11.024>.